A Thesis for the Degree of Ph.D. in Engineering

Numerical investigation on the discharge process of a nanosecond-pulsed surface dielectric-barrier-discharge plasma actuator

February 2019

Graduate School of Science and Technology
Keio University

Weizhuo Hua

Acknowledgements

First and foremost, I would like to express my heartfelt gratitude to my supervisor, **Professor Koji Fukagata**, for his constant encouragement and guidance on my research. He not only gives me consistent and illuminating instruction in research, but also acts as an example who is responsible and devoted to research.

I am deeply indebted to **Professor Shinnosuke Obi** and **Professor Keita Ando** for the insightful comments during the lab seminar, which help me improving and extending my research.

I would like to thank all of the labmates of Obi-Fukagata-Ando laboratories. They are so kind and always willing to help me in both research and life. I really appreciate the fruitful discussion with **Dr. Mehdi Badri** and **Dr. Hosnier Kor**.

I gratefully acknowledge the financial support from the scholarship provided by Xi'an Jiaotong University. My sincere acknowledgements also go to the Research Grant from the Keio Leading-edge Laboratory of Science and Technology. Moreover, this work was partly supported through Council for Science, Technology and Innovation (CSTI), Cross-ministerial Strategic Innovation Promotion Program (SIP), "Innovative Combustion Technology" (Funding agency: JST).

I also want to sincerely thank my examining committee, **Professor Shinnosuke Obi** (Keio University), **Professor Keita Ando** (Keio University) and **Professor Hiroyuki Nishida** (Tokyo University of Agriculture and Technology) for their time commitment and valuable comments.

Last but not least, my sincere thanks would go to my beloved family. Their whole-hearted support to me always motivate me to keep forward.

Abstract

Surface dielectric-barrier-discharge plasma actuator (SDBD-PA) has shown its promising prospects in aerodynamic applications. Due to the complexity in discharge plasmas, numerical modelling of plasma actuators is important to understand the its physics and improve the intensity of plasma actuation.

Two-dimensional fluid-model simulation of an SDBD-PA, driven by a nanosecond voltage pulse, is conducted. We first focus on the influence of grid resolution on the computational result. It is found that the result is not sensitive to the streamwise grid spacing, whereas the wall-normal grid spacing has a critical influence. The computed propagation velocity of discharge streamer changes discontinuously around the wall-normal grid spacing about 2 μm due to a qualitative change of discharge structure. The present result suggests that a computational grid finer than that was used in most of previous studies is required to correctly capture the structure and dynamics of streamer: under positive nanosecond voltage pulse, a streamer forms in the vicinity of upper electrode and propagates along the dielectric surface with a maximum velocity of 2×10^8 cm/s, and plasma sheath layer with low electron density exists between the streamer and dielectric surface.

Based on the grid convergence study, a systematic numerical investigation of the nanosecond-pulsed SDBD evolution under positive (PEP) and negative electrode polarity (NEP) is performed. Under both PEP and NEP, two discharge strokes take place corresponding to the leading edge and trailing edge of the nanosecond voltage pulse. During the first stroke, the positive streamer propagates along the dielectric surface accompanying a thin sheath layer, while the negative streamer stays attached to the dielectric surface. The positive streamer propagates faster than the negative streamer. During the second stroke, a sheath layer forms between the negative streamer and the dielectric surface due to the electrons drifting away from the near-surface region, while the sheath layer between the positive streamer and the dielectric surface fades away due to the electrons drifting toward the dielectric surface. For both PEP and NEP, it is revealed that a strong downstream body force is generated when the sheath layer exists, due to the high net charge density and strong electric field in the near-surface sheath layer.

Parametric study is conducted to investigate the influence of voltage amplitude, dielectric permittivity and thickness on the discharge propagation, generated body force and heat source under both PEP and NEP. It is found that the discharge current, generated body force and heat source increase with increasing the dielectric permittivity or decreasing the dielectric thickness. The improvement of body force is mainly due to the increase of net charge density in the sheath layer.

The series of numerical simulations reveal the plasma discharge in detail, which is important to understand the physics of SDBD-PA and to help improving its flow control ability.

Contents

List of Figures

List of Tables

Nomenclature

c	elementary charge
$\vec{D}$	electric displacement
D_p	diffusion coefficient of positive ions
D_n	diffusion coefficient of negative ions
D_e	diffusion coefficient of electrons
$\vec{E}$	electric field vector
$E,\ \|\vec{E}\|$	electric field strength
E_0	electric field strength at the coordinate origin in Fig. 1.4
E_{0+}	wall-normal (y) component of electric field at the interface (air side) in Fig. 2.6
E_{0-}	wall-normal (y) component of electric field at the interface (dielectric side) in Fig. 2.6
$\vec{f_e}$	EHD body force field
F_x	Streamwise component of domain-integrated EHD body force
j_p	wall-normal (y) component of current density of positive ions
j_e	wall-normal (y) component of current density of positive ions
$\vec{n}$	normal vector on a control surface
n_p	number density of positive ions, cm^{-3}
n_n	number density of negative ions, cm^{-3}
n_e	number density of electrons, cm^{-3}
P	pressure of air
q_s	surface free charge areal density
Q_s	surface free charge
r	rate coefficient of recombination
t	time
W	domain-integrated heat source
x	streamwise coordinate
y	wall-normal coordinate
α	rate coefficient of impact ionization
β	rate coefficient of attachment
Δx	grid spacing in streamwise (x) direction
Δy_j	grid spacing in wall-normal (y) direction of layer j in Fig. 2.5

$\Delta y_{j+1/2}$	spacing in wall-normal (y) direction between layer j and $j+1$ in Fig. 2.5
ε	relative permittivity
ε_0	vacuum permittivity
γ	coefficient of secondary electron emission
Γ_p	drift-diffusion flux of positive ions
Γ_n	drift-diffusion flux of negative ions
Γ_e	drift-diffusion flux of electrons
λ_D	Debye length
$\boldsymbol{\phi}$	total electric potential
ϕ	electric potential due to the external electric field
ρ_c	net charge density
σ_s	surface charge number density
φ	electric potential due to the plasma
τ_d	dielectric relaxation time
μ_p	mobility coefficient of positive ions
μ_n	mobility coefficient of negative ions
μ_e	mobility coefficient of electrons

Chapter 1

Introduction

1.1 Background

Surface dielectric barrier discharge plasma actuator (SDBD-PA) has attracted considerable attentions in recent 15 years because of its availability in a wide range of pressure [1] and promising advantages, such as absence of moving parts, low mass, fast response for unsteady applications and the ability to apply the actuator onto the surface without the addition of cavities of holes [2]. Researches on applications of SDBD-PA have been conducted in different fields, including flow control [2–8], combustion initiation [9–11], and so on. Researches on plasma flow control are summarized by Moreau [3], Corke et al. [2, 12, 13], Wang et al. [14], while a comprehensive overview of plasma-assisted ignition and combustion is given in review papers by Starikovskaia et al. [10, 15].

Dielectric barrier discharge (DBD) have drawn great attention all over the world since it was first reported experimentally by Siemens in 1857 [16]. At first, DBDs are mainly used for the generation of Ozone. DBDs are featured in the generation of 'cold' non-equilibrium plasmas at atmospheric pressure and the strong influence of the local electric field distortions caused by space charge accumulation [17]. A

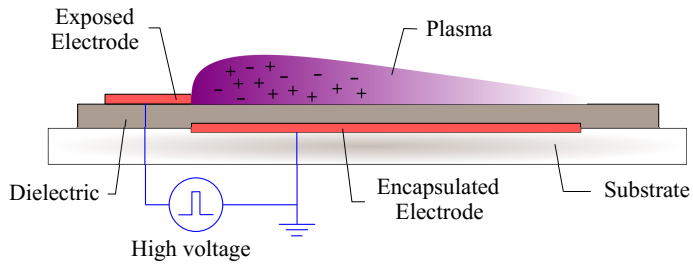

Figure 1.1: Schematic configuration of a surface dielectric-barrier-discharge plasma actuator.

number of researches extend the application of DBD from Ozone generation to plasma display panels [18], flow control [2–4, 6, 7, 12, 13, 19–28], plasm-assisted ignition and combustion [10, 11, 15, 29, 30], and so on.

The typical configuration of an SDBD plasma actuator is show in Fig. 1.1. Two asymmetric electrodes are separated by the dielectric layer. When different voltage waveforms are applied to the exposed electrode and encapsulated electrode, the difference of electrical potential between the electrodes will generate electric field. If the electric field strength is strong enough to exceed the ionization threshold, the air will be ionized and plasma will be generated from the discharge. A wide range of physicochemical phenomena occur in the plasma region, including processes of excitation of electronic states, destruction and ionization of heavy particles by electron impact, associative ionization, electron attachment and detachment, electron-ion and ion-ion recombination, chemical transformations of neutral particles (in ground and excited electronic states) and ion conversion, which are described in detail by Kossyi et al. [31]. In addition to these complicated physicochemical reactions, the electric field is distorted by the accumulation of the space and surface charges. The presence of electric field and charged particles will result in a electrohydrodynamic (EHD) body force field acting on the ambient air. The body force is one of the mechanism for active flow control.

Based on the applied voltage waveform, the SDBDs are divided into ACDBD

and NSDBD [23]. ACDBD is driven by an alternative current (AC) high voltage waveform and is most studied in the early period of the research on SDBD. The generation of EHD body force is the mechanism for ACDBD driven flow control [2, 13]. A large number of researches are conducted to improve the EHD body force and induced flow velocity by plasma actuation [20, 32, 33]. Roth et al. [32] analyzed the physical process and power flows that occur in plasma actuators, and divided the power flows through a plasma actuator into four sinks: reactive power losses due to inadequate impedance matching of the power supply to the actuator; dielectric heating of the actuator insulating materials; power required to maintain the atmospheric pressure plasma; power coupled to neutral gas flow by ion-neutral collisions, as shown in Fig. 1.2. Among them, the fourth fraction (i.e., power coupled to neutral gas flow by ion-neutral collisions) is responsible for the body force and induced flow. Experimental researches are conducted to maximize the induced flow velocity by adjustment of the actuator geometry, dielectric materials, RF frequency and RMS voltage. A parametric experimental investigation is conducted by Thomas et al. [20] to optimize the body force produced by SDBD plasma actuator. They examines the effects of dielectric dielectric material and thickness, applied voltage amplitude and frequency, exposed electrode geometry, covered electrode width, and multiple actuator arrays, and it is demonstrated that plasma actuators constructed with thick dielectric material of low dielectric constant produce a body force that is an order of magnitude larger than that obtained by the Kapton-based actuators used in many previous plasma flow control studies.

Even though a large number of works have been conducted to improve the intensity of actuation by ACDBD, the induced flow velocity by ACDBD plasma actuation hardly exceeds 10 m/s [23]. The intensity of plasma actuation of ACDBD limits its application for flow control, especially for flow control applications at

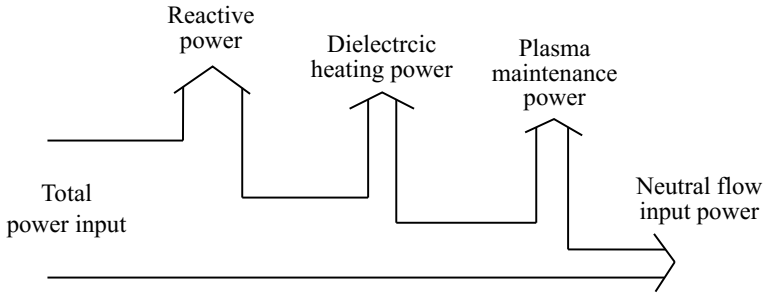

Figure 1.2: Schematic of the power flow through a plasma actuator.
Figure adapted from [32].

higher Reynolds number. NSDBD is a different kind of DBD plasma actuator which is driven by nanosecond pulsed voltage, and it is proved to be effective in control boundary layer separation, lift and drag coefficients, and acoustic noise in the Mach number range of 0.05 to 0.85 [4]. The duration τ of the nanosecond pulsed voltage is typically several nanoseconds to several hundreds nanoseconds, while the rise time τ_{rise} and fall time τ_{fall} is several nanoseconds. When nanosecond pulsed voltage is applied to the electrode, the fast discharge induces an impulsive power deposition in the discharge volume/plasma layer on the time scale of 10^{-9} s. The impulsive power deposition results in a rapid (typically within 1 μs) increase of the temperature in the plasma layer via Joule heating [4, 34, 35]. The measurements have shown that the mean values of such heating for the plasma layer can reach 70, 200, and even 400 K for 7-, 12- and 50-ns pulsed duration, respectively [4]. Accompanied with the thermal effect, a relatively small body force $\vec{f_e}$ is induced. However, because of the short time scale, $\vec{f_e}$ shows no visible effect on the flow. On the time scale of 10^{-6} s, shock or pressure wave emerges and propagates with around sonic speed [4, 34, 36]. The rapid temperature increase also affects the fluid properties such as viscosity and density [37]. Consequently, on the time scale of 10^{-3} s, secondary vortex flows emerges and disturbs the main flow. Figure 1.3 depicts the schlieren image of NSDBD plasma actuator on different time scales,

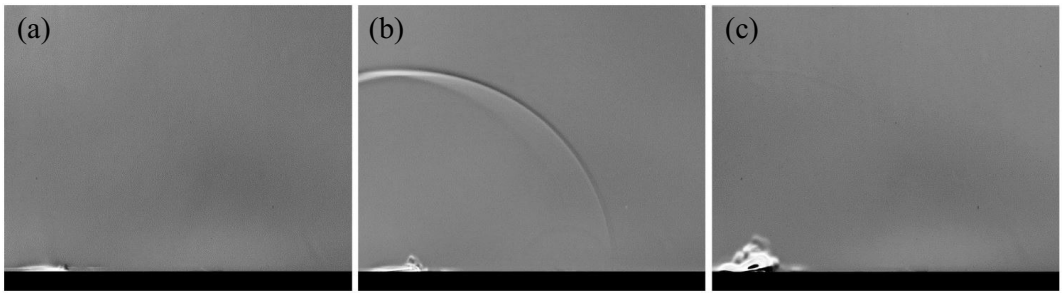

Figure 1.3: Schlieren image of nanosecond-pulsed surface dielectric-barrier-discharge plasma actuator on a (a) nanosecond, (b) microsecond and (c) millisecond time scale. Figure adapted from [37].

from which we can see the shock wave and vortex flows generated by NSDBD clearly.

The phenomena of multiple time scale make it quite difficult to explain the physical mechanism of flow control by NSDBD and generate a long debate on it. In spite of this, what is widely accepted is that, for ACDBD and NSDBD, the generated EHD body force or the fast heating from high-voltage discharge are the reason for flow control or plasma-assisted ignition and combustion. In order to understand the discharge process and obtain the spatio-temporal distribution of generated body force and heat, experimental and numerical studies on SDBD-PAs have extensively been conducted [1, 20, 23, 38–49]. However, because of the complexity of the discharge process and the restriction of the experimental apparatus, it is still beyond the ability to measure the discharge development in detail. Even the EHD body force field cannot be obtained directly from the experimental measurement, but derived from the flow field by Particle Image Velocimetry (PIV) measurement, as illustrated in [50–52].

1.2 Modelling of plasma actuator

Numerical studies can help understanding the discharge evolution in greater detail. In this section, we describe the numerical models of SDBD-PAs briefly. These models have their own advantages and disadvantages, which will be discussed in this section, too.

1.2.1 Phenomenological models

Shyy et al. [53, 54] develop a semi-empirical model to account for the EHD body force acted on the airflow by the plasma. The electric field lines are concentrated at the cathode and are almost uniformly distributed on the anode. Shyy et al. [53] assume that the electric field lines are parallelly (see Fig. 1.4(b)) and linearly distributed near the cathode, as illustrated by Eq. (1.1). Based on this assumption, we can get the electric field distribution in space without computing the detailed electric field, i.e.,

$$|E| = E_0 - k_1 x - k_2 y, \tag{1.1}$$

where E_0 is the electric field on the dielectric surface between the two separated electrodes (i.e., the origin of the coordinate in Fig. 1.4), which can be approximated as $E_0 = V/d$. Here, d is the streamwise distance between the two electrodes, and V is the difference of electric potential between electrodes.

In Shyy's model, the force acts only in the triangle area with the height of a and length of b, as shown in Fig. 1.4(b). Along the line A-B, the electric field strength is equal to the ionization threshold E_b. Hence, we can compute the constants k_1 and k_2 as

$$k_1 = \frac{E_0 - E_b}{b}, \quad k_2 = \frac{E_0 - E_b}{a}. \tag{1.2}$$

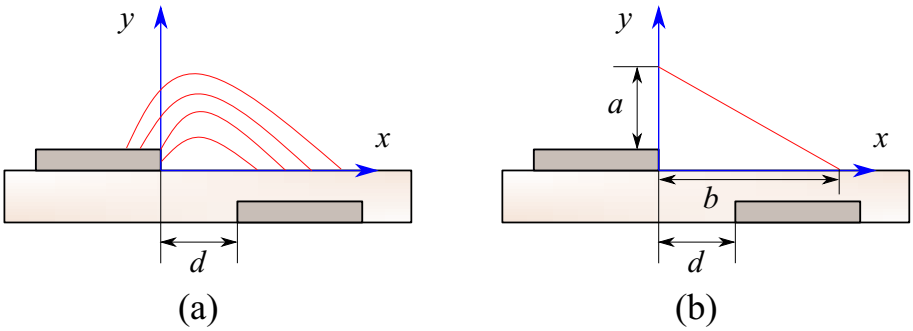

Figure 1.4: Schematic illustration of Shyy's model: (a) rough shape of electric fiedl lines, (b) linearized electric field. Figure adapted from [53].

The components of electric field are calculated as

$$E_x = \frac{Ek_2}{\sqrt{k_1^2 + k_2^2}}, \quad E_y = \frac{Ek_1}{\sqrt{k_1^2 + k_2^2}}. \tag{1.3}$$

When the frequency of the discharge is high enough, it is reasonable to consider the force acting on the fluid as a constant. The force in the triangle area can be time-averaged over a cycle of the applied voltage, i.e.,

$$f_{x,\text{ave}} = \frac{E_x \rho_c \Delta t}{T_a}, \quad f_{y,\text{ave}} = \frac{E_y \rho_c \Delta t}{T_a}, \tag{1.4}$$

where ρ_c is the net charge density, and Δt is the time duration when the plasma discharge take place, and T_a is the period of the applied voltage cycle.

Shyy's model significantly simplify the plasma actuation by using the linearized approximation of the electric field. The peak volue of the induced flow velocity obtained by using this model is in agreement with experimental results [53]. Because of its simplicity, Shyy's model is economic for numerical research on plasma flow control and used in control of transitional and turbulent flows around airfoil [55], control of vortical flows around delta wings [56], control of flow around a circular cylinder [57] and square cylinder [27]. The largest drawback of this model is that

the linearized approximation of the electric field, as well as the assumed net charge density, is too artificial, which may result in large deviation from the real EHD body force field.

Suzen et al. [19, 58] developed a two-potential model for the computation of the EHD body force. They assume the total electric potential $\boldsymbol{\phi}$ is composed of the potential ϕ due to the applied voltage on the electrodes and the potential φ due to the plasma, i.e.,

$$\boldsymbol{\phi} = \phi + \varphi. \tag{1.5}$$

The potential due to the external applied voltage is given by Eq. (1.6), while the potential due to the plasma by Eq. (1.7).

$$\nabla \cdot (\varepsilon_r \nabla \phi) = 0, \tag{1.6}$$

$$\nabla \cdot (\varepsilon_r \nabla \varphi) = -\frac{\rho_c}{\varepsilon_0}, \tag{1.7}$$

where ε_r is the relative dielectric permittivity, and ε_0 is the dielectric permittivity of the vacuum.

Boltzmann distribution for the ion and electron velocity distribution is assumed in the model. Then the net charge density in the plasma is given as

$$\frac{\rho_c}{\varepsilon_0} = -\frac{\varphi}{\lambda_D^2}, \tag{1.8}$$

where λ_D is the Debye length.

From Eqs. (1.7) and (1.8), the net charge density distribution can be obtained as

$$\nabla \cdot (\varepsilon_r \nabla \rho_c) = -\frac{\rho_c}{\lambda_D^2}. \tag{1.9}$$

Hence, the electric potential ϕ due to the external applied voltage and the net

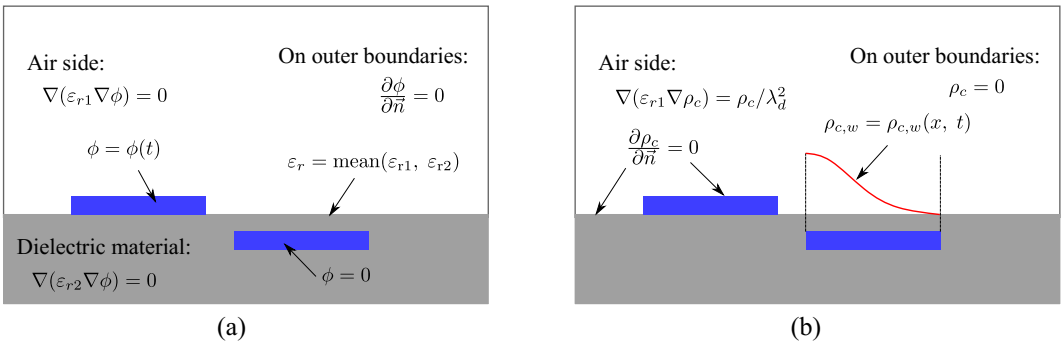

Figure 1.5: Computational domain and boundary condition for (a) Equation (1.6) and (b) Equation (1.9). Figure adapted from [19].

charge density ρ_c can be obtained from Eq. (1.6) and Eq. (1.9), respectively. Then the resultant EHD body force is computed by

$$\vec{f_e} = \rho_c\vec{E} = \rho_c(-\nabla\phi). \tag{1.10}$$

The computational domain and boundary condition for Eq. (1.6) and Eq. (1.9) are shown in Fig. 1.5. On the wall above the encapsulated electrode, a half Gaussian distribution with a maximum value of $\rho_c^{\max}$ is assumed by Suzen et al. [19, 58]. Two parameters, namely, $\rho_c^{\max}$ and λ_D need to be calibrated with available experimental date to solve Eq. (1.9).

Suzen's model is a promising approach in the computation of plasma flow control application and has been used in numerical investigation on flow seperation control [8, 59–61].

Another commonly used semi-empirical two-dimensional models of SDBD plasma actuator is developed at the University of Nortre Dame [2, 62, 63], generally called Lumped-Element Circuit model. This model simulates the surface plasma layer as distributed electrical conductivity and capacitance, as shown in Fig. 1.6. The circuit is consist of a number of network of electric circuit elements, as shown in Fig. 1.6(a). Each of these circuit elements represents a small physical domain with

finite width and consists of an air capacitor C_a, dielectric capacitor C_d and plasma resistive element R, as shown in Fig. 1.6(b). The diodes are introduced in the circuit to govern the presence of plasma in the circuit element if the electric field exceeds the ionization threshold. When the applied voltage V_{app} on the electrode is known, the voltage on the dielectric surface is obtained by using Kirchhofff's current law on the dielectric surface, i.e.,

$$\frac{dV_n(t)}{dt} = \frac{dV_{\text{app}}(t)}{dt}\left(\frac{C_{an}(t)}{C_{an}(t)+C_{dn}(t)}\right) + k_n \frac{I_n(t)}{C_{an}(t)+C_{dn}(t)}, \tag{1.11}$$

where $k_n = 0$ when the plasma is not present and $k_n = 1$ when the plasma exists in the n_{th} circuit element. The plasma current in the circuit element I_n is given as

$$I_n = \frac{1}{R_n}(V_{\text{app}}(t) - V_n(t)). \tag{1.12}$$

By solving the electric circuit Eqs. (1.11) and (1.12), we can obtain the voltage potential on the dielectric surface and the plasma current in each circuit element, respectively. The electric current in the plasma relates directly to the light emission from the SDBD [64]. The rectified plasma current from the circuit model is in good agreement with the experimental results of spatio-temporal variation of the plasma illumination [63, 64]. Orlov et al. [63, 64] also obtain the maximum extent of the plasma and the plasma sweep velocity form the computed spatio-temporal rectified current.

By using the voltage potential on the dielectric surface as the boundary condition for the electric potential $\boldsymbol{\phi}$ in the electrostatic equation, i.e.,

$$\nabla(\varepsilon\nabla\boldsymbol{\phi}) = \frac{1}{\lambda_D^2}\boldsymbol{\phi}, \tag{1.13}$$

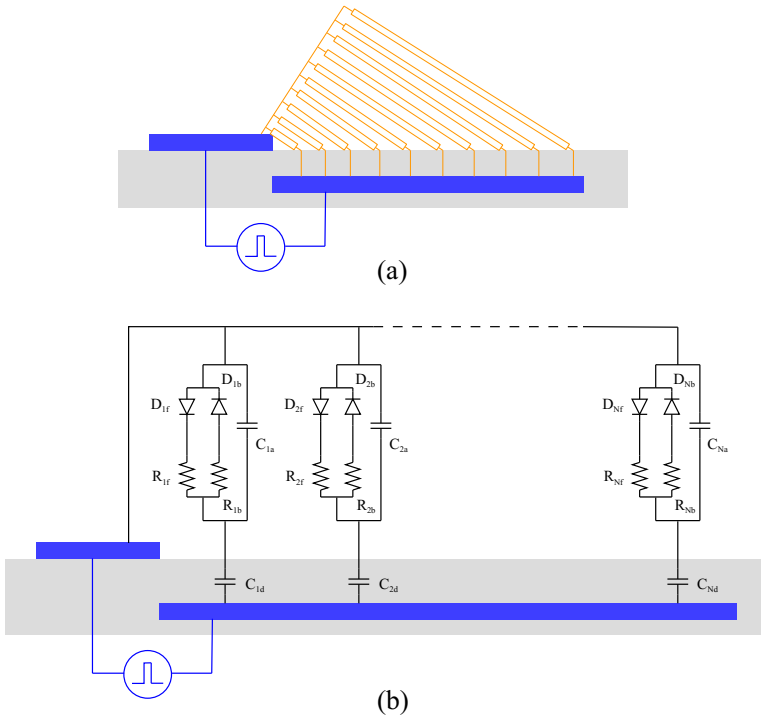

Figure 1.6: Schematic of Lumped-Element Circuit model: (a) circuit elements, (b) network of a single circuit element. Figure adapted from [63]

the electric potential can be computed. Then the EHD body force generated by the plasma is calculated as

$$\vec{f_e} = \rho_c \vec{E} = \left(\frac{\varepsilon_0 \phi}{\lambda_D^2} \right) \nabla \phi. \tag{1.14}$$

This model has been fairly successful predicting the time-dependent EHD body force and applying to the leading-edge separation control on the NACA 0021 airfoil [64].

Phenomenological models has been fairly successful to predict the time-averaged EHD body force. However, phenomenological models are not capable of describing the transport of charged particles and predicting the propagating of the discharge streamer. Physics-based models are needed to better understand the discharge propagation and the generation of EHD body force and heat source.

1.2.2 Kinetic model

Kinetic models describes the plasma by solving the distribution function $f_j(\vec{x}, \vec{v}, t)$ of each type of particles j in phase-space. Here, the independent variables $\vec{x}$ and $\vec{v}$ are position and velocity. Thus, for each type of particles j, at each position $\vec{x}$, the number of such particles in an element of volume $d^3\vec{x}$ are $f_j(\vec{x}, \vec{v})d^3\vec{x}d^3\vec{v}$. Note that in some papers [10, 31, 44, 65], the word 'kinetics' is used to describe the chemical transformations of particles in the discharge. Some fluid model (which will be discussed in Section 1.2.3) considering a part of chemical transformations of particles are also called kinetic models. In this dissertation, kinetics model refers to the model solving the distribution function, rather than the fluid model considering a part of the chemical transformations.

The Boltzmann equation (BE) is used to solve the distribution function $f(\vec{x}, \vec{v}, t)$ for each type of particles in phase space. In an ionized gas, the BE is,

$$\frac{\partial f}{\partial t} + \vec{v} \cdot \frac{\partial f}{\partial \vec{x}} + \frac{q\vec{E}}{m} \cdot \frac{\partial f}{\partial \vec{v}} = (\frac{df}{dt})_{\text{coll}}, \tag{1.15}$$

where q is charge of the particles, and m is the mass of the particles. Hence, the electromagnetic force acting on the particle is represented as $\vec{f_e} = q\vec{E}$. The term on the right hand side of Eq. (1.15) is the collision terms and describes the collisions between the particles. It is worth noting that Eq. (1.15) must be solved for each type of particle species. To obtain a self-consistent solution of Eq. (1.15), the electric field $\vec{E}$ needed to be computed from the solution of Poisson equation,

$$\nabla \cdot \vec{E} = \frac{\rho_c}{\varepsilon\varepsilon_0}, \tag{1.16}$$

The collision term in Eq. (1.15) is the source of the non-linearity and is often modelled by using the Monte-Carlo (MC) method. The Monte-Carlo method uses

many particles for random sampling of collision events in order to reproduce the behaviour of real particles in the plasma [66, 67].

The exact solution of BE is extremely difficult and time consuming because it is multi-dimensional and highly time-dependent. Even for the zero-dimensional steady-state case, it can be a challenge to solve the BE to obtain the distribution function [10]. The present available solution of BE is based on simplifications or assumptions. There exist plenty kinds of ionized, excited and neutral state of particles in the plasma, but only the dominant particles, electrons, are considered to solve the BE. On the other hand, two-term approximation is usually used to solve the BE [68].

1.2.3 Fluid model

Nowadays, in spite of the rapid development of computer science, it is still extremely time-consuming to solve the Boltzmann equation in kinetic model. To reduce the complexities in the kinetic model, the fluid model describes the plasma based on macroscopic properties of plasma, i.e., the first a few moments of the BEs for the electrons, ions and possibly other reactive particle species with near-Maxwellian distribution function. Each of the moments of the BEs is a transport equation describing the dynamics of a quantity associated with a given power of velocity, including: (1) the continuity equation, (2) the momentum equation, usually approximated by the drift-diffusion equation and (3) the energy equation, usually only for electrons [68].

Fluid model treats the particles in the plasma as continuum. The fluid (transport) equation for macroscopic quantities, such as particle density, momentums and energy are obtained to describe the plasma dynamics. In fluid model, the basic phenomena necessary for gas discharges are considered, such as ionization,

attachment, drift-diffusion of the charged particles, evolution of the electric field, recombination, etc. However, the fluid equations are not closed without the determination of the transport coefficients (i.e., drift coefficients, diffusion coefficients of particles) or rate coefficients (i.e., ionization coefficient, attachment coefficient, recombination coefficient, etc.). The transport coefficients and rate coefficients are related to the distribution function $f(\vec{x}, \vec{v}, t)$, and the accuracy of the fluid model is highly depend on the coefficients. The coefficients used for fluid models are obtained by solving the BE in the zero-dimensional steady-state case for a series of reduced electric field, and putting the resulting coefficients in tables versus the reduced electric field. Then the tables are used in the fluid model to find the transport coefficients and rate coefficients by interpolation [68]. There are several BE solvers that can be used for fluid-model of discharge, such as BOLSIG+ [68, 69], BOLOS [70], ELENDIF [71], etc.

Along with the transport equations, the Poisson equation (1.16) for electric field need to be solved. By solving the transport equation of charged particle coupled with Poisson equation, we can get the transport of the charged particles and the evolution of the electric field. A more elaborate description of the fluid model is given in Chapter 2. Compared with phenomenological models, fluid models considers the primary phenomenon in plasma discharge; compared with kinetic models, the fluid approximation is more economic. Such advantages make fluid model a good tool to simulation the discharge propagation. Since firstly carried out by Davies et al. in the 1970s [72], fluid models have draw great attention in the research on plasma display panel, discharge propagation of SDBD, etc.

The first simulation on gas discharge using fluid model dates back to the 1970s. Davies et al. [72] succeed to trace theoretically the growth in space and time of a rapidly developing gaseous discharge in nitrogen between parallel-plate electrodes

by using fluid model. From then, plenty of groups started to conduct fluid simulation of plasma discharge, both volume discharge and surface discharge. In this dissertation, we focus on the simulation of surface dielectric barrier discharge, so researches on the volume discharge simulation are not reviewed. As for the researches on surface dielectric barrier discharge plasma actuator, the results presented in the publications are mainly from the following groups: The Center of Plasma Physics and Applications in Toulouse [39, 73–75], Moscow Institute of Physics and Technology [76–79], Princeton University [41, 80]. In the previous studies on SDBD-PA using the fluid model, the simulations of the discharge structure and the generated body force have shown success. The results obtained form the fluid model correctly depicted the discharge discharge morphology depending on the polarity of the voltage applied to the electrode [49, 77].

1.2.4 Other models

Another kinetic way to describe the plasma is to track the motion of particles directly, known as particle model. Broadly speaking, particle model can also be viewed as kinetic model as described in Section 1.2.2. Here, we describe the particle model independently for clarity. In particle model, the interaction between charged particles and the electric field is solved by using the Particle-in-Cell (PIC) method. The basic equations for the PIC method are the momentum equation of individual particles and Poisson equation (1.16).

$$m\frac{d^2\vec{x}}{dt^2} = q\vec{E}, \tag{1.17}$$

where m and q are the particle mass and charge, respectively. Note that due to the enormous number of particles in realistic plasma, researchers usually introduce

'macro-particles' consisting of several real particles to reduce the computational cost [67, 81]. On the other hand, another necessary part of particle model is to describe the collisions between plasma and neutral particles, which is usually solved by the MC method. The main drawback of particle method is the same as kinetic model, i.e., the extremely high computational cost.

Hybrid model takes the advantage of both kinetic model and fluid model. It avoid computational heavy kinetic simulations and still not lose to much accuracy. These hybrid models treat some parts of the discharge region as a fluid and others kinetically. Babaeva et al. [47] computed the NSDBD by using a 2D fluid-Monte Carlo simulation. They treated the energetic secondary electrons near the dielectric surface in a fully kinetic way, while other regions as fluid. Sugimoto et al. [67] constructed a hybrid model depend on the electron density. Regions with high electric fields and low electron density are computed by the particle model while regions with low electric fields and a high electron density are treated by the fluid model.

1.3 Motivations and objectives

The applications of SDBD-PA require understanding of the physical mechanisms inside plasma discharge. This thesis aims at investigating the discharge process of nanosecond-pulsed SDBD-PA and understand the discharge physics in detail. Based on the detailed understanding of the discharge process, we can gain some insight on the improvement of flow control capability of SDBD-PA.

In the previous studies on SDBD-PA using the fluid model [39, 41, 43, 74, 82, 83], both the discharge structure and the generated body force are investigated, but the computational grid spacing used in these studies are significantly different from one another: it ranges from 1–100 μm. It is hardly known whether the

results are grid-convergent and it is hard to say whether the obtained results are reasonable enough to analyze the discharge process and the mechanism of body force generation. In the present study, we first examine different grid configurations and compare the obtained results to see whether and how the discharge structure is qualitatively influenced by the grid spacing. Subsequently, the transport of charged particles (in particular, electrons) computed using different grid resolutions is analyzed to explain the effect of grid resolution on the accuracy of discharge evolution simulation.

The discharge patterns on the dielectric surface depend on the polarity of the applied voltage. When a positive voltage is applied to the upper electrode, distinct discharge streamers propagate from the vicinity of upper electrode along the dielectric surface, while a homogeneous and diffused discharge is observed with the opposite polarity [1]. However, most of the previous numerical studies on SDBD consider a constant, linear or sinusoidal voltage waveform [79]. Recently, Soloviev et al. [79] studied SDBD initiated by a high nanosecond voltage pulse of negative electrode polarity. It was shown that two discharge strokes were observed corresponding to the leading and trailing edges of the voltage pulse. Babaeva et al. [47] investigated nanosecond pulsed SDBD of positive and negative electrode polarities using both a conventional fluid model and a hybrid model. The hybrid model treats the energetic secondary electrons in a fully kinetic way by using electron Monte Carlo simulation. Special attentions were paid on the influence of energetic secondary electrons. In the previous numerical studies on SDBD driven by nanosecond voltage pulse [41, 47, 49, 78, 84, 85], however, a systematic comparison of the entire discharge process under different polarities has not been conducted, although comprehensive understanding based on such a systematic study is an important step toward improvement of SDBD plasma actuators. In the present study,

We first systematically compare the discharge evolution under positive electrode polarity (PEP) and negative electrode polarity (NEP). Subsequently, the transport of charged particles in the near-surface region is analyzed to explain the distinct discharge development under different electrode polarities. Besides, the generated EHD body force and heat source are compared between different electrode polarities.

In order to improve the generated EHD body force and heat source by SDBD-PA and understand the physical mechanisms behind, parametric study is conducted to numerically investigate the effect of voltage amplitude, dielectric permittivity and dielectric thickness on the discharge propagation, induced EHD body force and heat source under both PEP and NEP.

1.4 Organization of this thesis

Two-dimensional fluid modelling of an SDBD-PA, driven by a nanosecond voltage pulse, is conducted in the thesis.

In Chapter 2, the numerical procedure is described in detail, including the governing equation of fluid model of plasma discharge, the computational domain and boundary conditions, and the spatial discretization and time integration.

In Chapter 3, we conduct grid convergence study on the numerical simulation of SDBD-PA. The influence of streamwise and wall-normal resolution effect on the computational results is investigated. In order to explain the reason for the influence of grid resolution, the transport of charged particles are analyzed.

In Chapter 4, based on the grid convergence study, a systematic investigation on the discharge process of nanosecond-pulsed SDBD-PA under positive electrode polarity (PEP) and negative electrode polarity (NEP) is conducted. Then, the

transport of charged particles and its influence on the discharge propagation are analyzed for both PEP and NEP.

In Chapter 5, parametric study on the discharge plasma under both PEP and NEP are conducted. The discharge propagation, generated body force and discharge power are investigated and compared between different parameters of the plasma actuator, including the amplitude of the applied voltage, dielectric permittivity, the dielectric thickness.

In Chapter 6, the thesis is summarized and conclusion are drawn. Besides, the discussions on the future research on the fluid-model simulation of an SDBD-PA are given.

Chapter 2

Numerical approach

Plasma discharge in ambient gas is investigated. Three kind of particles are considered in the model, including electron, positive ions and negative ions. Electron impact ionizations ($N_2 + e \rightarrow N_2^+ + e + e,\ O_2 + e \rightarrow O_2^+ + e + e$), electron attachment (three body and dissociative attachment of O_2), and recombination are taken into account as plasma chemistry [86]. For a more detailed description of particls and chemical transformations, readers are referred to [31, 65]. In this dissertation, we adopted very fine grid to resolve the discharge structure correctly, so only 3 kind of charged particles are taken into consideration to reduce the computational cost. Besides, we are not interested in the detailed chemistry reactions in the discharge and taking into account only one type of positive and negative ions is sufficient for our purpose [84].

2.1 Governing equations

The plasma discharge process is modelled as the time-dependent fluid equations for ions and electrons, coupled with the Poisson equation for the electric potential. The transport equations consider the drift-diffusion flux, source and sink for positive

ions, negative ions and electrons:

$$\frac{\partial n_{\mathrm{p}}}{\partial t} + \nabla \cdot \vec{\Gamma}_{\mathrm{p}} = \alpha n_{\mathrm{e}} \mu_{\mathrm{e}} \|\vec{E}\| - r n_{\mathrm{p}} n_{\mathrm{e}} - r n_{\mathrm{p}} n_{\mathrm{n}}, \tag{2.1a}$$

$$\frac{\partial n_{\mathrm{n}}}{\partial t} + \nabla \cdot \vec{\Gamma}_{\mathrm{n}} = \beta n_{\mathrm{e}} \mu_{\mathrm{e}} \|\vec{E}\| - r n_{\mathrm{n}} n_{\mathrm{p}}, \tag{2.1b}$$

$$\frac{\partial n_{\mathrm{e}}}{\partial t} + \nabla \cdot \vec{\Gamma}_{\mathrm{e}} = (\alpha - \beta) n_{\mathrm{e}} \mu_{\mathrm{e}} \|\vec{E}\| - r n_{\mathrm{e}} n_{\mathrm{p}}, \tag{2.1c}$$

where n_{i} and $\vec{\Gamma}_{\mathrm{i}}$ (i = p, n, e) denote the number density and flux of charged particles, the subscripts p, n, and e represent positive ions, negative ions and electrons, respectively. In the drift-diffusion approximation [80, 84], the charged particle fluxes are:

$$\begin{aligned} \vec{\Gamma}_{\mathrm{p}} &= n_{\mathrm{p}} \mu_{\mathrm{p}} \vec{E} - D_{\mathrm{p}} \nabla n_{\mathrm{p}}, \\ \vec{\Gamma}_{\mathrm{n}} &= -n_{\mathrm{n}} \mu_{\mathrm{n}} \vec{E} - D_{\mathrm{n}} \nabla n_{\mathrm{n}}, \\ \vec{\Gamma}_{\mathrm{e}} &= -n_{\mathrm{e}} \mu_{\mathrm{e}} \vec{E} - D_{\mathrm{e}} \nabla n_{\mathrm{e}}. \end{aligned} \tag{2.2}$$

The rate coefficients of impact ionization, attachment and recombination are denoted as α, β and r, respectively. The transport coefficient of mobility and diffusion are denoted as μ_{i} and D_{i} (i = p, n, e). These coefficients are determined by the local reduced electric field strength, which is consistent with the solution of Boltzmann equation in the local thermal-equilibrium approximation [68]. The following expression for the ionization coefficient α in atmospheric air is used [87]:

$$\alpha(\mathrm{cm}^{-1}) = \begin{cases} 3.9P \exp(-213P/E) & \text{for} \quad E/P < 108, \\ 14.5P \exp(-356P/E) & \text{for} \quad E/P > 108, \end{cases} \tag{2.3}$$

where P is the pressure, in Torr[1], and $E = \|\vec{E}\|$ is the magnitude of electric field, in V/cm. We consider the atmospheric plasma, i.e., $P = 760$ Torr. The attachment coefficient β is given by [87]

$$\beta(\mathrm{cm}^{-1}) = \begin{cases} \max(4.47P/E, 4.47 \times 10^{-3}(E/P)^2) & \text{for} \quad E/P < 10, \\ 4.47 \times 10^{-3}(E/P)^2 & \text{for} \quad 10 < E/P < 50, \\ 1.58\sqrt{E/P} & \text{for} \quad 50 < E/P < 90, \\ 142/\sqrt{E/P} & \text{for} \quad E/P > 90. \end{cases} \tag{2.4}$$

The electron mobility coefficient μ_e is given by [88]

$$\mu_\mathrm{e}(\mathrm{cm}^2\mathrm{V}^{-1}\mathrm{s}^{-1}) = 6.06 \times 10^3 E^{0.75}, \tag{2.5}$$

while the mobility coefficients of positive and negative ions are given by [83]

$$\mu_\mathrm{p}(\mathrm{cm}^2\mathrm{V}^{-1}\mathrm{s}^{-1}) = \mu_\mathrm{n} = \frac{2.0 \times 10^3}{P}. \tag{2.6}$$

The diffusion coefficients are set based on the Einstein relation: $D_\mathrm{e}/\mu_\mathrm{e} = 1$ V, $D_\mathrm{p,n}/\mu_\mathrm{p,n} = 0.01$ V.

The electric field $\vec{E}$ is obtained as

$$\vec{E} = -\nabla\boldsymbol{\phi}. \tag{2.7}$$

The electric potential $\boldsymbol{\phi}$ is obtained by solving the Poisson equation,

$$\nabla \cdot (-\varepsilon\nabla\boldsymbol{\phi}) = \frac{c(n_\mathrm{p} - n_\mathrm{n} - n_\mathrm{e})}{\varepsilon_0} + \frac{c}{\varepsilon_0}\sigma_\mathrm{s}\delta_\mathrm{s}, \tag{2.8}$$

[1]defined as exactly 1/760 of the standard atmosphere (i.e., 1 Torr ≈ 133.32 Pa).

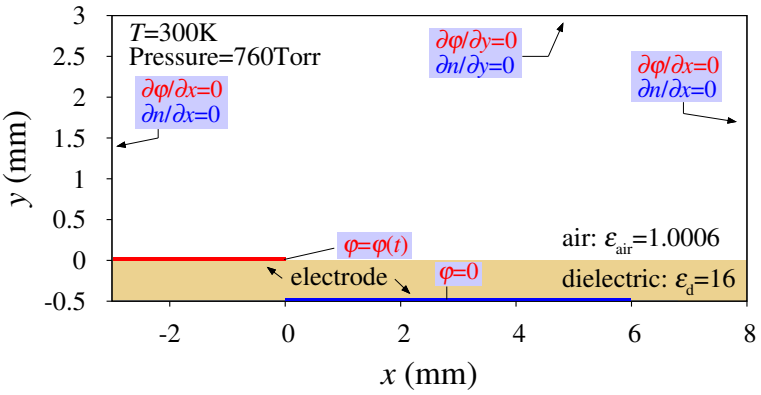

Figure 2.1: Computational domain and boundary conditions.

where ε_0 denotes the permittivity of vacuum, while ε is the relative permittivity; c is the elementary charge. The surface free charge number density σ_s is non-zero only on the dielectric surface, as expressed by the Dirac delta function δ_s.

2.2 Computational domain and boundary conditions

The computational domain is shown in Fig. 2.1, which is a 8 mm $\times$ 3.5 mm rectangular box. The widths of the upper and lower electrodes are 3 mm and 6 mm, respectively, and the thickness of the upper electrode is 80 μm. The streamwise distance between two electrodes is zero, and the electrodes are separated by the dielectric layer in the thickness of 0.5 mm.

As for the charged particle number density, Neumann boundary conditions are used at the top, left and right side of the domain and the dielectric surface (i.e., $\partial n_i/\partial \vec{n} = 0,\ i = p, n, e$). At the dielectric surface, surface charge and secondary electron emission are taken into consideration. When the positive ions flow towards

the dielectric surface, secondary electron emission occurs, i.e.,

$$j_{\mathrm{e}\,y} = -\gamma j_{\mathrm{p}\,y}, \text{ if } \Gamma_{\mathrm{p}\,y} < 0, \text{ at the interface.} \tag{2.9}$$

Here, $j_{\mathrm{e}\,y}$, $j_{\mathrm{p}\,y}$ are the wall-normal (y) component of current density of electrons and positive ions respectively, which is calculated by multiplying the wall-normal component of charged particle flux and elementary charge, i.e., $j_{\mathrm{i}\,y} = c\Gamma_{\mathrm{i}\,y}$ (i = p, n, e) ; γ is the secondary electron emission coefficient, which is set to $\gamma = 0.05$ in the present study.

It is should be noted that, on the dielectric surface, surface charge accumulation plays an important role in the discharge propagation and the generation of EHD body force [62, 89–93]. The accumulation of the surface charge is determined by the transport of charged particles to the dielectric surface. As the results, the boundary condition of the charged particles on the dielectric surface seems to be extremely important to the fluid-model simulation of a SDBD plasm actuator. In the recent review paper [89], the accurate formulation of boundary conditions for electron density on the dielectric surface is listed as a key technical issues that need to be resolved for adequate numerical simulations of SDBD plasma actuator. However, in previous publications, no consensus on the boundary condition of charged particle density at the dielectric surface has been reached. Note that we have also carried out numerical tests using two other boundary conditions: 1) the boundary condition described in Zhu et al. [49], i.e., a combination of zero gradient of flux for flow towards boundary and zero flux for flow away from boundary; 2) zero-diffusion flux for both flows towards and away from boundary. In both cases, secondary electron emission is added as described above. The present computations have shown that the results do not visibly depend on the boundary condition on the dielectric surface mentioned above when a sufficiently fine grid resolution (discussed in chapter 3) is

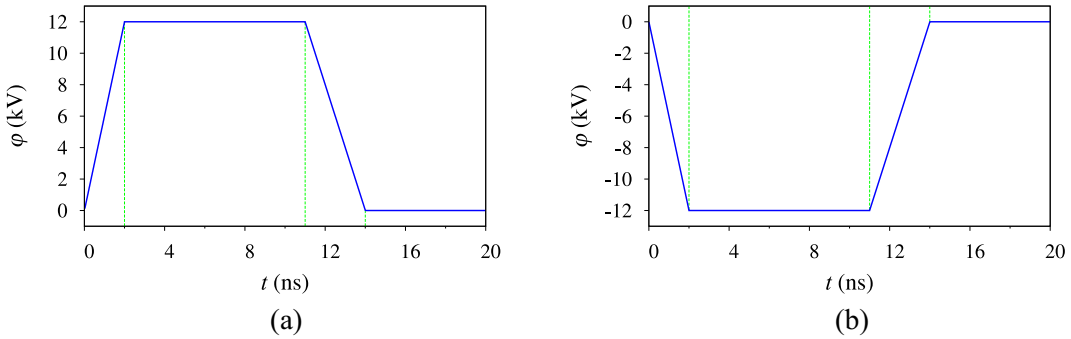

Figure 2.2: Applid nanosecond voltage pulse signal on the upper electrode: (a) positive polarity; (b) negative polarity.

used.

For the electric potential, Neumann boundary conditions are used at the top, left, right and bottom side of the domain (i.e., $\partial\boldsymbol{\phi}/\partial\vec{n} = 0$), while Dirichlet boundary conditions are adopted on the electrodes. High voltage signal is adopted to the upper electrode, i.e.,

$$\boldsymbol{\phi}_{\text{upper}} = \phi(t). \tag{2.10}$$

As shown in Fig. 2.2, the voltage signal used in the present study is a 14 ns duration nanosecond pulse with 2 ns rising time and 3 ns falling time, and the amplitude of the voltage is 12 kV, which is the same as Ref. [47]. Both positive pulse and negative pulse are considered. The waveform of the negative voltage pulse has a reversed profile with the same voltage amplitude as the positive voltage pulse.

The lower electrode is grounded, i.e.,

$$\boldsymbol{\phi}_{\text{lower}} = 0.$$

At the interface of air and dielectric layer, the electric field is described by the Maxwell equations. According to the Ampere Circuits Theorem, the integrals of

electric field strength along the circuit is equal to zero, i.e.,

$$\oint \vec{E} \cdot d\vec{l} = 0.$$

At the interface, when $\delta y \to 0$, we can get,

$$E_{x1} = E_{x2}, \tag{2.11}$$

namely, the streamwise component of electric field is continues at the interface.

On the other hand, according to the Gauss law, the integrals of the electric displacement $\vec{D}$ $(= \varepsilon \vec{E})$ along the surface is equal to the surface free charge Q_s [C] in the integral domain, i.e.,

$$\oint \vec{D} \cdot dS = Q_s.$$

Similarly, at the interface, when $\delta y \to 0$, we can get,

$$\varepsilon_1 E_{y1} - \varepsilon_2 E_{y2} = q_s. \tag{2.12}$$

Here, q_s [C/m^2] is the surface free charge areal density. Note that surface free charge Q_s, surface free charge areal density q_s and surface free charge number density σ_s [m^{-3}] in Eq. (2.8) are different. The relationship between the three variables are as follows,

$$Q_s = q_s S_s = c\sigma_s V_s,$$

$$q_s = c\sigma_s \Delta y_1,$$

where S_s, V_s and Δy_1 are the volume of the interface cell, the area of the interface cell on the dielectric surface and the grid spacing at the interface of dielectric and air, as shown in Fig. 2.4.

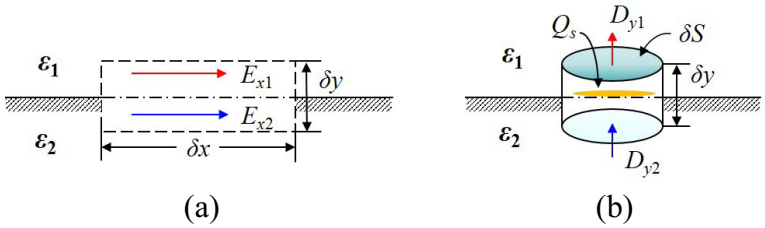

Figure 2.3: Electric field at the interface

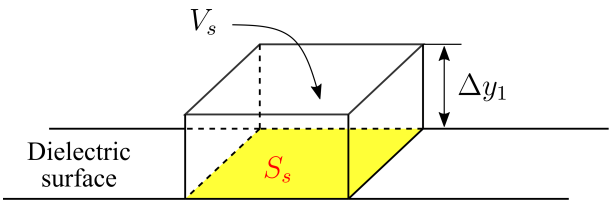

Figure 2.4: Schematic of the interface cell.

The surface free charge number density is obtained by temporally integrating the charged particle fluxes to the dielectric surface [39, 74], i.e.,

$$\sigma_s(t)\ [\mathrm{m}^3] = \frac{1}{\Delta y_1}\int_0^t \left[-\Gamma_{\mathrm{p}\,y}(t) + \Gamma_{\mathrm{n}\,y}(t) + \Gamma_{\mathrm{e}\,y}(t)\right]|_{y=0} dt. \tag{2.13}$$

Note that electrons and ions in each surface element cell are supposed to recombine instantly.

2.3 Spatial discretization and time integration

Finite difference method is used to solve the governing equations. The computation is conducted in the two-dimensional Cartesian system. The grid is equispaced in the streamwise (x) direction and stretched in the wall-normal (y) direction. Staggered grid is adopted, with the scalar variables, e.g., electric potential $\boldsymbol{\phi}$, charged particle number densities n_{p}, n_{n}, n_{e} defined at the cell center, and the vectors, e.g., electric field (E_x, E_y), drift-diffusion flux (Γ_x, Γ_y) defined at the cell edges, as shown in Fig. 2.5.

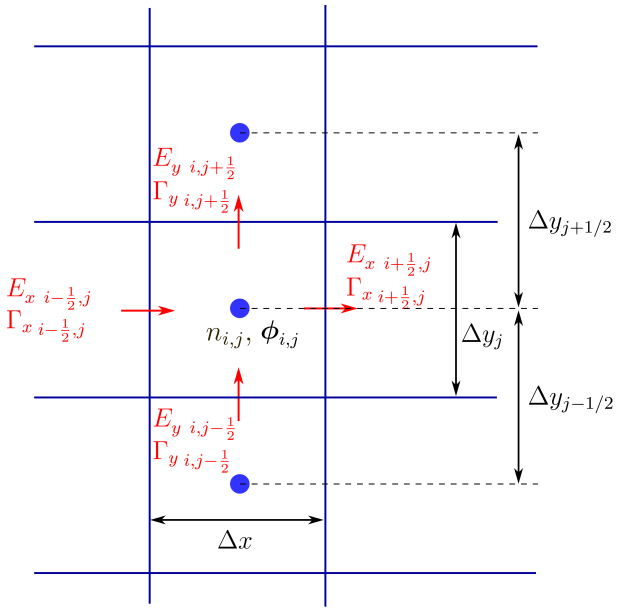

Figure 2.5: Staggered grid defined in the computation.

The drift-diffusion terms are discretized using the Scharfetter-Gummel (SG) scheme [94], which has been proven to be numerically stable when the electric field is strong. Time integration for the transport equations is conducted using the Euler explicit scheme. Therefore, the discretized formula for the transport equation of positive ions (i.e., Eq. (2.1(a))) is given as

$$\begin{aligned}\frac{n_{\mathrm{p}\,i,j}^{t+1}-n_{\mathrm{p}\,i,j}^{t}}{\Delta t}=&\frac{\Gamma_{\mathrm{p}x\,i+1/2,j}^{t}-\Gamma_{\mathrm{p}x\,i-1/2,j}^{t}}{\Delta x}+\frac{\Gamma_{\mathrm{p}y\,i,j+1/2}^{t}-\Gamma_{\mathrm{p}y\,i,j-1/2}^{t}}{\Delta y_j}\\&+\alpha_{i,j}^{t}n_{\mathrm{e}\,i,j}^{t}\mu_{\mathrm{e}\,i,j}^{t}\|\vec{E}\|_{i,j}^{t}-rn_{\mathrm{p}\,i,j}^{t}n_{\mathrm{e}\,i,j}^{t}-rn_{\mathrm{p}\,i,j}^{t}n_{\mathrm{n}\,i,j}^{t}.\end{aligned}\tag{2.14}$$

The transport equations for negative ions and electrons are discretized similarly.

The Poisson equation is discretized as

$$\begin{aligned}\Big[\frac{2}{\Delta x^2}+\frac{1}{\Delta y_{j-1/2}\Delta y_j}+\frac{1}{\Delta y_{j+1/2}\Delta y_j}\Big]\boldsymbol{\phi}_{i,j}=&\frac{1}{\Delta x^2}\boldsymbol{\phi}_{i-1,j}+\frac{1}{\Delta x^2}\boldsymbol{\phi}_{i+1,j}\\&+\frac{1}{\Delta y_{j-1/2}\Delta y_j}\boldsymbol{\phi}_{i,j-1}+\frac{1}{\Delta y_{j+1/2}\Delta y_j}\boldsymbol{\phi}_{i,j+1}+\frac{c(n_{\mathrm{p}}-n_{\mathrm{n}}-n_{\mathrm{e}}+\delta_s\sigma_s)}{\varepsilon},\end{aligned}\tag{2.15}$$

which is solved by using the successive over relaxation (SOR) method with a convergence criterion set to 10^{-6}.

However, at the interface of air and dielectric layer, the discretization of Poisson equation should be consistent with the Gauss law (Eq. (2.12)). Because of the existence of surface free charge and the difference in permittivity between dielectric layer and air, the wall-normal (y) component of the electric field at the interface E_{y0} can no longer be calculated as the gradient of electric potential $\boldsymbol{\phi}$. First we consider the one dimension problem in wall-normal direction, as shown in Fig. 2.6. According to the Gauss law (Eq. (2.12)), the wall-normal component of electric field is not continuous at the interface. Here, the wall-normal components of electric field on the side of air and dielectric layer are denoted as E_{0+} and E_{0-}, respectively. The Eq. (2.12) can be expressed as

$$\varepsilon_{\mathrm{air}}\varepsilon_0 E_{0+} - \varepsilon_{\mathrm{d}}\varepsilon_0 E_{0-} = c\sigma_s \Delta y_1. \tag{2.16}$$

On the other hand, according to the relation between electric field and electric potential,

$$0.5\Delta y_1 E_{0+} + 0.5\Delta y_0 E_{0-} = \boldsymbol{\phi}_0 - \boldsymbol{\phi}_1. \tag{2.17}$$

By solving Eqs. (2.16) and (2.16), we can obtain E_{0+} and E_{0-},

$$\begin{aligned} E_{0+} &= \frac{c\sigma_s \Delta y_1 \Delta y_0 + 2\varepsilon_{\mathrm{d}}(\boldsymbol{\phi}_0 - \boldsymbol{\phi}_1)}{\varepsilon_{\mathrm{air}}\varepsilon_0 \Delta y_0 + \varepsilon_{\mathrm{d}}\varepsilon_0 \Delta y_1}, \\ E_{0-} &= \frac{-c\sigma_s \Delta y_1 \Delta y_1 + 2\varepsilon_{\mathrm{air}}\varepsilon_0(\boldsymbol{\phi}_0 - \boldsymbol{\phi}_1)}{\varepsilon_{\mathrm{air}}\varepsilon_0 \Delta y_0 + \varepsilon_{\mathrm{d}}\varepsilon_0 \Delta y_1}. \end{aligned} \tag{2.18}$$

Now we consider the Gauss law for the interface cell (blue color in Fig. 2.6), i.e.,

$$\frac{1}{\Delta y_1}(E_1 - E_{0+}) = \frac{n_{\mathrm{p}} - n_{\mathrm{n}} - n_{\mathrm{e}}}{\varepsilon_{\mathrm{air}}\varepsilon_0}. \tag{2.19}$$

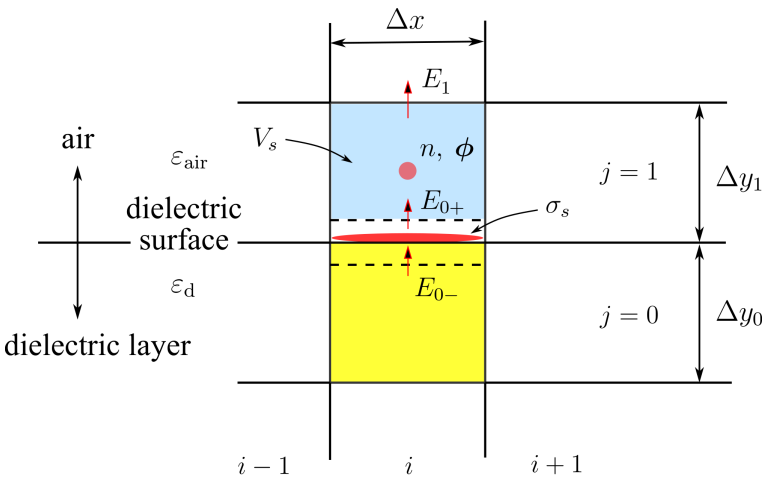

Figure 2.6: Grid configuration at the interface.

Note that the surface free charge is not exist in the right hand side of Eq. (2.19), for surface free charge is not in the volume V_s (blue color in Fig. 2.6). Substituting Eq. (2.18) into Eq. (2.19), we can obtain,

$$\frac{1}{\Delta y_1}\left(\frac{\boldsymbol{\phi}_1-\boldsymbol{\phi}_2}{\Delta y_{3/2}}-\frac{c\sigma_s\Delta y_1\Delta y_0+2\varepsilon_d\varepsilon_0(\boldsymbol{\phi}_0-\boldsymbol{\phi}_1)}{\varepsilon_{\text{air}}\varepsilon_0\Delta y_0+\varepsilon_d\varepsilon_0\Delta y_1}\right)=\frac{c(n_{\text{p}}-n_{\text{n}}-n_{\text{e}})}{\varepsilon_{\text{air}}}. \tag{2.20}$$

We can easily extend the formula from one-dimensional problem to two-dimensional problem, as expressed in Eq. (2.21).

$$\begin{aligned}\frac{-\boldsymbol{\phi}_{i-1,1}+2\boldsymbol{\phi}_{i,1}-\boldsymbol{\phi}_{i+1,1}}{\Delta x^2}+\frac{1}{\Delta y_1}\left(\frac{\boldsymbol{\phi}_{i,1}-\boldsymbol{\phi}_{i,2}}{\Delta y_{3/2}}-\frac{c\sigma_{s\,i}\Delta y_1\Delta y_0+2\varepsilon_d\varepsilon_0(\boldsymbol{\phi}_{i,0}-\boldsymbol{\phi}_{i,1})}{\varepsilon_{\text{air}}\varepsilon_0\Delta y_0+\varepsilon_d\varepsilon_0\Delta y_1}\right)\\ =\frac{c(n_{\text{p}}-n_{\text{n}}-n_{\text{e}})}{\varepsilon_{\text{air}}\varepsilon_0}.\end{aligned} \tag{2.21}$$

Finally, the Poisson equation at the interface is descretized as

$$\begin{aligned}
&\Big(\frac{2}{\Delta x^2}+\frac{1}{\Delta y_1\Delta y_{3/2}}+\frac{2\varepsilon_d\varepsilon_0}{\Delta y_1\varepsilon_{\text{air}}\varepsilon_0\Delta y_0+\Delta y_1\varepsilon_d\varepsilon_0\Delta y_1}\Big)\boldsymbol{\phi}_{i,1}\\
&=\frac{1}{\Delta x^2}\boldsymbol{\phi}_{i-1,1}+\frac{1}{\Delta x^2}\boldsymbol{\phi}_{i+1,1}+\frac{2\varepsilon_d\varepsilon_0\boldsymbol{\phi}_{i,0}}{\Delta y_1\varepsilon_{\text{air}}\varepsilon_0\Delta y_0+\Delta y_1\varepsilon_d\varepsilon_0\Delta y_1}+\frac{1}{\Delta y_1\Delta y_{3/2}}\boldsymbol{\phi}_{i,2}\\
&+\frac{c(n_{\text{p}}-n_{\text{n}}-n_{\text{e}})}{\varepsilon_{\text{air}}\varepsilon_0}+\frac{c\sigma_{s\,i}\Delta y_1\Delta y_0}{\Delta y_1\varepsilon_{\text{air}}\varepsilon_0\Delta y_0+\Delta y_1\varepsilon_d\varepsilon_0\Delta y_1}.
\end{aligned}\tag{2.22}$$

The initial density for positive ions and electrons is uniform and equal to 10^9 cm^{-3} in the air domain. While the time step in explicit solution of transport equations is constrained by several time scales, including the CFL (Courant-Friedrichs-Lewy) number, the effective ionization and dielectric relaxation time scales [49, 95, 96]. Among them, the dielectric relaxation time scales severely restricts the time step in the simulation [84], which is smaller than 10^{-12} s with a plasma density of 10^{20} m^{-3}. Here, a brief explanation on the dielectric relaxation time scales is provided. The dielectric relaxation reveals how long it takes the plasma respond to a disturbance in the charge density. Assuming a simple one-dimensional problem, some disturbance in the charge equilibrium somewhere, expressed as Δn, will lead to the disturbance in electric field, which is governed by the one-dimensional Poisson equation,

$$\frac{dE}{dx}=-\frac{c\Delta n}{\varepsilon\varepsilon_0}.\tag{2.23}$$

However, the Poisson equation does not explicitly contain the time dependence. If we want to find out about how long it takes to establish a steady state, we need some expression for dn/dt. For quasi-neutral plasma, we can neglect the diffusion terms in continuity equation, which leaves us with the following simplified

continuity equation,

$$\frac{\partial \Delta n}{\partial t} = -n\mu \frac{\partial E}{\partial x}. \tag{2.24}$$

Substituting (2.23) into (2.24), we can get,

$$\frac{\partial \Delta n}{\partial t} = -\frac{cn\mu}{\varepsilon\varepsilon_0}\Delta\rho. \tag{2.25}$$

The analytical solution of (2.25) is

$$\Delta\rho(x,\, t) = \Delta\rho(x,\, 0)\exp(-t/\tau_d), \tag{2.26}$$

where,

$$\tau_d = \frac{\varepsilon\varepsilon_0}{c\mu\rho_0},$$

is the dielectric relaxation time.

On the other hand, the characteristic time associated with the transport of electron can be as small as some picoseconds [97]. Hence, the time step in the present simulation is set to be $\Delta t = 10^{-14}$ s to obtain a sufficient time resolution for discharge propagation to analyze the transport of charged particles.

Chapter 3

Influence of grid resolution in fluid-model simulation of NSDBD

3.1 Introduction

It is widely accepted that the generated thrust or the fast heating from high-voltage discharge are the mechanisms of flow control or plasma-assisted ignition and combustion. In order to understand the discharge process and obtain the spatial and temporal distribution of generated body force and heat, experimental and numerical studies on SDBD plasma actuators have extensively been conducted [1, 20, 23, 38–49]. Experimental results show that the dielectric barrier discharge consists of numerous micro-discharges with a short duration of some 10 ns.

The fluid model couples the transport equation of positive ions, negative ions and electrons with the Poisson equation for the electric potential. Compared with the kinetic model, the fluid model is computationally cheaper; however, in order to resolve the discharge formation, a sufficiently fine computational grid and a short time step are required. In the previous studies on SDBD plasma actuator using the fluid model [39, 41, 43, 47, 74, 75, 82, 83, 98], both the discharge structure and the generated body force are investigated, but the computational grid spacing used in

these studies are significantly different from one another: it ranges from $1 - 100$ μm. It is hardly known whether the results are grid-convergent and it is hard to say whether the obtained results are reasonable enough to analyze the discharge process and the mechanism of body force generation. Boeuf et al. [74] checked the accuracy of numerical simulations by comparing the integrated body force obtained with different grid spacings. In the case of negative voltage slope, the body force computed using 2.5 μm wall-normal grid spacing was found to be approximately 3 times smaller than that using 10 μm grid spacing. Soloviev and Krivtsov [77] claim that the grid spacing should be less than $1 - 2$ μm (and they actually used the grid spacing less than 2 μm) and the time step less than $10^{-14} - 10^{-13}$ s. It indicates that the wall-normal grid spacing is very important for the accuracy of fluid-model simulation of SDBD plasma actuator. Besides, it should be reminded that the discharge structure is the consequence of transport of charged particles, including ions and electrons. In the previous numerical studies, however, most attentions have been paid in the discharge structure and the generated body force, while the detailed transport mechanisms of ions and electrons inside the plasma have not sufficiently been investigated.

An SDBD excited by a single pulse of a few tens of nanosecond duration is not only useful to understand the mechanism of a nanosecond-pulse SDBD actuator, but also an attractive object to study the physics of SDBD because only one microdischarge is generated over the pulse time [79]. In the present study, we first examine different grid configurations and compare the obtained results to see whether and how the discharge structure is qualitatively influenced by the grid spacing. Subsequently, the transport of charged particles (in particular, electrons) computed using different grid resolutions is analyzed to explain the effect of grid resolution on the accuracy of discharge evolution simulation.

Table 3.1: Test cases for grid dependence study.

Case	Δx [μm]	Δy_1 [μm]	Computational cells ($N_x \times N_y$)
PG-1	20	0.625	650×374
PG-2 (Reference case)	10	0.625	1100×374
PG-3	5	0.625	2200×244
PG-4	10	10	1100×83
PG-5	10	5	1100×184
PG-6	10	2.5	1100×244
PG-7	10	1.25	1100×308
PG-8	10	0.3125	1100×443

3.2 Numerical accuracy for different grid resolution

A systematic study is conducted to investigate the influence of grid resolution on the accuracy of plasma simulation. Besides, transport of charged particles is analyzed to explain the different discharge structures computed by different grid resolutions.

In order to obtain grid-convergent results, 8 cases with different grid configuration shown in Table 3.1 are investigated and compared. Note that in the present study, uniform grid is used in the streamwise (x) direction, while non-uniform grid is adopted in the wall-normal (y) direction. In the table, Δy_1 denotes the grid spacing at the interface of dielectric and air. Cases PG-1–3 study the influence of streamwise spacing on the results, while Cases PG-2, 4–8 study the influence of wall-normal spacing.

Before discussing the dependence on grid resolution, we quickly take a look at time evolutions of the charged particle density and the electric field computed with $\Delta x = 10$ μm and $\Delta y_1 = 0.625$ μm (Fig. 3.1), which we refer to as the reference case (Case PG-2). The results show that a streamer of plasma forms in the vicinity of the upper electrode when a positive voltage is applied, which is consistent with earlier experimental [1] and numerical [47] observations. The densities of positive

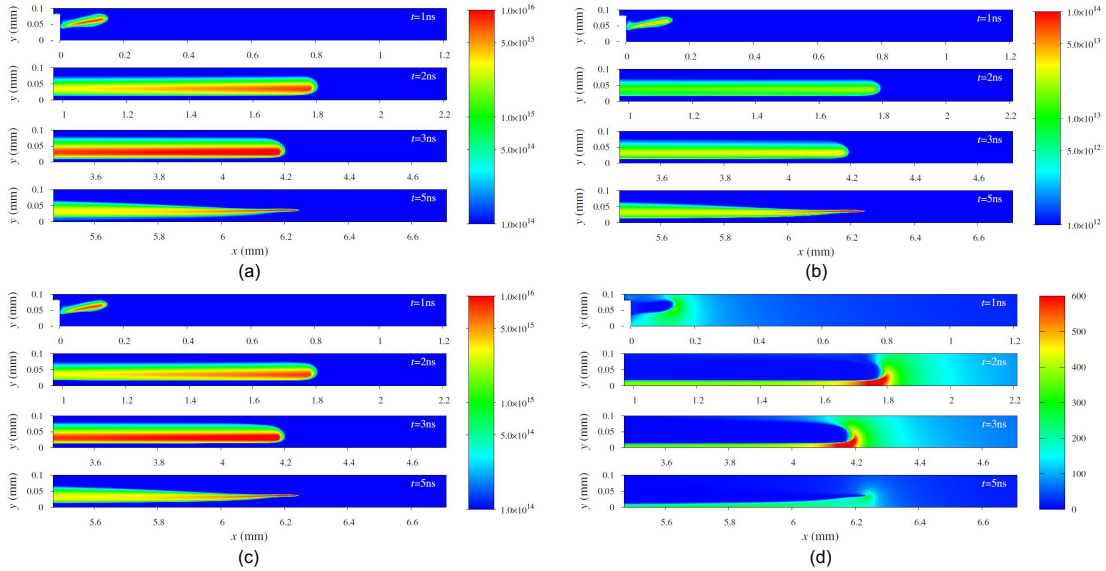

Figure 3.1: Discharge evolution computed with the reference grid resolution ($\Delta x = 10$ μm, $\Delta y_1 = 0.625$ μm): (a) positive ion (cm^{-3}); (b) negative ion (cm^{-3}); (c) electron (cm^{-3}); (d) electric field strength (kV/cm).

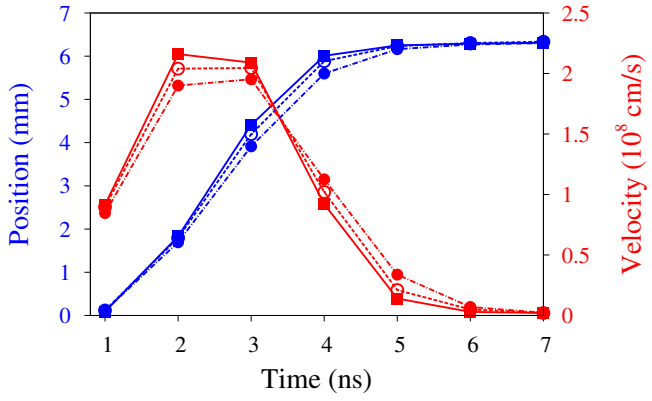

Figure 3.2: Head position and velocity of discharge streamer computed with different Δx. Blue line, head position; red line, velocity. Solid line, $\Delta x = 20$ μm, dashed line, $\Delta x = 10$ μm, one-dot chain line, $\Delta x = 5$ μm.

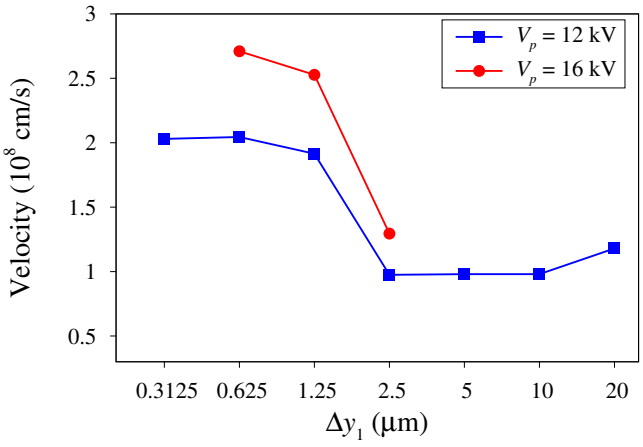

Figure 3.3: Discharge streamer propagation velocity at $t = 2$ ns computed with different Δy_1.

ions and electrons can reach 10^{16} cm^{-3} in the streamer region, whereas the density of negative ions is much lower. The streamer propagates along the the dielectric surface with a high electric field around its head (Fig. 3.1(d)).

Dependence of the head position and the velocity of the discharged streamer on Δx is shown in Fig. 3.2. Here, Δy_1 is fixed at $\Delta y_1 = 0.625$ μm. The head position and the propagation velocity show little difference. Even at the time instant when the largest difference is observed, i.e., $t = 2$ ns, the difference in the propagation velocity between Case PG-2 ($\Delta x = 10$ μm) and the twice finer case, Case PG-3 ($\Delta x = 5$ μm), is less than 7%. Therefore, it can be concluded that the result is relatively insensitive to Δx.

Surface charges play an important role in the plasma discharge process; therefore, calculation of the surface charge density should significantly influence the accuracy of plasma simulation. As described in Section 2.2, the surface charge density is calculated as the time integration of wall-normal fluxes of positive ions, negative ions and electrons into the dielectric surface; hence, the first wall-normal grid spacing adjacent to the surface Δy_1 is extremely important. Figure 3.3 shows

the discharge propagation velocity at $t = 2$ ns for different Δy_1 with the same Δx (i.e., $\Delta x = 10$ μm). When Δy_1 is decreased from 20 μm to 2.5 μm, the streamer propagation velocity at 2 ns is kept nearly constant at about 1×10^8 cm/s. However, when Δy_1 is further decreased to 1.25 μm, the computed velocity is abruptly doubled and kept nearly constant at about 2×10^8 cm/s for smaller Δy_1. Similar abrupt increase is also observed when the applied voltage is increase to $V_p = 16$ kV. The abrupt increase of velocity indicates that the structure of plasma discharge is not accurately captured with $\Delta y_1 = 2.5$ μm.

The near-surface discharge evolution for Case PG-6 ($\Delta y_1 = 2.5$ μm) depicted in Fig. 3.4 clearly shows the difference in the streamer structure from that computed with $\Delta y_1 = 0.625$ μm. The discharge streamer of Case PG-6 ($\Delta y_1 = 2.5$ μm) is attached to the dielectric surface, and the density of charged particles is much higher near the dielectric surface. In contrast, the discharge streamer of Case PG-2 ($\Delta y_1 = 0.625$ μm) is detached and the densities of charged particles between the streamer and dielectric are very small, which is consistent with the observations in the previous studies that used a refined ionization rate [77, 99] and that used a particle-in-cell approach instead of fluid model [67]. Namely, the present result suggests that the grid spacing recommended in the previous study [74] (i.e., $\Delta y_1 =$ 7 μm) is not sufficiently fine to correctly capture the discharge structure with a narrow gap adjacent to the surface.

Figure 3.5 shows the distributions of electric field and particle number density in the cross-section of $x = 0.5$ mm at different time instants obtained in Case PG-2. It is clearly shown that, at $t = 2$ ns, a region of low ion and electron density and high electric field (i.e., plasma sheath) exists below $y = 20$ μm. With the propagation of the discharge, this region shrinks and the electron-ion density in the streamer region decreases as well. However, in Case PG-6 (i.e., the case with the

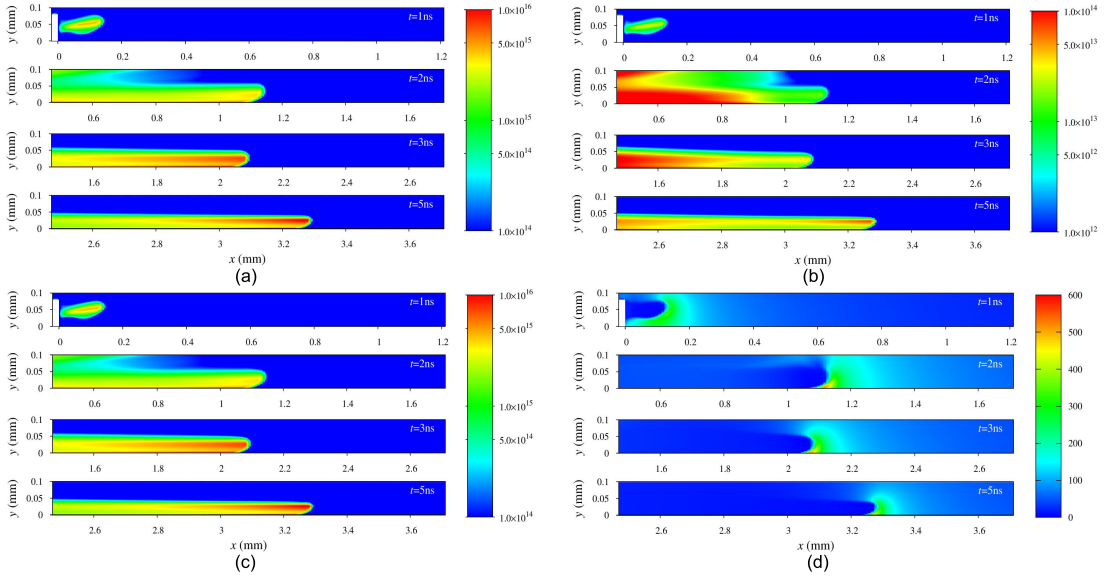

Figure 3.4: Discharge evolution in Case PG-6 (Δx = 10 μm, Δy_1 = 2.5 μm): (a) positive ion (cm^{-3}); (b) negative ion (cm^{-3}); (c) electron (cm^{-3}); (d) electric field strength (kV/cm).

coarser y grid), this low electron region is not resolved. As a result, the densities of charged particles in the first wall-normal layer adjacent to the surface become extremely high.

The computed streamer propagation is compared with Babaeva et al. [47], who used the same voltage shape and similar geometry. Figure 3.6 shows the time history of the streamer position away from the upper electrode. The streamer head

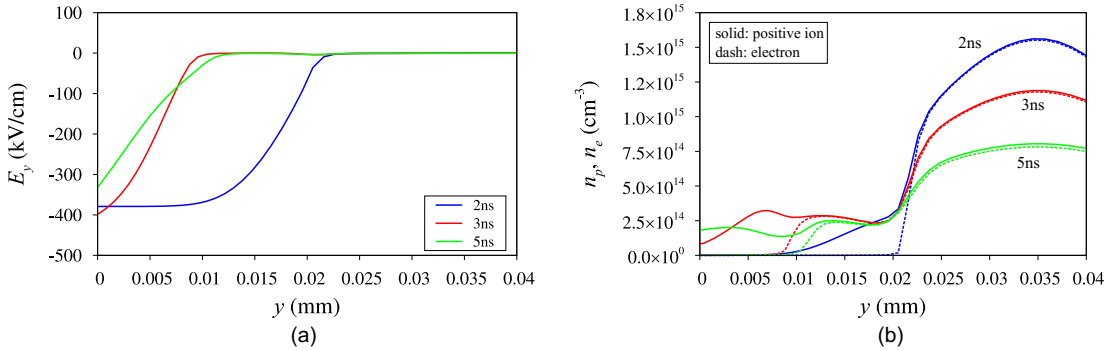

Figure 3.5: Wall-normal distribution of (a) wall-normal electric field and (b) electron-ion density in cross-section x=0.5 mm in Case PG-2 (Δx = 10 μm, Δy_1 = 0.625 μm).

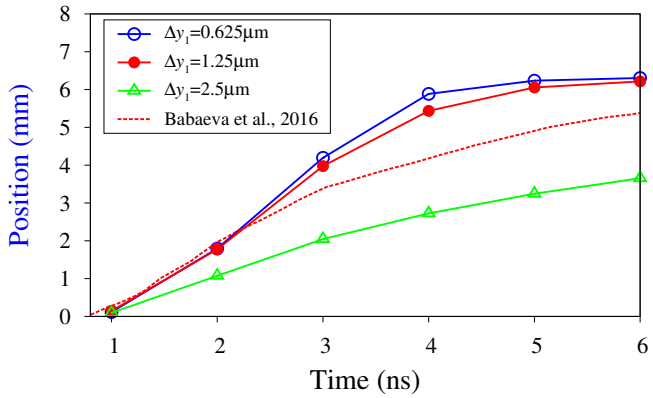

Figure 3.6: Time trace of the streamer position compared with the previous simulation by Babaeva et al. [47] considering detailed reactions.

position before 2 ns is in good agreement with Babaeva et al. [47], but deviation is observed after 2 ns. This difference is likely to come from the physical model and numerical configuration used. Babaeva et al. [47] considered 13 species and 77 reactions to describe the reaction mechanism in plasma discharge, while the present study used a standard plasma fluid model considering positive ions, negative ions and electrons. In contrast, the wall-normal grid resolution near the dielectric surface, which has been shown to have significant impact on the result, used in the present study is much finer than that of Babaeva et al. [47] whose finest resolution is about 3 μm. Considering the differences above, the present result is considered to be in reasonable agreement with the previous numerical study. Besides, the numerical result is compared with previous experimental results by Zhu et al., [49], as shown in Fig. 3.7. The amplitude of the nanosecond voltage pulse is $V_p = 24$ kV. It is found that the position of the streamer head is in good agreement with the experimental results, although slight deviation occurs due to the restriction of the width of lower electrode, which is 20 mm in the simulation due to the high computational cost.

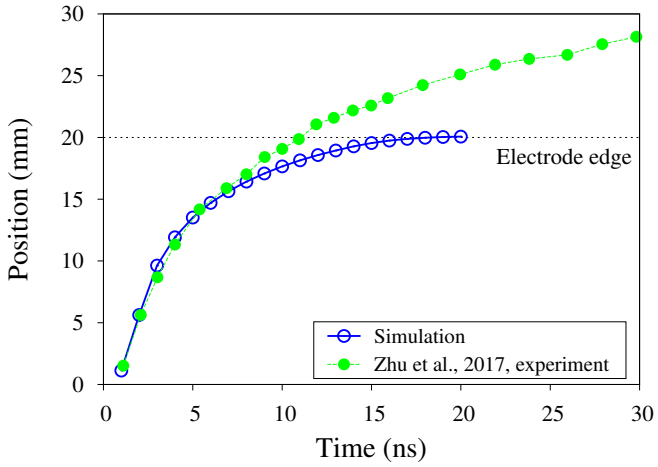

Figure 3.7: Time trace of the streamer position compared with the previous experimental results by Zhu et al. [49].

3.3 Analysis of transport of charged particles

The difference of discharge structure of different grid resolution is the consequence of different transport of charged particles, and the analysis of charged particles' transport can help to explain the difference. In order to understand the transport of charged particles during the plasma discharge, decomposition of the variation of particle number density is considered. The variation of charged particle number density, n_i (i = p, n, e), depends on the drift-diffusion flux, ionization, attachment and recombination, which is expressed as

$$\frac{\partial n_\mathrm{p}}{\partial t} = \nabla \cdot \vec{\Gamma}_\mathrm{p} + S_\mathrm{p} - R_\mathrm{p}, \tag{3.1a}$$

$$\frac{\partial n_\mathrm{n}}{\partial t} = \nabla \cdot \vec{\Gamma}_\mathrm{n} + S_\mathrm{n} - R_\mathrm{n}, \tag{3.1b}$$

$$\frac{\partial n_\mathrm{e}}{\partial t} = \nabla \cdot \vec{\Gamma}_\mathrm{e} + S_\mathrm{e} - R_\mathrm{e}. \tag{3.1c}$$

Here, $\vec{\Gamma}_\mathrm{i}$ (i = p, n, e) are the drift-diffusion flux; S_i (i = p, n, e) are the source terms, including ionization and attachment terms, and R_i (i = p, n, e) are the sink

terms representing recombination.

As shown in Fig. 3.1, the density of negative ion is much lower than those of positive ions and electrons. On the other hand, the ionization term in Eq. (3.1) is determined by the density of electrons; in other words, transport of electrons governs the discharge process. Therefore, in this section, the decomposition is conducted for the variation of electron number density. From Eq. (3.1c), the variation of n_e consists of contributions from drift-diffusion flux, source, and sink. The contribution of drift-diffusion flux, $\nabla \cdot \vec{\Gamma}_\mathrm{i}$, can be decomposed into the contribution of streamwise flux, $\partial\Gamma_{\mathrm{i}x}/\partial x$, and the wall-normal flux $\partial\Gamma_{\mathrm{i}y}/\partial y$. Hereafter, the contributions of streamwise flux, wall-normal flux, source and sink to the variation of electron number density are denoted as $\Phi_x = \partial\Gamma_x/\partial x$, $\Phi_y = \partial\Gamma_y/\partial y$, S and R for brevity. The difference of discharge structure of different grid resolution is the near surface layer, i.e., low electron density layer for Case PG-2 ($\Delta y = 0.625$ μm) and high electron density region for Case PG-6 ($\Delta y = 2.5$ μm). Therefore, we choose the first computational cell adjacent to the surface at $x = 3$ mm to analyze the transport of electron. Hereafter, the right-hand-side terms of Eq. (3.1c) are denoted as Φ_x (i.e., streamwise flux), Φ_y (i.e., wall-normal flux), S (source) and R (i.e., sink) for brevity. Besides, in order to describe the transport direction of electron more clearly, the flux term is further decomposed to those due to the drift-diffusion flux of electron on the left, right, bottom and top sides of the control volume, denoted as f_l, f_r, f_b, f_t, respectively. When electrons flow into the control volume, the rate of change is defined as positive. Using this notation, Eq. (3.1c) can be expressed as

$$\frac{\Delta n_\mathrm{e}}{\Delta t} = f_l + f_r + f_b + f_t + S_\mathrm{e} - R_\mathrm{e}. \tag{3.2}$$

Time evolution of the electric field at this location in Case PG-2 and Case PG-6 is shown in Fig. 3.8. The x component of electric field (E_x) is defined as positive

when it directs towards the right, while the y component (E_y) is positive when it directs toward the top. The electric field affects both the drift-diffusion flux and ionization, leading to the variation of charged particle density, which in turn affects the evolution of electric field. The peak value indicates the arrival of streamer. The peak value in Case PG-6 is smaller and about 2 ns later than Case PG-2. Besides, the electric field decreases to nearly zero after the peak value instantly in Case PG-6, while the peak value of electric field in Case PG-2 is followed by a broad plateau with a slight decrease in magnitude until the applied voltage starts to decrease at $t = 11$ ns.

Time evolutions of the electron number density and the right-hand-side terms of Eq. (3.2) in Case PG-2 are shown in Fig. 3.9(a). Fig. 3.9(a) also shows the schematic diagram of the electron transport derived from the observations. Note that the sink term R_e representing recombination is not shown because it is much smaller than other five terms. There are two distinct increases of n_e at about 3 ns and 15 ns, which indicate two strokes at the leading edge and trailing edge of the voltage pulse. In the first stroke, the electric field reaches the ionization threshold with the increase of applied voltage and n_e shows an obvious increase from about 3 ns. At the same time, secondary electron emission from the dielectric surface contributes to the increase of n_e, whereas the electrons flow out of the first cell to the upper adjacent position.

From Fig. 3.8(a), we notice that the electric field strength is about 300 kV/cm during $t = 3$ ns–11 ns, which is far greater than the ionization threshold in atmospheric air (i.e., 32.28 kV/cm) [77], but n_e does not increase significantly, which indicates that discharge avalanche does not happen. This is because discharge avalanche needs both enough seed electrons and high electric field. In the present

case, even though the electric field is strong enough during $2 < t < 12$ ns, the electrons generated from ionization is compensated by the drift-diffusion flux quickly. As the results, the electron density is not sufficiently high for discharge avalanche to occur. Compared with the ionization and flux in y direction, the flux in x direction is rather small.

At the second stroke, even though the electric field is decreasing and relatively small, the transport of electrons from top side of the control volume to dielectric surface leads to considerable increase of n_e. Note that during the second stroke, E_y is still negative (namely, electron drifts toward the top side), but the significant difference in n_e between the streamer and gap region results in massive diffusion flux from the top side of the control volume down to the dielectric surface.

The present results suggest that during the discharge formation phase the drift-diffusion flux primarily governs the variation of electron number density near the dielectric surface. Strong drift-diffusion happens near the dielectric surface, and the electrons generated by ionization are immediately compensated by the drift-diffusion flux, especially by the flux in y direction, and the electron density does not increase significantly. As the result, the discharge avalanche does not happen near the dielectric surface, and a gap is formed between the streamer and the dielectric surface during the streamer propagation in spite of the considerably high electric field near the dielectric surface.

As has been observed, the discharge structure in Case PG-6 ($\Delta y_1 = 2.5$ μm) is quite different from that in Case PG-2 ($\Delta y_1 = 0.625$ μm). The time evolution of n_e, its variation rate, and the derived schematic diagram are shown in Fig. 3.9(b). Compared with Case PG-2, intense ionization is observed in Case PG-6 and the electron density is much higher. At $t = 4.5$ ns, intense ionization happens and n_e increases to 10^{17} cm^{-3} in 0.1 ns. Strong recombination is accompanied with the

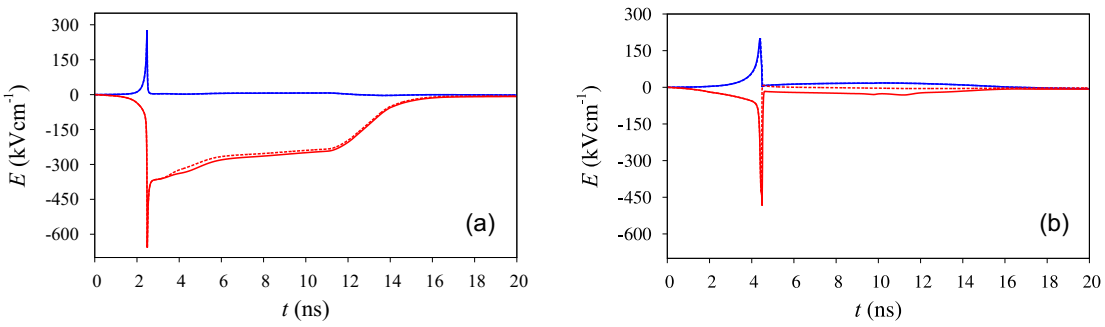

Figure 3.8: Time trace of electric field components in: (a) Case PG-2 and (b) Case PG-6. Red solid line, E_y on the bottom of control volume; red dashed line, E_y on the top; blue solid line, E_x on the left; blue dashed line, E_x on the right.

intense ionization, as shown in Fig. 3.9(b), resulting in rapid decrease of n_e. During the intense ionization, the drift-diffusion flux is almost negligible compared with the ionization and recombination, which is significantly different from Case PG-2. After the intense ionization, the electric field and ionization is weakened by the recombination, and finally, say $t > 4.6$ ns, the variation of n_e is mainly governed by the drift-diffusion flux.

As described by Eq. (3.2), the variation of electron density is determined by the balance between drift-diffusion term and source terms. In the simulation, the drift-diffusion term is discretized by SG scheme. If the grid spacing is too large, numerical diffusion can occur [74, 100]. From the results above, it is indicated that SG scheme need fine grid near the dielectric surface. If the grid resolution is not fine enough (Case PG-6), numerical diffusion will lead to the underestimation of the drift-diffusion flux and the source terms will lead to the rapid increase of electron density without sufficient balance from the drift-diffusion term.

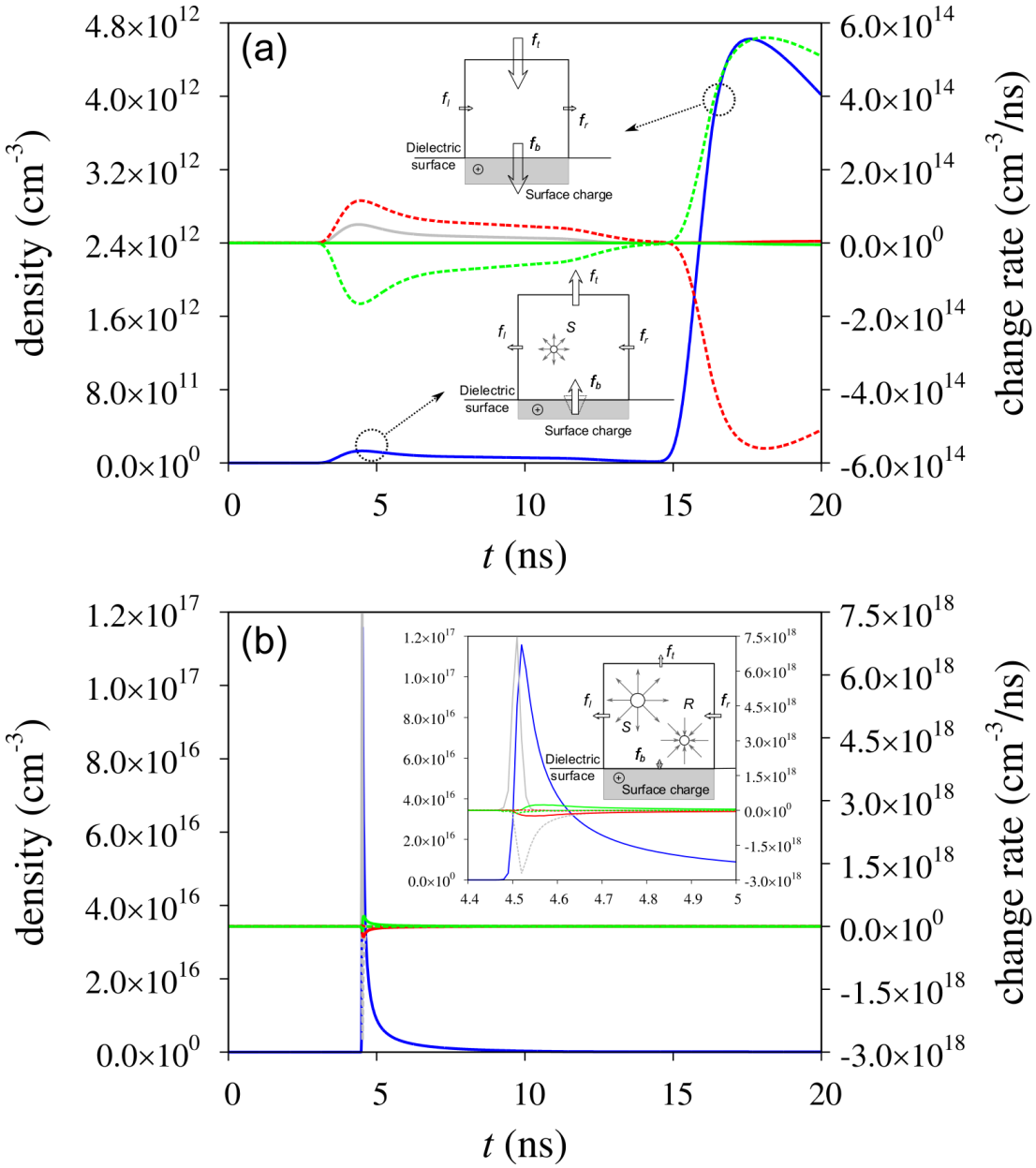

Figure 3.9: Time evolution of electron number density and its variation rate in the first cell adjacent to the surface at $x = 3$ mm: (a) Case PG-2; (b) Case PG-6. Blue solid line, n_e; gray solid line, S_e; gray dashed line, R_e; green solid line, f_r; red solid line, f_l, green dashed line, f_t; red dashed line, f_b.

3.4 Conclusions

Two-dimensional numerical simulation was performed using a plasma-fluid model to simulate the SDBD plasma actuator driven by a nanosecond voltage pulse. A special focus was laid upon the influence of grid resolution on the results in addition to the structure and dynamics of the streamer of positive nanosecond voltage pulse.

When a positive nanosecond voltage pulse is applied to the upper electrode, a streamer forms in the vicinity of upper electrode and propagates along the dielectric with a maximum propagation velocity of 2×10^8 cm/s. Because of the restriction of lower electrode's length, the streamer propagation slows down and stops after it reaches the edge of lower electrode. In the streamer region, high densities of positive ions and electrons are observed, whereas the density of negative ions is relatively small. A gap with low density of ions and electrons exists between the streamer and the dielectric surface. Such a discharge structure coincides with the previous studies that used a refined ionization rate and that used a particle-in-cell approach.

It is found that the simulation result is not very sensitive to the streamwise (x) grid spacing, whereas the wall-normal (y) grid spacing is critical to correctly reproduced the structure and dynamics of streamer. When the thickness of the first layer above the dielectric varies from 2.5 μm to 1.25 μm, the computed streamer propagation velocity abruptly increased. This result suggests that the wall-normal grid spacing is important for calculating the wall-normal flux, and a finer y grid resolution than what was recommended in the previous studies is needed near the dielectric surface.

The discharge structure is the consequence of the transport of charged particles. Decomposition of electron density variation is conducted to analyze the transport of electrons. The variation is determined by the balance between drift-diffusion

term and source terms. The transports of electrons near the dielectric surface during the nanosecond voltage pulse are found to be quite different between the cases with the finer resolution and the coarser resolution. For the case of finer resolution, the discharge structure computed is comparable with previous experimental and numerical results. The drift-diffusion flux plays the dominant role during the nanosecond pulse at the near surface position. Although the electric field at the near surface position is much higher than the ionization threshold, the balance between the drift-diffusion term and source terms maintain the electron density at a relatively low level. For the case of coarser resolution, intense ionization is observed at the near surface position, when the drift-diffusion flux is almost negligible. It is indicated that the underestimated drift-diffusion flux leads to the rapid increase of electron density.

Chapter 4

Discharge of NSDBD under different electrode polarities

4.1 Introduction

Extensive studies have been conducted to understand the detailed mechanisms of the plasma-flow interaction and to improve the EHD body force and fast gas heating by discharge plasma. It is found that the discharge morphology and plasma-flow interaction depend on the polarity of the voltage applied to the electrode. For positive polarity of the exposed electrode, the micro-discharges evolve into streamers, whereas for negative polarity the micro-discharges form more diffused plasma regions [89]. The difference in discharge morphology has been demonstrated both experimentally [1] and numerically [47, 77, 101]. Consequently, the different discharge morphology may result in different plasma-flow interactions; thus, it is important to understand the physical mechanism behind the difference to improve the EHD body force and fast gas heating by discharge plasma. The experimental study of Benard et al. [52] on the time-dependent volume force produced by sinusoidal AC voltage-driven SDBD revealed that the momentum transfer is significantly larger during the negative going cycle. Pioneering numerical studies on the

physical mechanism of EHD body force acting on the flow were conducted by Boeuf et al. [39, 75, 84]. According to the numerical results [75], the momentum transfer is due to positive ions during the positive going cycle, and to negative ions during the negative going cycle of the sinusoidal voltage. These results provide a possible explanation for the generation of EHD body force by SDBD. However, a possible shortcoming of those studies is that relatively coarse computational grid spacing of 20 μm is used, which may not be sufficiently fine to resolve the thin near-surface discharge structure [79, 85], and it is not clear how reliable the obtained results are. Soloviev et al. [77] pointed out this shortcoming and calculated the discharge evolution in air for constant voltage of positive and negative electrode polarities. In their model, a non-local air ionization by electron impact was introduced, and the discharge formation and relaxation phases were successfully simulated.

An SDBD excited by a single pulse of a few tens of nanosecond duration is not only useful to understand the mechanism of an nanosecond-pulsed SDBD plasma actuator, but also an attractive object to study the physics of SDBD because only one micro-discharge is generated over the pulse time. However, most of the previous numerical studies on SDBD consider a constant, linear or sinusoidal voltage waveform [79]. Recently, Soloviev et al. [79] studied SDBD initiated by a high nanosecond voltage pulse of negative electrode polarity. It was shown that two discharge strokes were observed corresponding to the leading and trailing edges of the voltage pulse. Babaeva et al. [47] investigated nanosecond pulsed SDBD of positive and negative electrode polarities using both a conventional fluid model and a hybrid model. The hybrid model treats the energetic secondary electrons in a fully kinetic way by using electron Monte Carlo simulation. Special attentions were paid on the influence of energetic secondary electrons. In the previous numerical studies on SDBD driven by nanosecond voltage pulse [41, 47, 49, 78, 84, 85],

however, a systematic comparison of the entire discharge process under different polarities has not been conducted, although comprehensive understanding based on such a systematic study is an important step toward improvement of SDBD plasma actuators.

In chapter 3, we have investigated the influence of grid spacing on the fluid-model simulation of nanosecond dielectric-barrier-discharge, and showed that much finer wall-normal grid spacing, i.e., 2 μm or less, should be used near the dielectric surface to capture the correct discharge structure with a plasma sheath. In the present study, such fine grid is used to calculate the discharge development under different polarities. We first systematically compare the discharge evolution under positive electrode polarity (PEP) and negative electrode polarity (NEP). Subsequently, the transport of charged particles in the near-surface region is analyzed and compared to explain the distinct discharge development under different electrode polarities. Finally, the generated EHD body force and heat source are analyzed and compared between PEP and NEP.

4.2 Discharge evolutions under positive and negative voltage pulses

The dynamics of discharge evolution under PEP and NEP are quite different [89]. Generally speaking, the discharge process is characterized by the interaction between the transport of charged particles and the evolution of electric field. In this section, a systematic comparison between the discharge dynamics under PEP and NEP is conducted during the entire period of nanosecond pulse.

The computed conduction electrical currents in response to the applied voltage pulse are shown in Fig. 4.1. The conduction current was calculated as an integral

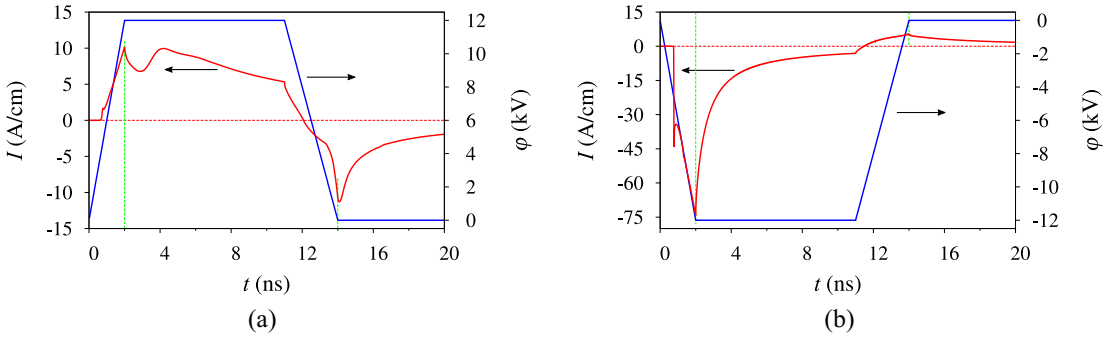

Figure 4.1: Applied voltage signal (blue line) and the electrical current (red line): (a) positive electrode polarity (PEP); (b) negative electrode polarity (NEP).

of fluxes of charges through the upper electrode [49], which is directly related to the transport of charged particles. At the leading edge of the applied voltage, with the increase of applied voltages, the currents increase rapidly for both PEP and NEP and reach their peak values at $t = 2$ ns. During the trailing edge of the applied voltage ($11 < t < 15$ ns), the currents decrease toward zero and change their signs. The maximum currents during the trailing edge of voltage are observed at about $t = 14$ ns. For both polarities, two discharge strokes are observed at the leading and trailing edges of voltage signals. For PEP, the current is positive during the first discharge stroke and negative during the second stroke. On the contrary, the current for NEP is negative during the first stroke and positive during the second stroke (although the amplitude is much smaller).

During the first discharge stroke, dynamics of the discharge are obviously different between PEP and NEP, as shown in Fig. 4.2. Generally speaking, the discharge structure under PEP shows a distinct streamer, while that under NEP is more diffuse, which is consistent with previous experimental observations [1] and numerical simulations [47, 49, 77]. The zoom-up view of the electron number density and the electric field strength are shown in Figs. 4.2(b-c). In order to show the near-surface discharge structure more clearly, the color range of the electron number density is

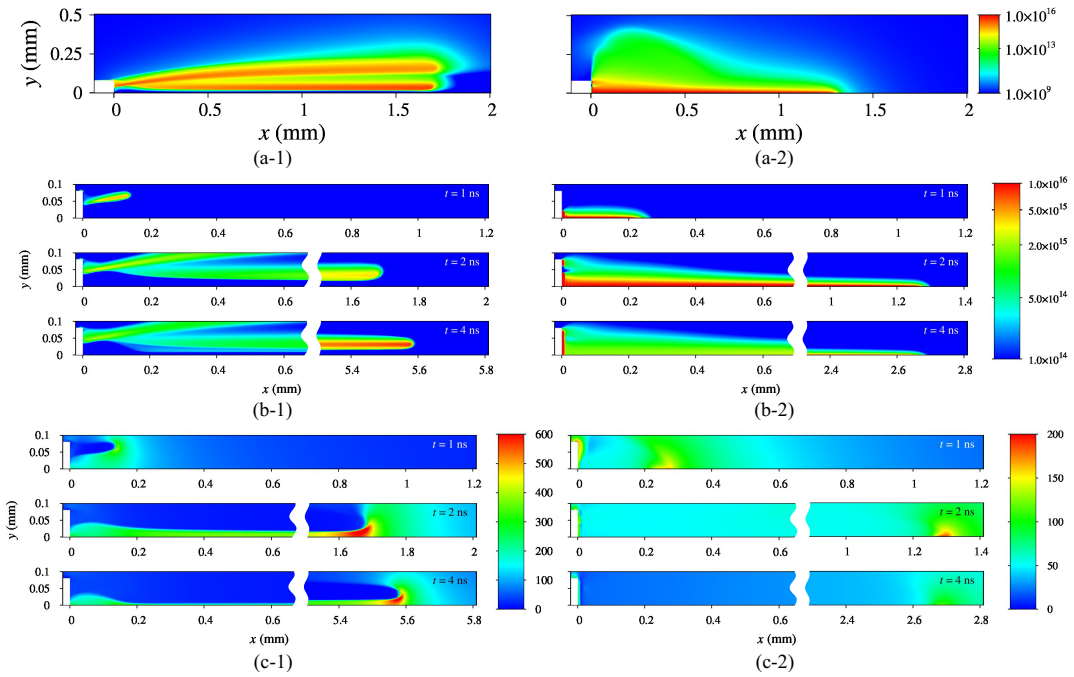

Figure 4.2: Near-surface discharge development during the first discharge stroke: (a) electron number density (cm^{-3}) at $t = 2$ ns; (b) zoom-up view of electron number density; (c) electric field strength (kV/cm). (a-1, b-1, c-1) positive electrode polarity (PEP); (a-2, b-2, c-2) negative electrode polarity (NEP).

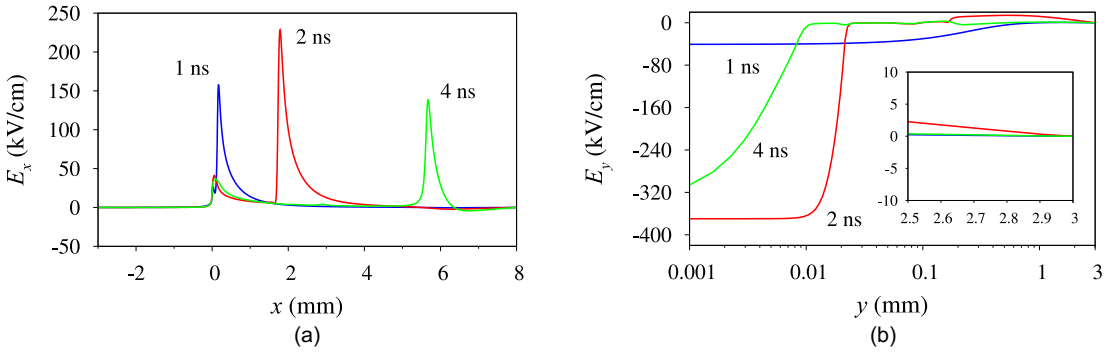

Figure 4.3: Distribution of electric field: (a) streamwise distribution of E_x at $y = 0.1$ mm; (b) wall-normal distribution of E_y at $x = 0.5$ mm.

set as 10^{14}–10^{16} cm^{-3}. For PEP, a streamer forms in the vicinity of upper electrode and rapidly propagates along the dielectric surface. A streamer branch appears at the initial stage of the discharge, as shown in Fig. 4.2(b-1). One potential reason for this streamer branching is the use of Neumann boundary condition for $\boldsymbol{\phi}$ at the outer boundary of the computational domain. The accurate formulation of boundary conditions for zero electric field at infinity remains as a key technical issue that needs to be resolved for adequate numerical simulations of SDBDs [89]. In the present simulation, the outer boundary of computational domain is far from infinity, but the high electric field region is concentrated only in the near-surface region. The distributions of the normal components of electric field (i.e., E_x at $y = 0.1$ mm, E_y at $x = 0.5$mm) are shown in Fig. 4.3. It is found that the normal component of electric field nearly vanishes already at 1 mm away from the outer boundary of the computational domain. Besides, we have increase the computational domain in both streamwise and wall-normal direction. It is found that the results obtained from enlarged computational domain is the same as the present results. It indicates that the present computational domain is enough to capture the discharge development correctly.

By conducting plenty of numerical tests, we have checked the influence of several

parameters on the computational results, including the size of computational domain, electron boundary condition at the dielectric surface and the initial density of charged particles. For the influence of computational domain, we increased the top computational boundary from $y_T = 3$ mm to $y_T = 10$ mm, while the right computational boundary from $x_R = 8$ mm to $x_R = 12$ mm, respectively. For the influence of electron boundary condition at the dielectric surface, we adopted the boundary condition described in Zhu et al. [49], i.e., a combination of zero gradient of flux for flow towards the boundary and zero flux for flow away from the boundary. For the influence of initial density of charged particles, we reduced the initial density of charged particles from $n_0 = 10^9$ cm^{-3} to $n_0 = 10^3$ cm^{-3}. Apart from the initial density of charge particles, other three parameters (i.e., the boundary condition, y_T, and x_R) have little influence on the electron number density field, as shown in Figs. 4.4(a-c). Namely, the streamer branching observed here is likely related to the initial condition of charged particles. Here, we try to give some explanations for this streamer branching by further examining the initial discharge development in the case of $n_0 = 10^9$ cm^{-3} and $n_0 = 10^3$ cm^{-3}, as shown in Fig. 4.4(a) and (d). For both cases, the streamer forms in the vicinity of the upper electrode, about 50 μm away from the dielectric surface, and then the streamer branch appears near the dielectric surface. From Fig. 4.2(c-1), it is shown that the electric field near the dielectric surface is very high, which enhances ionization. The charged particles generated by the ionization form the near-surface streamer branch. The difference between the two cases is observed in the parallel streamer above the near-surface streamer. The parallel streamer branch is obvious in the case of $n_0 = 10^9$ cm^{-3}, while it terminates at $x \simeq 0.25$ mm in the case of $n_0 = 10^3$ cm^{-3}. This indicates that the formation and propagation of the parallel streamer above the near-surface streamer is due to the relatively high background electron density assumed in the

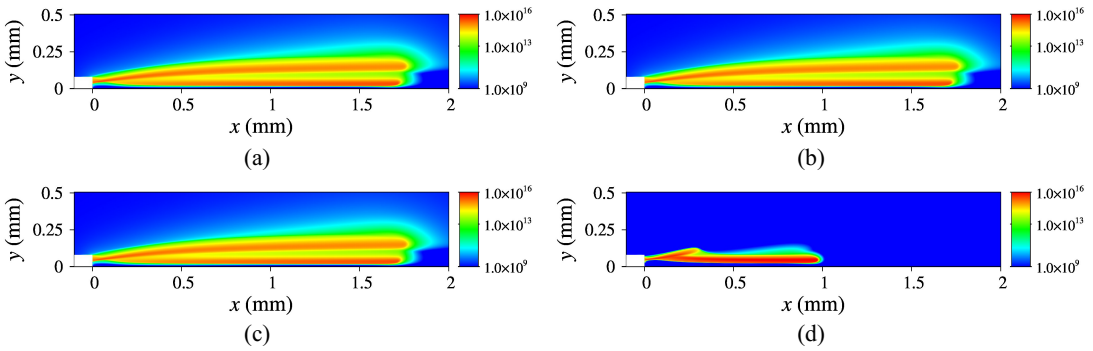

Figure 4.4: Electron number density (cm^{-3}): (a) $x_R = 8$ mm, $y_T = 10$ mm, during $0 < t < 2$ ns; (b) $x_R = 12$ mm, $y_T = 3$ mm, at $t = 2$ ns; (c) boudary condition at dielectric surface in Zhu et al. [49], at $t = 2$ ns; (d) $n_0 = 10^3$ cm^{-3}, during $0 < t < 2$ ns.

present simulation.

We have further analyzed the variation of electron density to explain the formation and propagation of the parallel streamer above the near-surface streamer. As described in Section 3.3, the variation of charged particle number density, n_i (i = p, n, e), depends on the drift-diffusion flux, ionization, attachment and recombination. Similarly, the contributions of streamwise flux, wall-normal flux, source and sink to the variation of electron number density are denoted as Φ_x, Φ_y, S and R for brevity. We have compared the electron density and its change rate in the case of $n_0 = 10^9$ cm^{-3} at $t = 1.2$ ns with that in the case of $n_0 = 10^3$ cm^{-3} at $t = 1.5$ ns, as shown in Fig. 4.5. A source region in the streamer head and a sink region in the streamer body are observed in both cases, as shown in Figs. 4.5(b-1) and (b-2). The spatial distributions (i.e., streamwise distribution at $y = 0.1$ mm and wall-normal distribution at $x = 0.2$ mm) of the contribution to the variation of electron number density are shown in Figs. 4.5(c) and (d). It is found that, in the region of parallel streamer head (see, Fig. 4.5(c)), the ionization contribution in the case of $n_0 = 10^9$ cm^{-3} is much higher than that in the case of $n_0 = 10^3$ cm^{-3}, which may result in the further propagation of the parallel streamer. In the streamer body,

the high recombination contribution will lead to the decrease of electron number density, as shown in Fig. 4.5(d). Despite the difference of streamer branching between the cases of different initial electron density, the formation and propagation of the near-surface streamer is similar and the sheath layer between the near-surface streamer and dielectric surface is observed in both cases. Namely, the initial electron density only influences the initial stage of the discharge, but not the discharge evolution, which is also in accordance with the results reported by Soloviev et al. [77] and Babaeva et al. [47].

In the streamer region, the densities of electrons and positive ions are of the order of 10^{14}–10^{15} cm^{-3}, which is significantly higher than that of negative ions (10^{13}–10^{14} cm^{-3}). Between the discharge streamer and dielectric surface, a region of low electron density exists, as known as plasma sheath [47, 49]. As shown in Fig. 4.2(c-1), the electric field near the head of the streamer is very high, leading to intense ionization and separation of positive ions and electrons. The electrons and negative ions drift toward the upper electrode, whereas the positive ions drift toward the dielectric surface to positively charge the dielectric surface. For NEP, a much thinner streamer forms, and it stays attached to the dielectric surface. Although it is reported "there is no streamers at negative polarity" in some papers [102], we will prefer to call the near-surface region of high charged particle density "negative streamers" under NEP, which is similar to [47, 49]. At the same time, a cathode layer characterized by high electron-density is observed in the vicinity of upper electrode. The electron-ion density in the streamer and cathode layer can reach the order of 10^{15}–10^{16} cm^{-3} at $t = 2$ ns. Due to NEP, positive ions drift to the upper electrode, resulting in the current peak at $t = 2$ ns; on the other hand, the electrons drift to the dielectric surface to negatively charge the dielectric surface.

Figure 4.6 depicts the wall-normal distribution of the wall-normal component

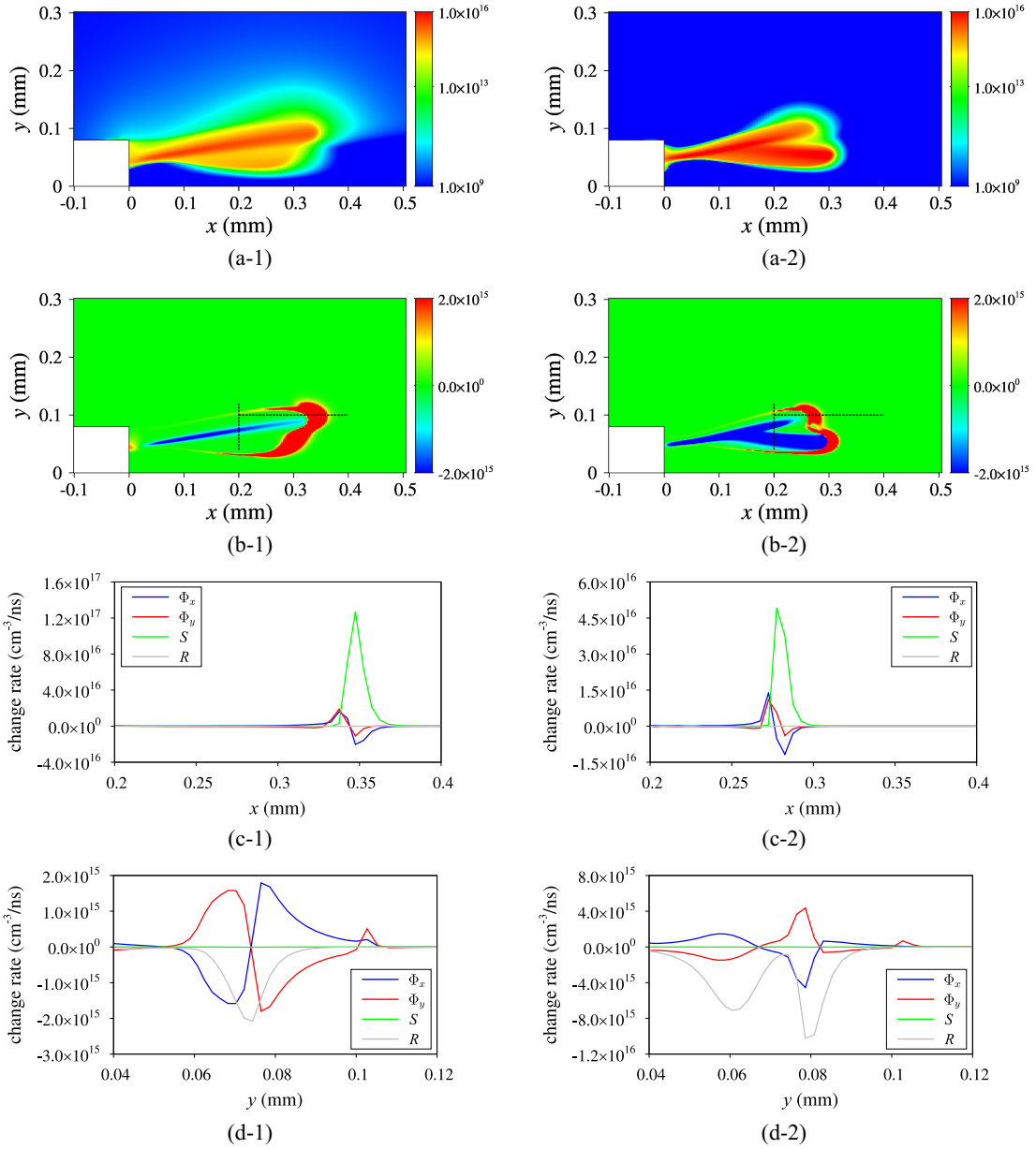

Figure 4.5: Influence of initial electron number density, n_0: (a) electron number density (cm^{-3}); (b) change rate of electron number density ($\mathrm{cm}^{-3}/\mathrm{ns}$); (c) streamewise distribution of the change rate of electron number density at $y = 0.1$ mm; (d) wall-normal distribution of the change rate of electron number density at $x = 0.2$ mm. (a-1, b-1, c-1, d-1) $n_0 = 10^9$ cm^{-3} at $t = 1.2$ ns; (a-2, b-2, c-2, d-2) $n_0 = 10^3$ cm^{-3} at $t = 1.5$ ns.

of electric field, E_y, and the charged particle number densities, n_p, n_e and n_n, at $x = 0.5$ mm. It is shown that a plasma sheath characterized by high electric field and low electron density exists under PEP. The sheath has a width of 10–20 μm during 2 ns to 4 ns. In contrast, plasma sheath is not observed for NEP during the first stroke. This is because the electric field near the dielectric surface is much weaker than that of PEP, while the electron density near the dielectric surface is much larger. Such a difference is a consequence of transport of charged particles, which will be discussed in more detail in Sec. 4.3.

In the previous numerical results [79], a thin high-electric-field layer above the dielectric surface is also observed under NEP during the first discharge stroke. The absence of a thin high-electric-field layer above the dielectric surface in the present study may be due to the use of Neumann boundary condition for electron at the dielectric surface. Hence, we performed additional computation to investigate the influence of boundary condition for electron at the dielectric surface on the computational results. In addition to the Neumann boundary condition, we adopted the boundary condition described by Zhu et al. [49]. Note that the original boundary condition of Zhu et al. [49] overestimates the ionization near the dielectric surface and leads to extremely high electron density, indicating that the nonlocality of the ionization source should be considered [77]. In order to avoid this problem, we modified the boundary condition by *artificially* setting the ionization rate coefficient in the first layer of computational cells above the dielectric surface to zero. Hereafter, the modified boundary condition from Zhe et al. [49] is denoted as BC-Modified. High electric field above the dielectric surface is observed by using BC-Modified, as shown in Fig. 4.6(a-3) and the charged particle number density above the dielectric surface is lower than that obtained by using the Neumann boundary condition,

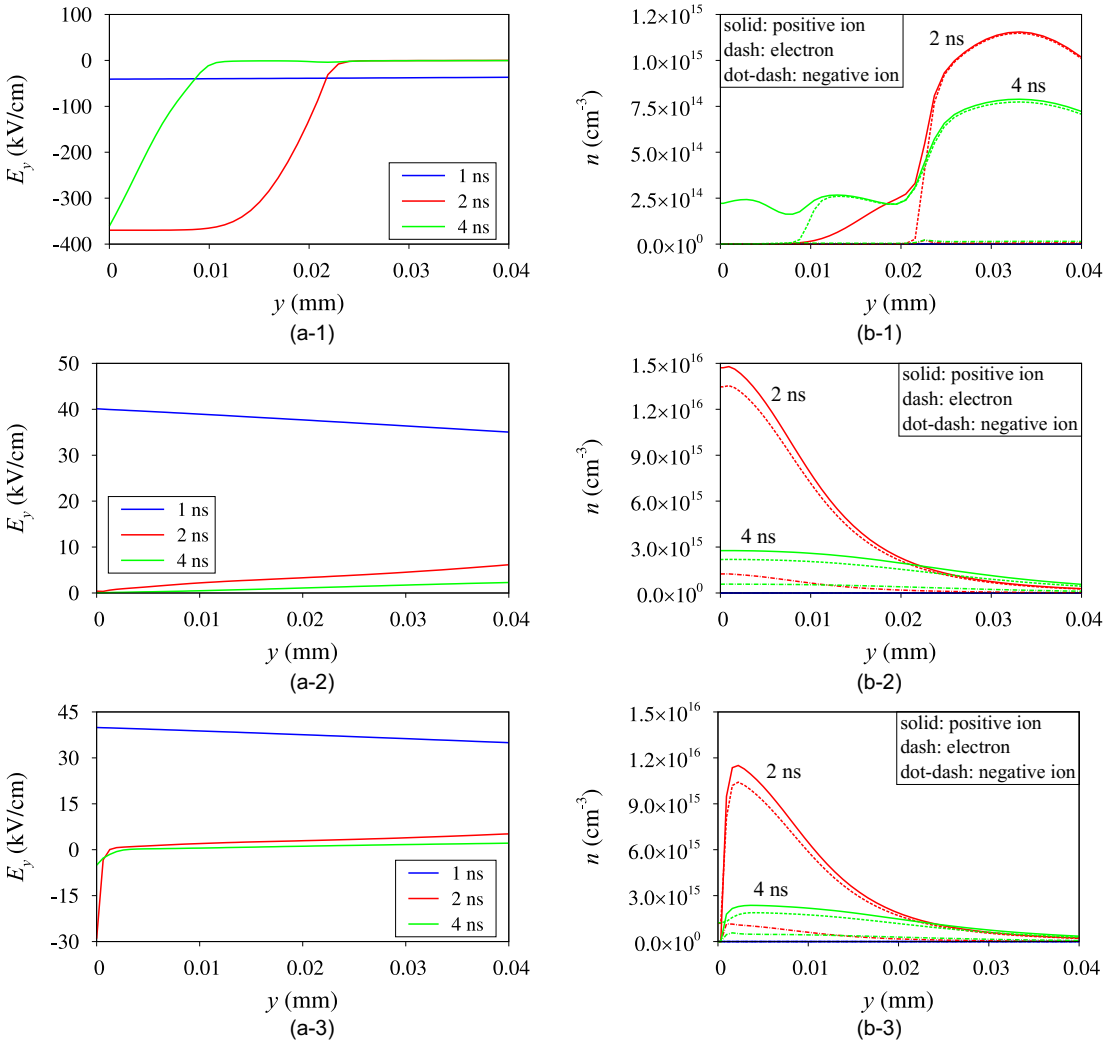

Figure 4.6: Wall-normal distribution of electric field and charged particle number density at $x = 0.5$ mm during the first discharge stroke: (a) electric field; (b) charged particle number density. (a-1, b-1) positive electrode polarity (PEP); (a-2, b-2) negative electrode polarity (NEP) with Neumann boundary conditon; (a-3, b-3) negative electrode polarity (NEP) with BC-Modified.

which is similar to that in Soloviev et al. [79]. In spite of the difference, the maximum density is of the same order of magnitude (10^{16} cm^{-3}) for Neumann boundary condition and BC-Modified, and the region of high electron density in the region of about $y < 20$ μm is observed in both cases. It indicates that even with the Neumann boundary condition, the discharge propagation during the nanosecond pulsed discharge process can be properly captured if the grid resolution is sufficiently fine. This validates the use of the Neumann boundary condition for simulation of the discharge propagation, although in order to predict the plasma interaction with the surface and to estimate the electric field near the surface more accurately, it is necessary to use an accurate boundary condition for electron flux at the dielectric surface. For instance, Hagelaar et al. [103] have proposed an accurate boundary condition by equating the hydrodynamic flux and the kinetic flux, i.e.,

$$\begin{aligned}\vec{\Gamma}_{\mathrm{e}} \cdot \vec{n} =& \frac{1-r_{\mathrm{e}}}{1+r_{\mathrm{e}}}\left[-(2a_{\mathrm{e}}-1)\mu_{\mathrm{e}} n_{\mathrm{e}} \vec{E}\cdot\vec{n} + \frac{1}{2} v_{\mathrm{th,e}} n_{\mathrm{e}} - \frac{1}{2} v_{\mathrm{th,e}}(1-a_{\mathrm{e}}) \frac{\gamma \vec{\Gamma}_{\mathrm{p}} \cdot \vec{n}}{\mu_{\mathrm{e}} \vec{E}\cdot\vec{n}}\right] \\ & - \frac{2}{1+r_{\mathrm{e}}}(1-a_{\mathrm{e}})\gamma \vec{\Gamma}_{\mathrm{p}} \cdot \vec{n},\end{aligned} \tag{4.1}$$

where $\vec{\Gamma}_{\mathrm{e}}$ and $\vec{\Gamma}_{\mathrm{p}}$ are the electron flux and positive ion flux at the dielectric surface; $\vec{n}$ is the normal vector pointing toward the dielectric surface; a_{e} is set to unity if the electron drift velocity is directed toward the dielectric surface and zero otherwise; r_{e} is the fraction of electrons reflected by the surface, and $v_{\mathrm{th,e}}$ is the electron thermal velocity. For more ditails, readers are refered to Hagelaar et al. [103] and Soloviev et al. [77].

Another significant difference in the discharge development between PEP and NEP is observed in the velocity of the streamer propagation, as shown in Fig. 4.7. Here, the head position of the streamer is defined as the position where E_y on the dielectric surface takes its maximum value. The initial development of the streamer

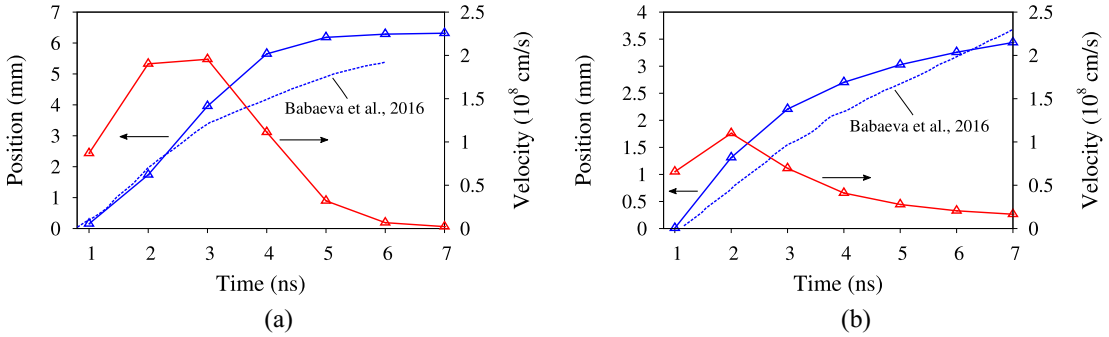

Figure 4.7: Head position (blue) and its propagation velocity (red) of discharge streamer: (a) positive electrode polarity (PEP); (b) negative electrode polarity (NEP).

head position under PEP is in good agreement with that in the previous study by Babaeva et al. [47], even though UV photoionization is not considered in the present study. On the other hand, as demonstrated in our previous paper [85], coarse grid resolution can lead to underestimation of the steamer propagation under PEP, which may also lead to the deviation of streamer head position after $t \simeq 2.5$ ns. The streamer velocity under NEP is obviously lower than that under PEP. For the same magnitude of the voltage pulse, i.e., $V_p = \pm 12$ kV, the streamer velocities reach 2×10^8 cm/s for PEP and 1×10^8 cm/s for NEP at $t = 2$ ns when the applied voltage reaches its amplitude value. Then, the streamer velocity decreases to 0.2×10^8 cm/s under NEP, and decrease to almost zero as the streamer reaches the edge of the lower electrode under PEP.

The distributions of the surface charge density during the first discharge stroke are shown in Fig. 4.8. Due to the different electrode polarity, the transport directions of ions and electrons under NEP are contrary to those under PEP; namely, positive ions drift toward the dielectric surface under PEP, while electrons and negative ions drift toward the dielectric surface under NEP. Because of the higher mobility of electrons, the dielectric surface is instantly negative-charged under NEP. The surface charge density near the upper electrode is around 400 nC/cm^2 at

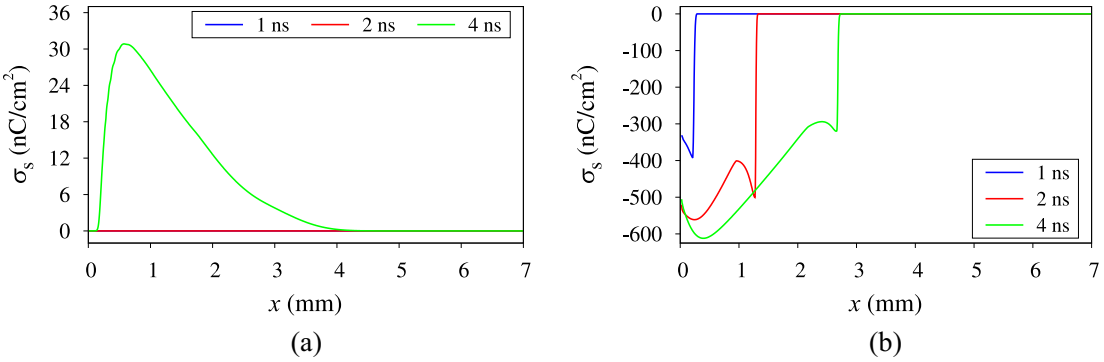

Figure 4.8: Distribution of surface charge density during the first discharge stroke: (a) positive electrode polarity (PEP); (b) negative electrode polarity (NEP).

$t = 1$ ns and reaches 600 nC/cm^2 at $t = 4$ ns. Note that the surface charge density computed in the present study is also in fair accordance with the simulation results of Soloviev et al. [79], i.e., 110 nC/cm^2, taking into account the difference in the dielectric permittivity assumed. The surface charge shields the wall-normal component of the external electric field, E_y, and prevents the streamer from further developing along the dielectric surface. For PEP, the dielectric surface is positively charged due to positive ions. Because the mobility of ions is much lower than that of electrons, the increase of surface charge is much slower and its value is much smaller than that under NEP.

Another reason for the difference in the dynamics of surface charge is the difference in the near-surface discharge structures. As shown in Fig. 4.6, the ion and electron densities under PEP are much lower in the plasma sheath region; but under NEP, the streamer is attached to the dielectric surface and the electron density in the streamer is kept high. As the result, the surface charge density under NEP is also much higher than that under PEP.

The spatial distributions of electric field on the surface during the first discharge stroke are shown in Fig. 4.9. The peak of electric field indicates the position of streamer head, which is consistent with the electric field strength shown in

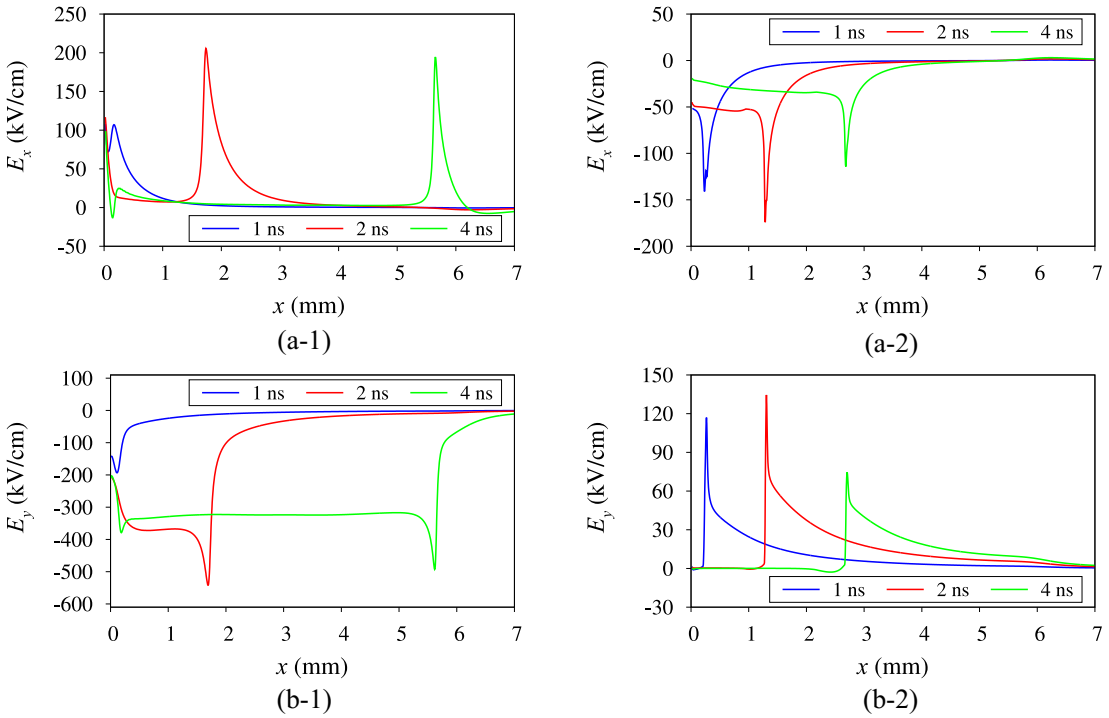

Figure 4.9: Distribution of electric field on the dielectric surface during the first discharge stroke: (a) streamwise component, E_x; (b) wall-normal component, E_y. (a-1, b-1) positive electrode polarity (PEP); (a-2, b-2) negative electrode polarity (NEP).

Figs. 4.2(c-1) and (c-2). The magnitude of E_x on the surface is comparable for both PEP and NEP, which is about 100–200 kV/cm. However, because of the shielding effect explained above, E_y under NEP is much weaker than that under PEP.

During the second discharge stroke, too, the near-surface discharge structures are different between PEP and NEP. Compared with the first discharge stroke, the electron-ion density in the streamer decreases to the order of 10^{14} cm^{-3}. For PEP, the discharge streamer gradually attaches to the dielectric surface and a cathode layer forms in the vicinity of the upper electrode, as shown in Fig. 4.10(b-1). The ion current from the cathode layer to the upper electrode leads to the second peak of the current, as shown in Fig. 4.1(a). For NEP, the discharge streamer gradually detaches from the dielectric surface and plasma sheath forms between the streamer and dielectric surface, as shown in Figs. 4.10(b-2) and (c-2). Figure 4.11 depicts the wall-normal distribution of E_y, n_p, n_e and n_n at $x = 0.5$ mm during the second discharge stroke. It is shown that, under PEP, n_e increase in the near-surface region (about $y < 15$ μm), while E_y decreases. Under NEP, a plasma sheath with low electron density forms between the discharge streamer and dielectric surface. From the wall-normal distributions of charged particles at $x = 0.5$ mm (i.e., Fig. 4.11(b-2)), it is shown that the thickness of the region of low electron density varies from 3 μm to 15 μm between 14 ns and 18 ns. The computational discharge propagation by using BC-Modified is also depicted in Figs. 4.11(a-3) and (b-3), which is similar to that by using the Neumann boundary condition. Plasma sheath is observed during the second discharge stroke and the maximum electron number density is of the same order of magnitude (10^{14} cm^{-3}) as that by using the Neumann boundary condition.

The distributions of the surface charge density during the second discharge stroke are shown in Fig. 4.12. The surface charges act as a virtual cathode for NEP

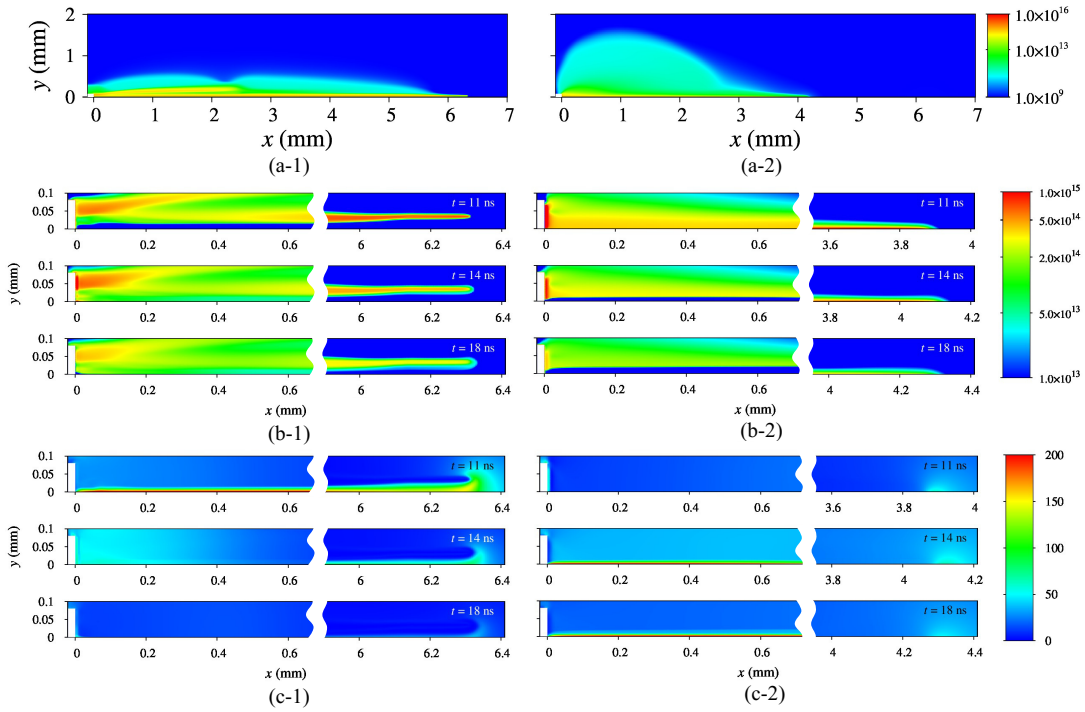

Figure 4.10: Near-surface discharge development during the second discharge stroke: (a) electron number density (cm^{-3}) at $t = 14$ ns; (b) zoom-up view of electron number density; (c) electric field strength (kV/cm). (a-1, b-1, c-1) positive electrode polarity (PEP); (a-2, b-2, c-2) negative electrode polarity (NEP).

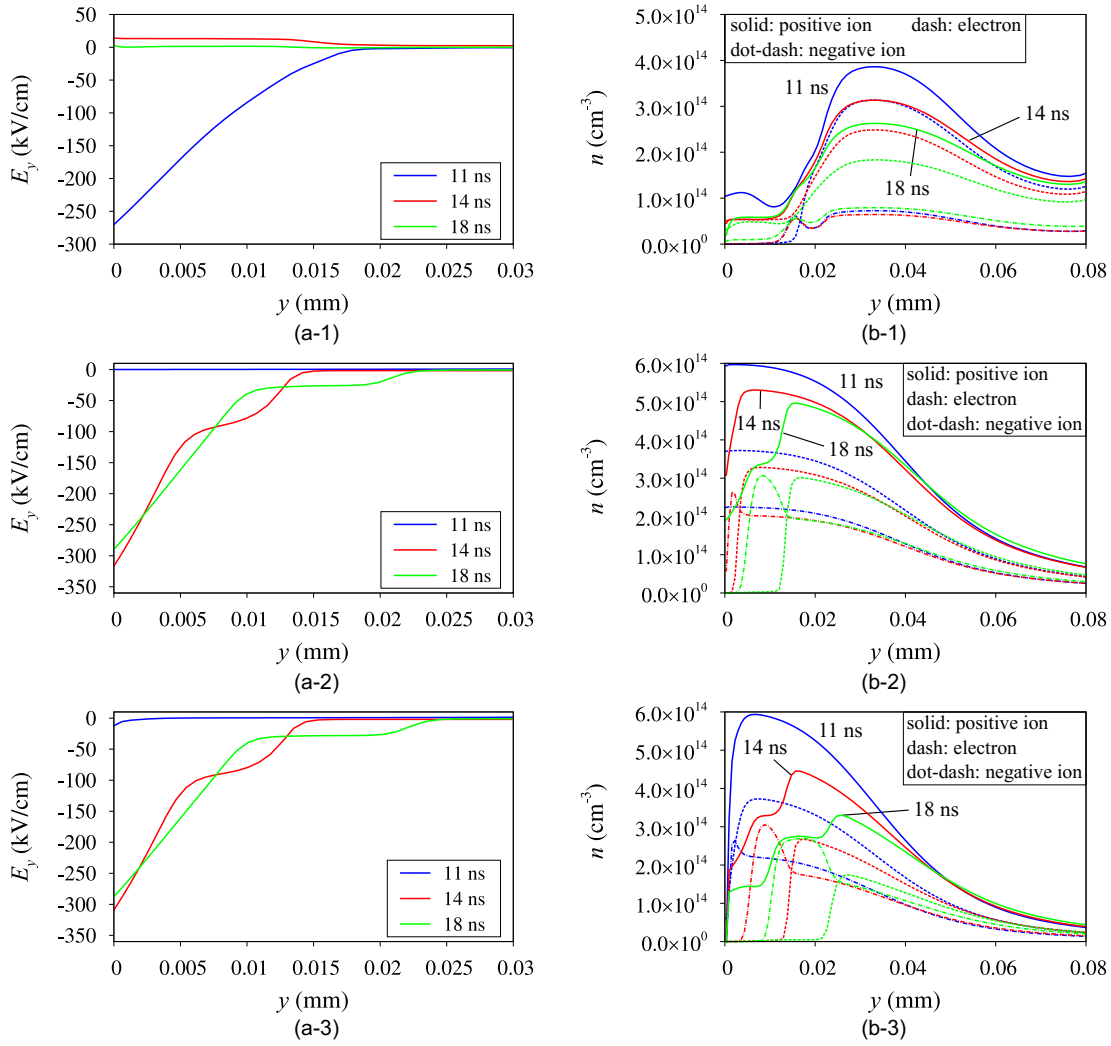

Figure 4.11: Wall-normal distributions of electric field and charged particle number density at $x = 0.5$ mm during the second discharge stroke: (a) electric field; (b) charged particle number density. (a-1, b-1) positive electrode polarity (PEP); (a-2, b-2) negative electrode polarity (NEP) with Nuemann boudary condition (a-3, b-3) negative electrode polarity (NEP) with BC-Modified.

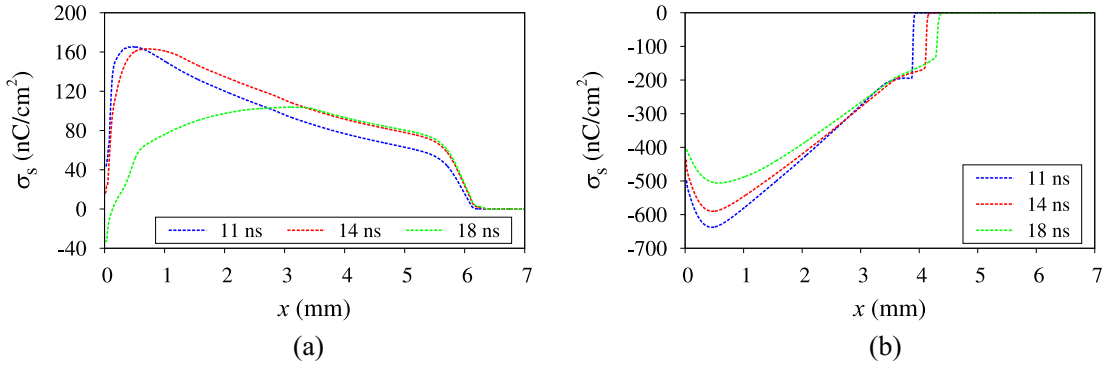

Figure 4.12: Distribution of surface charge density during the second discharge stroke: (a) positive electrode polarity (PEP); (b) negative electrode polarity (NEP).

and an anode for PEP. After the applied voltage starts to decrease at $t = 11$ ns, the virtual cathode or anode gradually governs the discharge process. During the trailing edge of the applied voltage (i.e., $11 < t < 14$ ns), both E_x and E_y change their signs, as shown in Fig. 4.13, indicating that the direction of the electric field vector reverses. Accordingly, the directions of charged particle transport also change. For PEP, negative ions and electrons start to drift toward the dielectric surface, and for NEP, positive ions start to drift toward the dielectric surface, which results in the decrease in the surface charge density.

4.3 Electron transport and its relation to near-surface discharge structure

From Sec. 4.2, it has been shown that the near-surface discharge structures under PEP and NEP are significantly different during the entire discharge process. For PEP, a plasma sheath forms and propagates during the first stroke, and the streamer attaches to the dielectric surface during the second stroke. For NEP, a streamer is attached to the dielectric surface during the first stroke of discharge, and a plasma sheath forms during the second stroke. In order to understand the

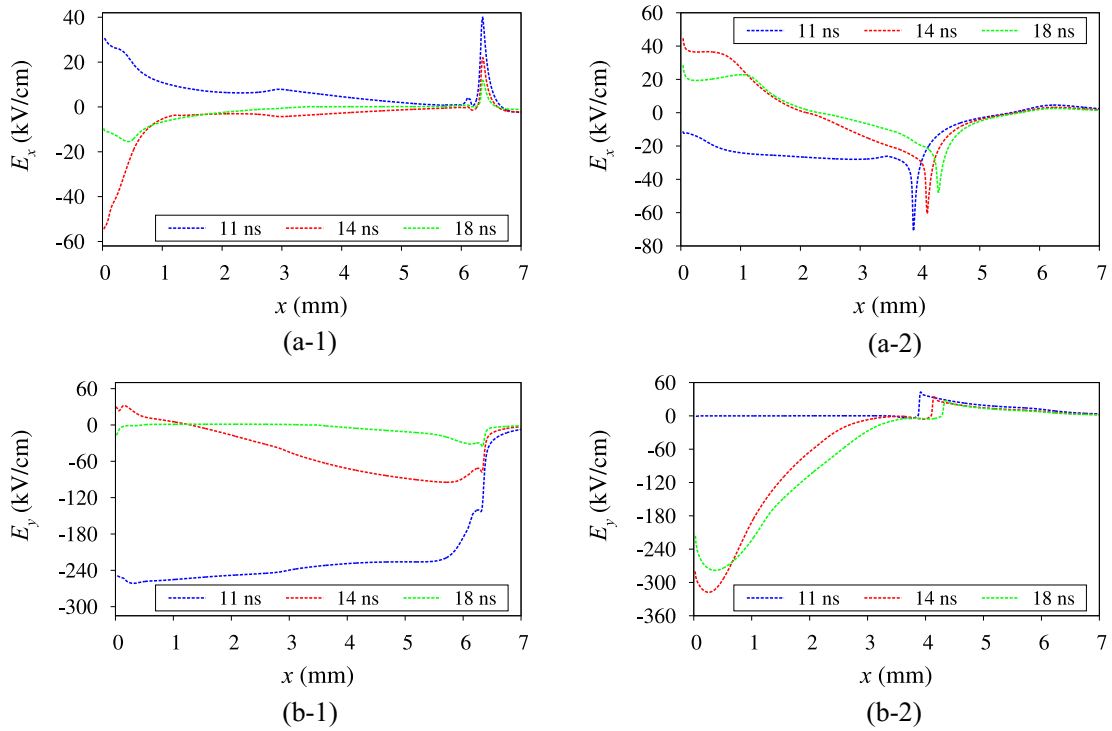

Figure 4.13: Distribution of electric field on the dielectric surface during the second discharge stroke: (a) streamwise component, E_x; (b) wall-normal component, E_y. (a-1, b-1) positive electrode polarity (PEP); (a-2, b-2) negative electrode polarity (NEP).

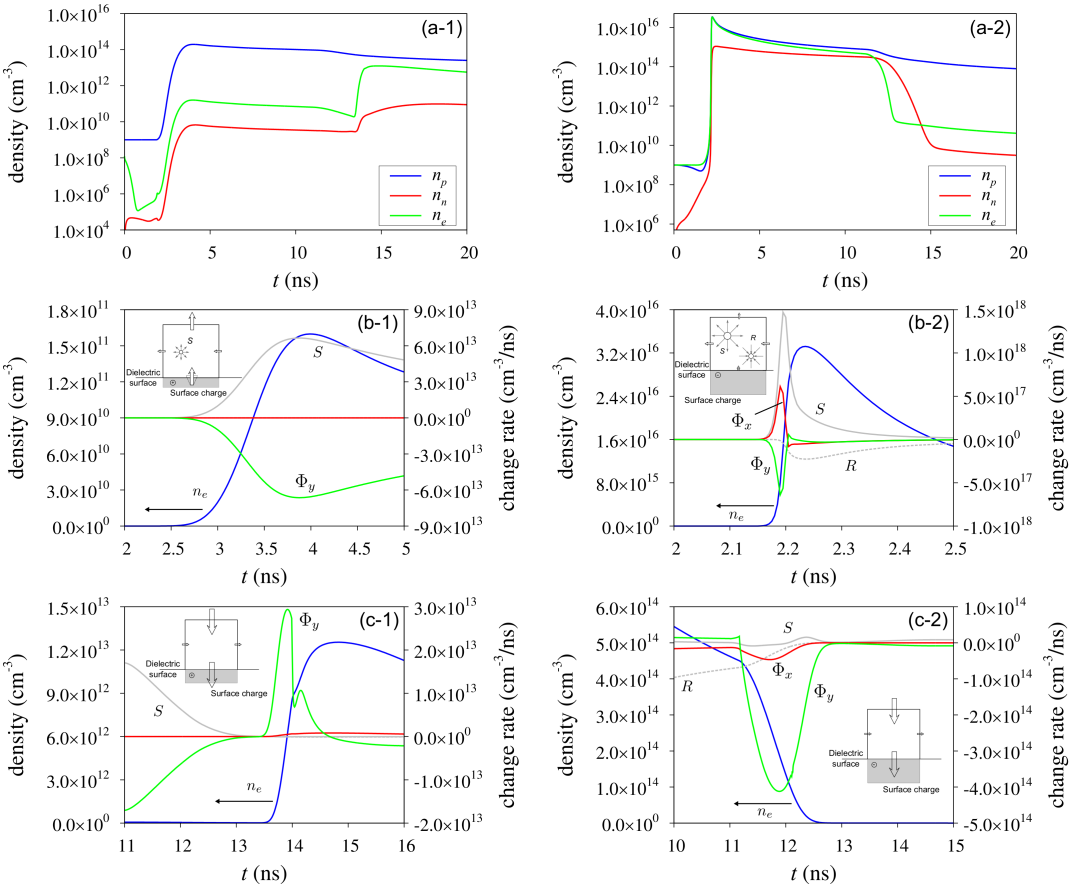

Figure 4.14: Transport of charged particles near the dielectric surface: (a) time trace of charged particles number density; (b) illustration of the electron transport during the first discharge stroke; (c) illustration of the electron transport during the second discharge stroke. (a-1, b-1, c-1) positive electrode polarity; (a-2, b-2, c-2) negative electrode polarity.

mechanism for this difference, transports of charged particles are analyzed and compared for different electrode polarities.

The transport of charged particles near the dielectric surface is distinct between PEP and NEP. Hence, we choose the first computational cell adjacent to the dielectric surface at $x = 0.5$ mm to analyze the transport of charged particles. The time traces of the charged particles number densities, n_{i} (i = p, n, e), are shown in Fig. 4.14. For both PEP and NEP, two remarkable variations are observed during 2–5 ns and 11–15 ns, corresponding to the two discharge strokes. During the first

stroke, n_{i} increase rapidly, and the increase under NEP is more significant than that under PEP. Before the second stroke, n_{p} is much larger than n_{e} and n_{n} under PEP, while n_{p} and n_{e} are comparable but larger than n_{n} under NEP. During the second stoke, n_{e} increases substantially under PEP, while n_{e} and n_{n} decrease significantly under NEP.

The significant difference in the time variation of n_{e} between PEP and NEP indicates different electron transport mechanisms. The transport of electrons during the two discharge strokes are demonstrated in Figs. 4.14(b-c). From Eq. (3.1c), the variation of n_{e} consists of contributions from drift-diffusion flux, source, and sink. The contribution of drift-diffusion flux, $\nabla \cdot \vec{\Gamma}_{\mathrm{i}}$, can be decomposed into the contribution of streamwise flux, $\partial \Gamma_{\mathrm{i}x}/\partial x$, and the wall-normal flux $\partial \Gamma_{\mathrm{i}y}/\partial y$. Hereafter, the contribution of streamwise flux, wall-normal flux, source and sink are denoted as $\Phi_x = \partial \Gamma_x/\partial x$, $\Phi_y = \partial \Gamma_y/\partial y$, S and R for brevity.

During the first discharge stoke under PEP, the variation of n_{e} is determined by Φ_y and S (due to ionization), while Φ_x and R are negligible. The schematic illustration of electron transport in the control volume is depicted in Fig. 4.14(b-1). At the dielectric surface, secondary electron emission takes place due to ion flux to the dielectric surface, whereby the dielectric surface is positively charged. At the same time, electrons drift away from the near-surface region. The overall effect of Φ_y is to oppose the increase of n_{e} and the electrons generated by ionization are instantly compensated by the wall-normal flux. Although the electric field near the dielectric surface is much higher than the ionization threshold (i.e., 32.28 kV/cm) [77], discharge avalanche does not happen during the first discharge stroke of PEP due to insufficient amount of electrons. For NEP, the variation of n_{e} is determined by all the four terms, among them ionization is dominant. As illustrated in Fig. 4.14(b-2), electrons drift toward the dielectric surface to negatively charge

it. In streamer-wise (x) direction, electrons drift from left to right. The overall effect of Φ_x is to increase n_e, and that of Φ_y is to compensate the increase in n_e. As Φ_x and Φ_y are balanced by each other, electrons generated by ionization are no longer compensated by the drift-diffusion flux. Hence, once the electric field reach the ionization threshold, ionization avalanche takes place, resulting in dramatic increase of electron density. The duration of the ionization avalanche is within 0.1 ns and the electron density decreases quickly due to the recombination with positive ions.

During the second discharge stroke, the variation of n_e under PEP is mainly determined by Φ_y. At the trailing edge of the applied voltage pulse, the surface charge acting as a virtual anode starts to dominate the electric field. Wall-normal component of electric field, E_y, changes its sign and the electrons start to drift toward the dielectric surface, leading to the rapid increase of n_e near the dielectric surface, as illustrated in Fig. 4.14(c-1). For NEP, too, the variation of n_e is mainly determined by Φ_y. In contrast to PEP, however, the dielectric surface acts as a virtual cathode and electrons start to drift away from the dielectric surface to the top side, leading to the rapid decrease of electron density near the dielectric surface, as illustrated in Fig. 4.14(c-2). This electron transport mechanism can also explain the formation of plasma sheath during the second discharge stroke of NEP.

4.4 Body force and heat source

The generated EHD body force and heat source are compared between PEP and NEP. The domain-integrated streamwise EHD body force, F_x, and heat source, W, are defined as

$$F_x = \iint c(n_\mathrm{p} - n_\mathrm{n} - n_\mathrm{e}) E_x dx dy, \tag{4.2}$$

and

$$W = \iint c(\vec{\Gamma}_{\mathrm{p}} - \vec{\Gamma}_{\mathrm{n}} - \vec{\Gamma}_{\mathrm{e}}) \cdot \vec{E} dxdy. \tag{4.3}$$

This value should be treated as a maximal possible value of heat source, because only a part of this power transfer to heat [77]. The energy transfer from plasma to gas heating is a complicated question, as has been discussed in previous studies [35, 65, 84, 104, 105]. Note that the present results just focus on the difference of this maximal possible value of heat source between PEP and NEP, and the detailed kinetic mechanisms of the heating process is beyond the scope of this paper.

As shown in Fig. 4.15, F_x is mainly generated during the first discharge stroke under PEP, while during the second discharge stroke under NEP. For PEP, a plasma sheath forms and propagates during the first discharge stroke. In the plasma sheath, the density of positive ions is much higher than that of negative ions and electrons (as shown in Fig. 4.6(b-1)), and a large amount of positive net charges exist, which contributes to the generation of EHD body force. However, during the second discharge stroke, the plasma sheath fades away and the near-surface region becomes quasi-neutral, leading to the decrease of body force. On the contrary, for NEP, plasma sheath forms in the near-surface region during the second discharge stroke. The density of charged particles in the near-surface region are shown in Fig. 4.11(b-2). At $t = 14$ ns, the density of electrons close to the dielectric surface (about $y < 3$ μm) is much lower than that of positive ions and electrons. Besides, the density of positive ions is higher than that of negative ions, and a large amount of positive net charges exist. Similar situation is observed at $t = 18$ ns. Hence, during the second discharge stroke of NEP, it is mainly positive ions and negative ions that contribute to the generation of EHD body force.

The time trace of the domain-integrated heat source, W, is shown in Fig. 4.16. Due to the high peak of current during the first discharge stroke, the heat source

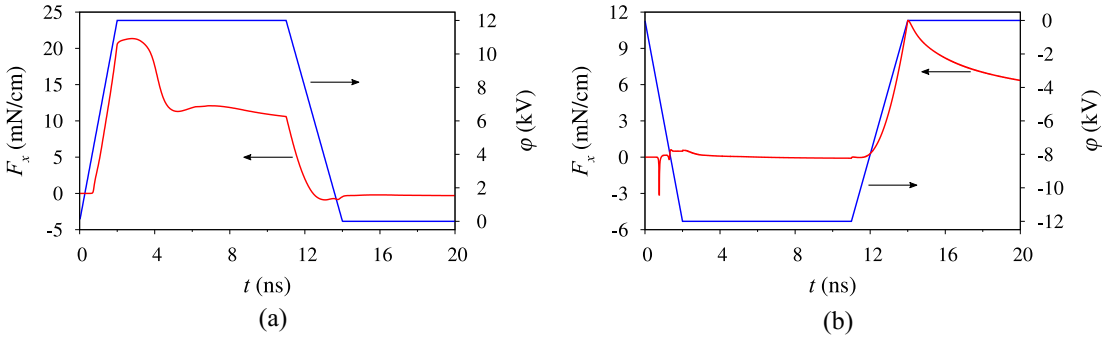

Figure 4.15: Time trace of EHD body force: (a) positive electrode polarity (PEP); (b) negative electrode polarity (NEP).

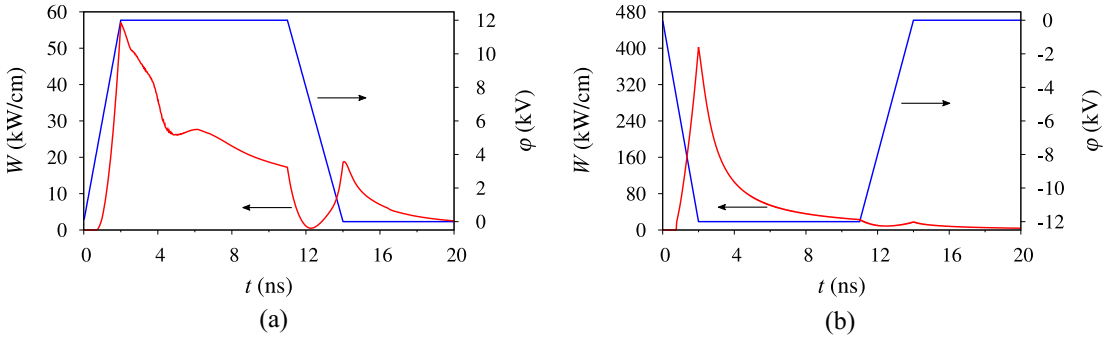

Figure 4.16: Time trace of heat source: (a) positive electrode polarity (PEP): (b) negative electrode polarity (NEP).

is very high and reaches its maximum value at $t = 2$ ns for both PEP and NEP. During the second discharge stroke, the heat source under PEP has a second peak, while the heat source under NEP is much smaller. The total heating energy during 20 ns is 0.34 mJ/cm for PEP and 1 mJ/cm for NEP.

These results suggest that, as far as the present configuration is concerned, PEP is more effective in force generation and NEP is more effective in heat generation. Which actuation mode (PEP or NEP) one should use, however, should be determined by which flow control mechanism (force or heat) one intends to use.

4.5 Conclusions

Two-dimensional numerical simulation of the NSDBD has been conducted for both PEP and NEP. The near-surface discharge structures have been analyzed and compared for both electrode polarities during the entire period of the nanosecond pulse. Transport of charged particles has been investigated to explain the difference of discharge structure between PEP and NEP. Besides, the generated EHD body force and heat source during the voltage pulse have been compared.

Two discharge strokes occur for both PEP and NEP. The first discharge stroke occurs at the leading edge of the applied voltage pulse, while the second discharge stroke occurs at the trailing edge. During the first discharge stroke, discharge streamer forms in the vicinity of the upper electrode. The electron-ion density in the streamer is high, which is of the order of 10^{14}–10^{15} cm^{-3} for PEP and 10^{15}–10^{16} cm^{-3} for NEP. For PEP, around 20 μm-thick plasma sheath layer, characterized by low electron density and high electric field, forms between the streamer and dielectric surface. The discharge streamer could be successfully simulated using artificial conditions for background electron density without accounting for the photoionization process, but one have to be careful regarding the value of the background electron density: too high values may lead to unphysical solutions. For NEP, the streamer is attached to the dielectric surface and plasma sheath layer is not observed when the Neumann boundary condition for the electron number density at the dielectric surface is used. The simplified boundary condition for electron flux at the dielectric surface dramatically changes the discharge structure near the surface but does not notably influence the overall discharge behavior. For the present $V_p = \pm 12$ kV nanosecond pulse, the maximum propagation velocity of the discharge streamer is 2×10^8 cm/s for PEP and 1×10^8 cm/s for NEP.

During the second discharge stroke, for PEP, the plasma sheath layer decays and

the electron density near the dielectric surface increases along with the decrease of the electric field in the sheath layer. For NEP, a plasma sheath layer forms near the dielectric surface with the detachment of the streamer from the dielectric surface, which is similar to the sheath layer of PEP during the first discharge stroke.

The analysis of the electron transport near the dielectric surface reveals the absence of ionization avalanche in the sheath layer for PEP. In spite of the high electric field in the sheath layer, the electrons generated by ionization are instantly compensated by the wall-normal drift-diffusion flux and the electron density in the sheath layer is maintained at a low level. For NEP, ionization avalanche occurs near the dielectric surface during the first discharge stroke, resulting in instant increase of electron density in 0.1 ns, followed by strong recombination, which terminates the ionization avalanche and reduce the electron density to the order of 10^{14}–10^{15} cm^{-3}. The transport of electron during the second discharge stroke is determined by the wall-normal drift-diffusion flux for both PEP and NEP. The existence of surface charge changes the direction of electric field vector as well as the drifting direction of electrons. For NEP, electrons drift away from the near-surface region and a plasma sheath layer forms with the detachment of negative streamer from the dielectric surface.

The EHD body force for PEP is generated before the second discharge stroke due to the high net charge density and strong electric field in the near-surface sheath layer. For NEP, body force is generated during the second discharge stroke after the formation of near-surface sheath layer. The total heating energy per pulse is 0.34 mJ/cm for PEP and 1 mJ/cm for NEP.

The present systematic study in the thesis reveals the difference of discharge evolution of NSDBD under different electrode polarities. The electron transport near the dielectric surface play an important role in the discharge evolution, as well

as the generation of body force and heat source.

Chapter 5

Parametric study on NSDBD of different electrode polarities

5.1 Introduction

Considerable attentions have been paid to the use of SDBD-PAs for flow control and combustion ignition. The interaction between the discharge plasmas and airflow has been widely investigated [2, 4, 5, 89]. It is widely accepted that the EHD body force and fast gas heating are the main mechanisms of discharge interaction with the airflow. Plenty of work have been conducted to improve the EHD body force and heat source for operation of SDBD-PAs in high Reynold number regimes. Thomas et al. [20] conducted the optimization of the SDBD plasma actuator by examining the effects of dielectric material and thickness, voltage amplitude and frequency, voltage waveform, exposed electrode geometry, and the number of actuators experimentally. It is found that larger body force is gained by using dielectric barrier materials with high dielectric strength, low dielectric constant, and increased thickness. Unfortunately, the experimental observations are not enough to explain the reason for the effects of dielectric permittivity, dielectric thickness.

Table 5.1: Test cases for study on influence of applied voltage amplitude for positive polarity.

Case	V_p [kV]	ε_d	d [mm]
PV-1	8	16	0.5
PV-2	12	16	0.5
PV-3	16	16	0.5

In this chapter, we numerically investigate the effect of applied voltage amplitude, dielectric permittivity and dielectric thickness on the discharge propagation, induced EHD body force and heat source under positive and negative electrode polarity. Besides, we explain the reason for the effect by analyzing the the results in detail.

5.2 Parametric study on NSDBD of positive polarity

In this section, the influences of several parameters, including applied voltage amplitude V_p, dielectric permittivity ε_d, dielectric thickness d, on the discharge evolution, generated EHD body force and heat source of NSDBD of positive polarity are examined.

5.2.1 Influence of applied voltage amplitude

Three cases with three different voltage amplitudes are computed, and the dielectric permittivity is fixed as $\varepsilon_d = 16$; the dielectric thickness is fixed as $d = 0.5$ mm, as shown in Table 5.1.

The discharge currents under different voltage amplitudes are shown in Fig. 5.1. For each voltage amplitude, the currents increase with the voltage during the leading edge of the applied voltage, and reach the positive peak when the voltage

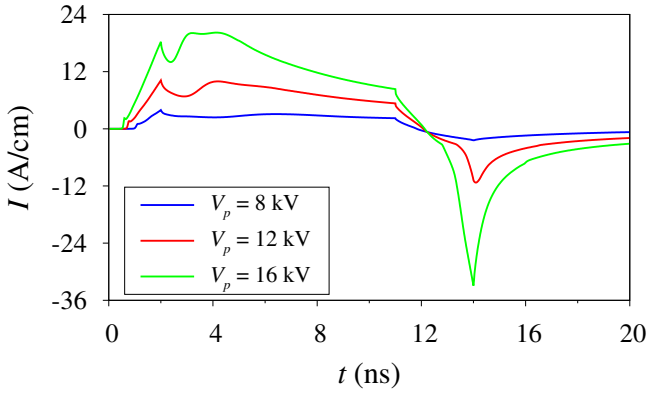

Figure 5.1: Discharge current under different voltage amplitudes for positive polarity.

reaches its amplitude value (i.e., $t = 2$ ns). During the trailing edge of the voltage, the currents decrease to zero and change its sign until reaching the negative peak at about the time when the voltage becomes zero (i.e., $t = 14$ ns). Besides, the currents increase with the voltage amplitude obviously. The positive peak currents at $t = 2$ ns are 3.94, 10.2 and 18.3 A/cm when $V_p = 8$, 12 and 16 kV, while the negative peak currents at about $t = 14$ ns are -2.42, -11.3 and -32.9 A/cm.

The streamer propagations under different voltage amplitudes are shown in Fig. 5.2. During the first 2 ns, the streamer propagates apparently faster with the increase of voltage amplitude. The propagation velocities of the streamer at $t = 2$ ns under $V_p = 8$, 12, 16 kV are 0.91, 1.90, 1.71×10^8 cm/s. Under $V_p = 16$ kV, the streamer quickly propagates to the right edge of the encapsulated electrode (i.e., $x = 6$ mm) at about $t = 3$ ns, leading to the instant decrease of the streamer propagation velocity, as shown in Fig. 5.2. Similar situation is observed at about $t = 5$ ns under $V_p = 12$ kV. The streamer propagates much slower under $V_p = 8$ kV. During $2 < t < 6$ ns, the streamer propagates smoothly with the velocity of 1×10^8 cm/s.

The time traces of the streamwise component of domain-integrated EHD body force under different voltage amplitudes are shown in Fig. 5.3. For each voltage

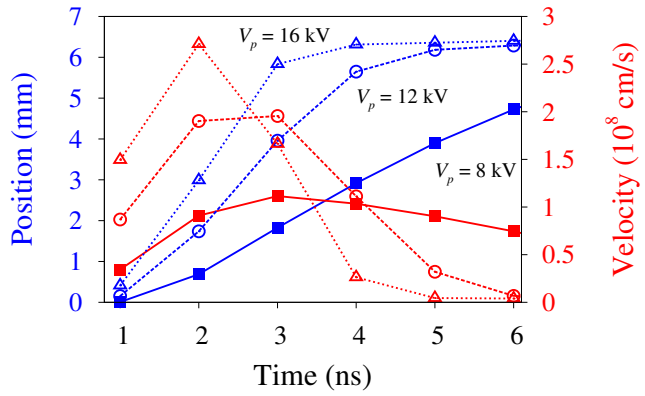

Figure 5.2: Streamer propagation under different voltage amplitudes for positive polarity.

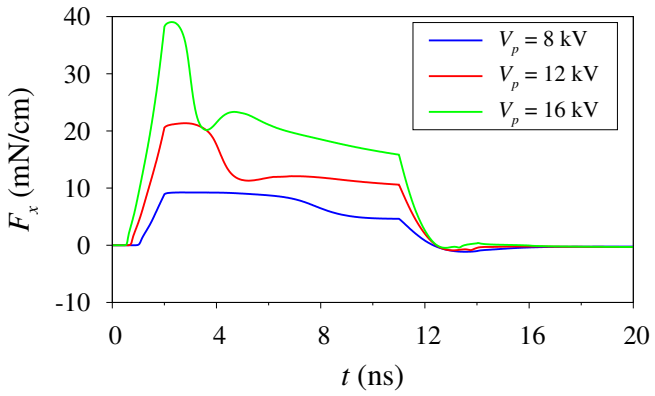

Figure 5.3: Time trace of streamewise domain-integrated EHD body force under different voltage amplitudes for positive polarity.

amplitude, the EHD body force F_x increase rapidly after the voltage reach the threshold. When the voltage reach its amplitude value (about $t = 2$ ns), a plateau is seen and the interval of the plateau decreases with voltage amplitude. In the case of $V_p = 12$ kV and 14 kV, it is clearly shown that F_x decrease after the plateau and another plateau is is observed. During the trailing edge of the voltage (i.e., $11 < t < 14$ ns), F_x decreases to zero gradually. The maximum values of F_x for each voltage amplitude during the voltage pulse are 9.24, 21.3 and 39.0 mN/cm, respectively.

The EHD body force fields under $V_p = 12$, 16 kV and the difference between

them at $t = 3$ ns are shown in Fig. 5.4(a). The force is concentrated in the sheath region, and the difference in force field is mainly the consequence of plasma sheath. The streamwise component of EHD body force F_x in the cross-section $x = 0.5$ mm is depicted in Fig. 5.4(b). It is clearly shown that F_x under $V_p = 16$ kV is much large than that under lower voltage amplitude. According to Eq. (4.2), the EHD body force is determined by the electric field and net charge number density. The streamwise component of electric field E_x and the net charge number density n_{net} in the cross-section $x = 0.5$ mm are shown in Figs. 5.4(c-d). The distribution of E_x is flat, and the distribution of F_x resembles that of the net charge density. Both E_x and n_{net} near the dielectric surface becomes larger under higher voltage amplitude, which results in stronger EHD body force. Hence, both E_x and n_{net} are responsible for the difference of F_x under different voltage amplitudes.

The time traces of the domain-integrated heat source under different voltage amplitudes are shown in Fig. 5.5. During the leading edge of the voltage, the heat sources increase and a peak appears at $t = 2$ ns. During the trailing edge of the voltage, another peak appears at $t = 14$ ns. Compared with the peak at $t = 2$ ns, the peak at $t = 14$ ns is smaller. Under high voltage (i.e., $V_p = 16$ kV), another peak at about $t = 4$ ns followed by the first peak is observed when the voltage is constant. The total maximal potential heating energies during 20 ns under $V_p = 8$, 12, 16 kV are 0.0904, 0.341, 0.863 mJ/cm, respectively.

5.2.2 Influence of dielectric permittivity

Thomas et al. [20] reported that a lower dielectric permittivity reduces the effective capacitance of the actuator and thereby also reduces the local concentration of electric field lines, which has the equivalent effect of lowering the current density and allowing operation of the actuator at higher voltage without giving rise

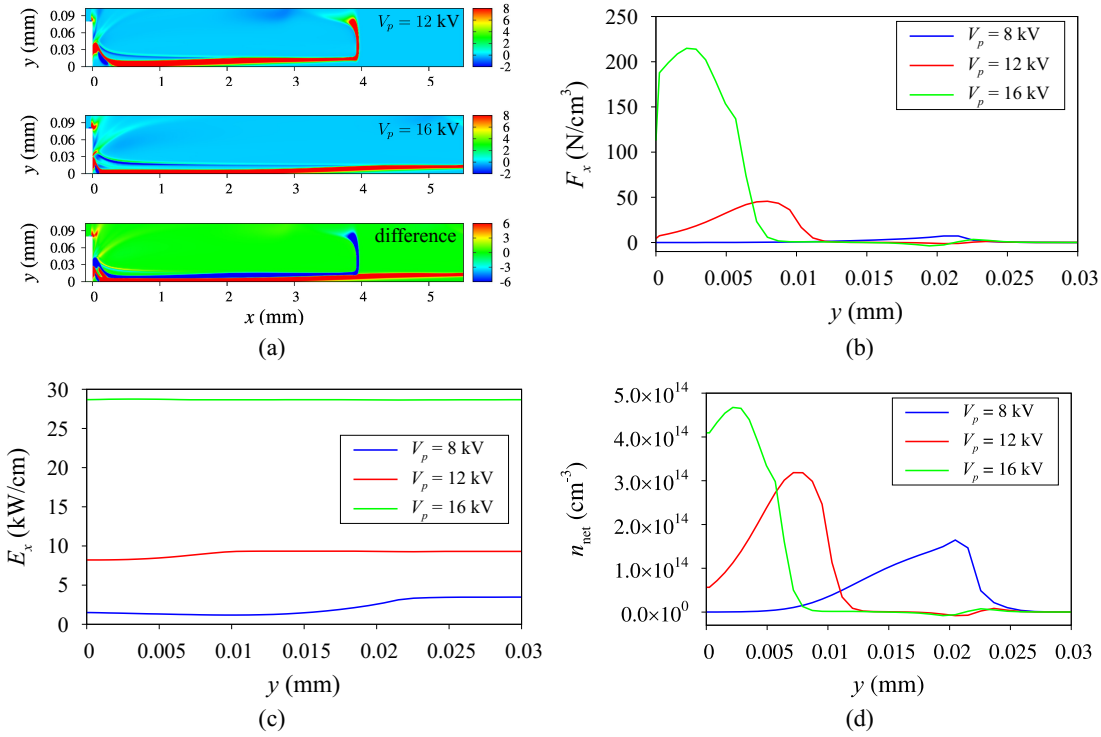

Figure 5.4: Analysis of the difference in EHD body force under different voltage amplitudes for positive polarity: (a) EHD body force field; (b) EHD body force in the cross-section $x = 0.5$ mm; (c) streamwise component of electric field; (d) net charge density.

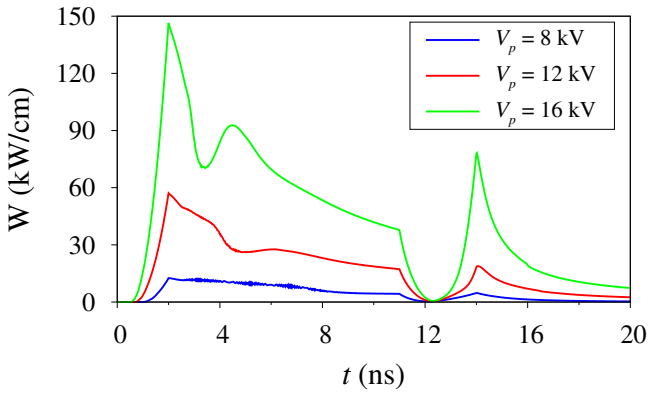

Figure 5.5: Time trace of maximum potential heat source under different voltage amplitudes for positive polarity.

Table 5.2: Test cases for study on influence of dielectric permittivity for positive polarity.

Case	V_p [kV]	ε_d	d [mm]
PE-1	12	4	0.5
PE-2	12	8	0.5
PE-3	12	16	0.5

to streamer formation. However, there are no experimental evidences in [20] to show the current or electric field under different dielectric permittivities due to the difficulty in experimental measurement. In this section, we compare our numerical results with previous experiments. Good agreements with the experimental results are observed. With the help of comprehensive numerical results, we can analyze the current and electric field, as well as the charged particle number density, helping to have a better understanding of the effect of dielectric permittivity.

Three cases with three different dielectric permittivities are computed, and the voltage amplitude is fixed as $V_p = 12$ kV; the dielectric thickness is fixed as $d = 0.5$ mm, as shown in Table 5.2.

The discharge currents under different dielectric permittivities are shown in Fig. 5.6. It is shown that the discharge current is slightly influenced by the dielectric permittivity, and the discharge current increase slightly with the dielectric permittivity, which is consisitent with the conclusion in [20]. The discharge currents at $t = 2$ ns under $\varepsilon_d = 4$, 8, 16 are 8.57, 9.58, 10.2 A/cm, respectively.

The streamer propagations under different dielectric permittivities are shown in Fig. 5.7. When the dielectric permittivity varies from 4 to 16, the propagation velocities of the streamers are almost the same. It is indicate that the streamer propagation is not so sensitive to the dielectric permittivity when $V_p = 12$ kV, $d = 0.5$ mm.

The time traces of the streamwise component of domain-integrated EHD body

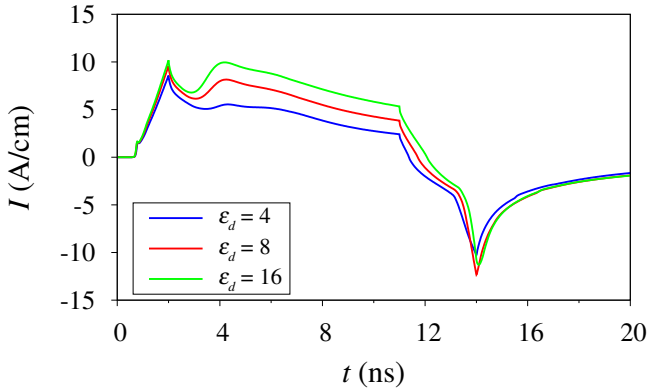

Figure 5.6: Discharge current under different dielectric permittivities for positive polarity.

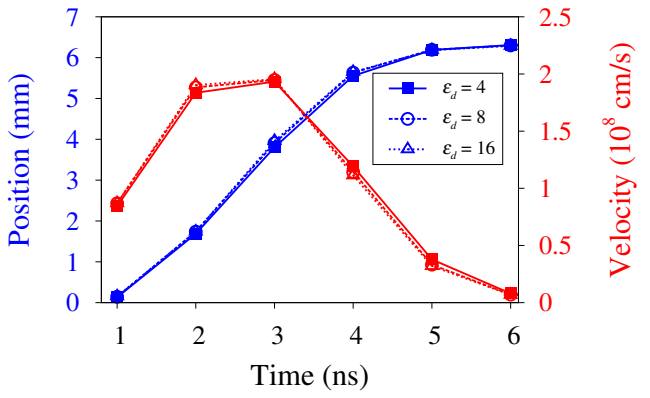

Figure 5.7: Streamer propagation under different dielectric permittivities for positive polarity.

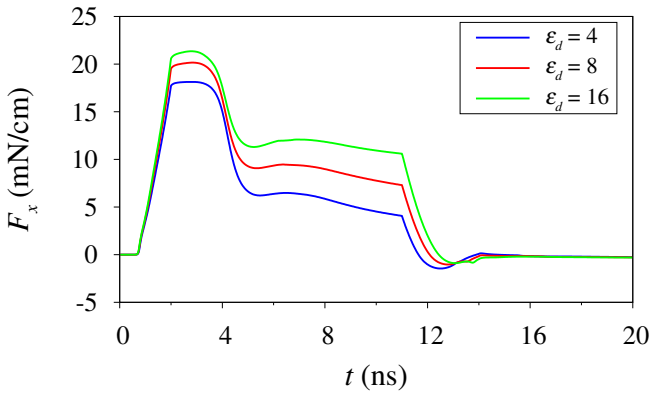

Figure 5.8: Time trace of streamwise domain-integrated EHD body force under different dielectric permittivities for positive polarity.

force under different dielectric permittivities are shown in Fig. 5.8. The streamewise component of domain-integrated EHD body force F_x increase with the dielectric permittivity. The streamewise component of domain-integrated EHD body force F_x at $t = 2$ ns are 17.7, 19.5, 20.6 mN/cm when the dielectric permittivity $\varepsilon_d = 4$, 8, 16.

The EHD body force fields under $\varepsilon_d = 4$, 16 and the difference between them at $t = 3$ ns are shown in Fig. 5.9(a). The difference still mainly appears in the sheath region. From the distribution of F_x in the cross-section $x = 0.5$ mm (Fig. 5.9(b)), it is clearly shown that higher F_x is observed under larger dielectric permittivity. The streamwise component of electric field and net charge number density in the cross-section $x = 0.5$ mm are also compared, as shown in Figs. 5.9(c-d). The streamwise component of electric field E_x increase slightly with the dielectric permittivity and the distribution of E_x seems to translate upward with the increase of dielectric permittivity. The net charge density n_{net} also slightly increase with the dielectric permittivity, and the distribution of F_x resemble that of n_{net}. Hence, both E_x and n_{net} are responsible for the difference of F_x under different dielectric permittivities.

The time traces of the domain-integrated heat source under different dielectric permittivities are shown in Fig. 5.10. The heat source W increase with the dielectric

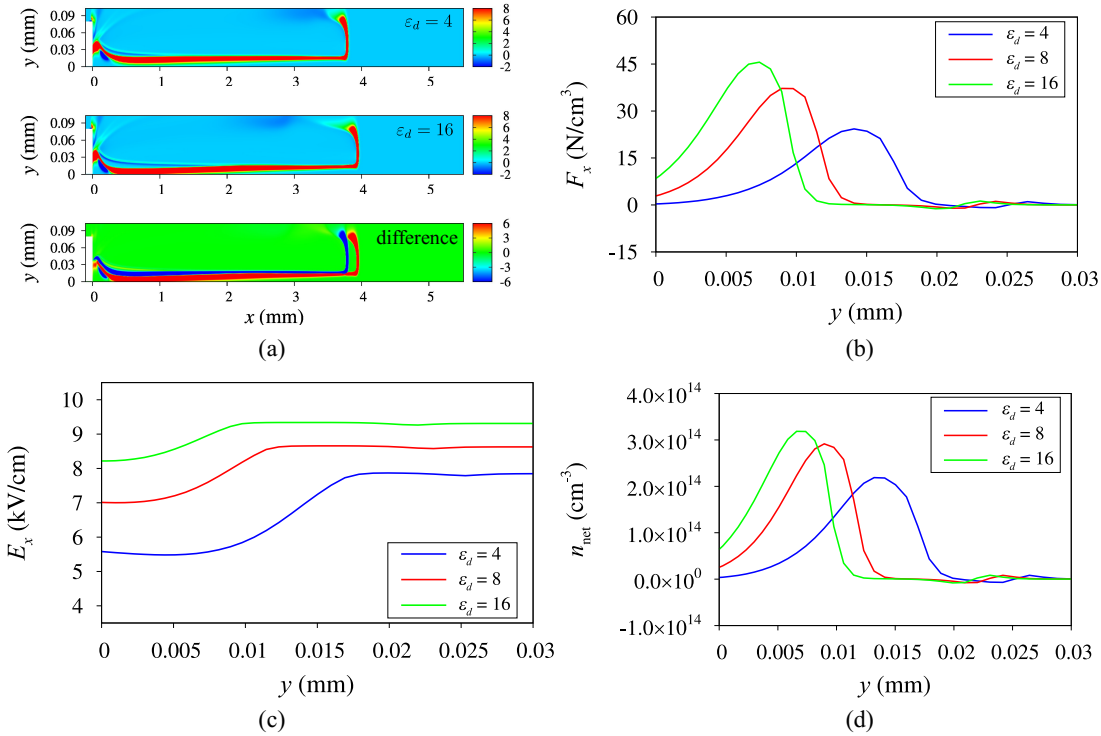

Figure 5.9: Analysis of the difference in EHD body force under different dielectric permittivities for positive polarity: (a) EHD body force field; (b) EHD body force in the cross-section $x = 0.5$ mm; (c) streamwise component of electric field; (d) net charge density.

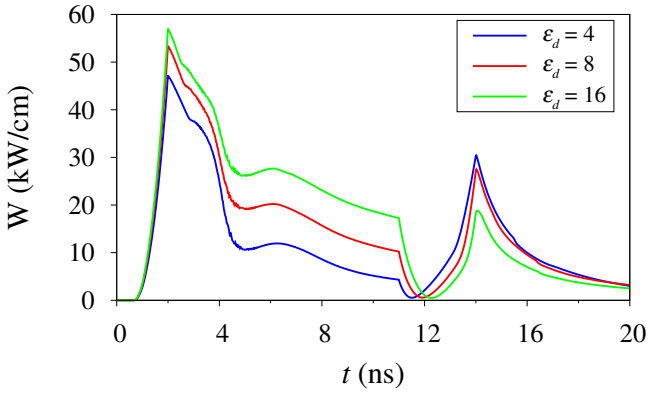

Figure 5.10: Time trace of maximum potential heat source under different dielectric permittivities for positive polarity.

Table 5.3: Test cases for study on influence of dielectric thickness for positive polarity.

Case	V_p [kV]	ε_d	d [mm]
PD-1	12	16	0.25
PD-2	12	16	0.5
PD-3	12	16	0.75

permittivity. The total heating energies during 20 ns under $\varepsilon_d = 4$, 8, 16 are 0.2438, 0.2985, 0.3412 mJ/cm, respectively.

5.2.3 Influence of dielectric thickness

Three cases with three different dielectric thicknesses are computed, and the voltage amplitude is fixed as $V_p = 12$ kV; the dielectric permittivity is fixed as $\varepsilon_d = 16$, as shown in Table 5.3.

The discharge currents under different dielectric thicknesses are shown in Fig. 5.11. The current profile of case $d = 0.25$ mm is quite different from those of case $d = 0.25$ mm and 0.75 mm. A significant peak is seen at about $t = 3$ ns in the case of $d = 0.25$ mm. Besides, the current of case $d = 0.25$ mm is obviously higher than those of case $d = 0.5$ mm and 0.75 mm. Generally, the current increase

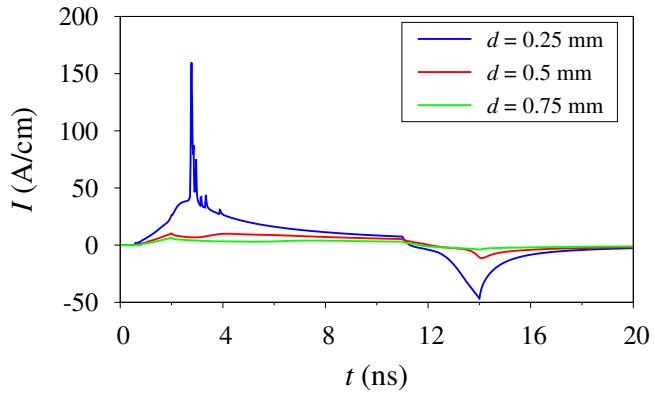

Figure 5.11: Discharge current under different dielectric thicknesses for positive polarity.

with decreasing the dielectric thickness. The current at $t = 2$ ns is 26.4, 10.2 and 6.51 A/cm when $d = 0.25$ mm, 0.5 mm and 0.75 mm, while the negative peak current at $t = 14$ ns is -46.6, -10.8 and -3.79 A/cm.

The streamer propagations under different dielectric thicknesses are shown in Fig. 5.12. During the first 2 ns, the streamer propagates apparently slower with the increase of dielectric thickness. The propagation velocities of the streamer at $t = 2$ ns under $d = 0.25$, 0.5, 0.75 mm are 2.03, 1.90, 1.59×10^8 cm/s. After 2 ns, the streamer velocity decreases quickly under $d = 0.25$ mm, and those under $d = 0.5$ mm and 0.75 mm start to decrease until $t = 3$ ns. The propagation of the streamer after 4 ns is mainly restricted by the length of the encapsulated electrode.

The time traces of the streamwise component of domain-integrated EHD body force under different dielectric thicknesses are shown in Fig. 5.13. It is shown that F_x increases with the decrease of the dielectric thickness, and that F_x increases apparently when decreasing d from 5 mm to 2.5 mm. The EHD body forces F_x at $t = 2$ ns are 42.6, 20.6, 14.4 mN/cm when the dielectric thickness $d = 0.75$ mm, 0.5 mm and 0.25 mm, respectively. The result indicates that thin dielectric thickness is preferred in term of the generation of EHD body force. However, the discharge current increase with the decrease of dielectric thickness (See, current peak

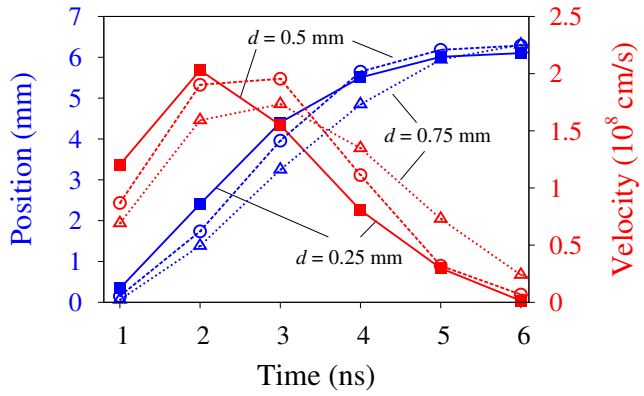

Figure 5.12: Streamer propagation under different dielectric thicknesses for positive polarity.

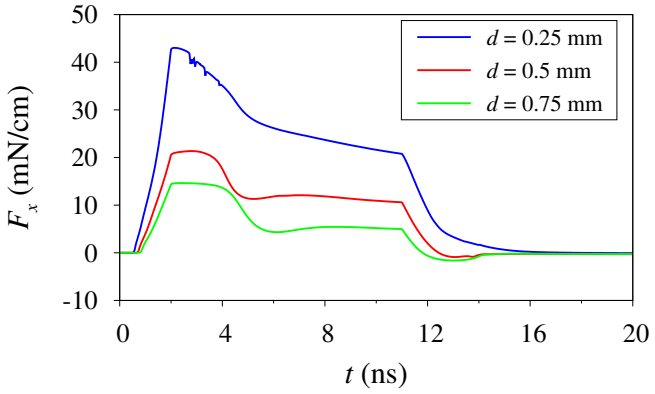

Figure 5.13: Time trace of streamewise domain-integrated EHD body force under different dielectric thicknesses for positive polarity.

of case $d = 0.25$ mm at about $t = 3$ ns in Fig. 5.11). Besides, for a specific dielectric material, electrical breakdown is easier to occur under thin dielectric thickness, which restricts the potential of improving body force by using thinner dielectric thickness.

The EHD body force fields under $d = 0.5$ mm, 0.75 mm and the difference between them at $t = 3$ ns are shown in Fig. 5.14(a). The difference still mainly appears in the sheath region. From the distribution of F_x in the cross-section $x = 0.5$ mm (Fig. 5.14(b)), it is clearly shown that higher F_x is observed under thinner dielectric thickness. Both E_x and n_{net} in the near-surface layer increase

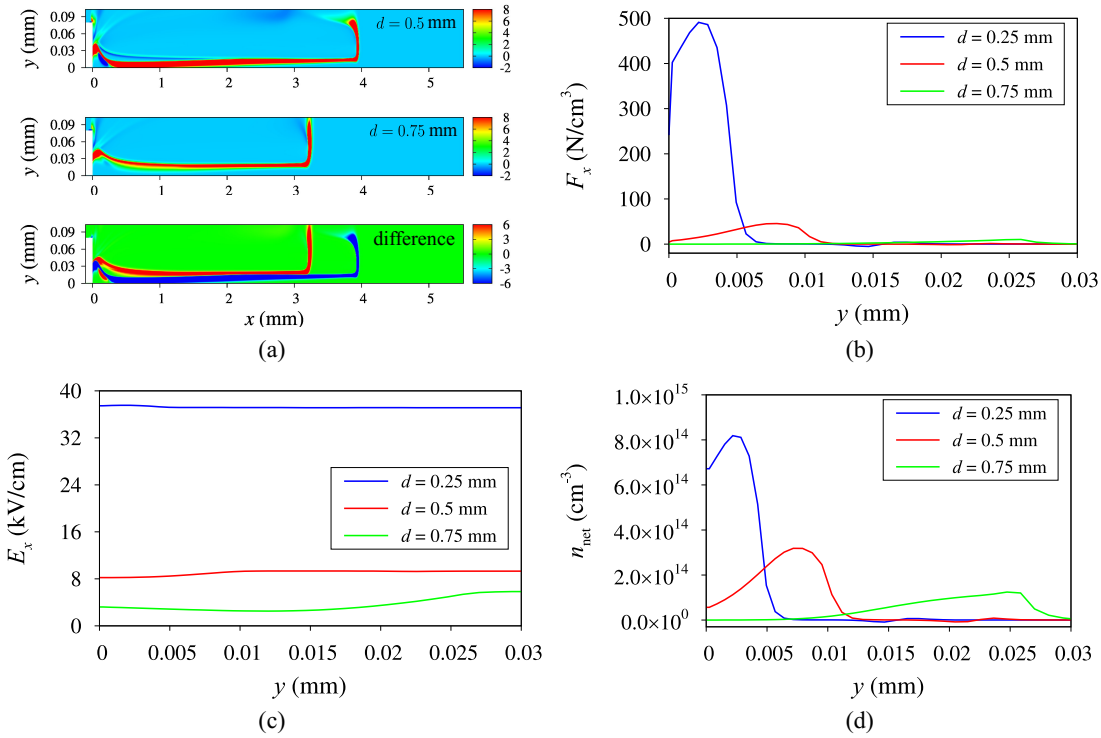

Figure 5.14: Analysis of the difference in EHD body force under different dielectric thicknesses for positive polarity: (a) EHD body force field; (b) EHD body force in the cross section $x = 0.5$ mm; (c) streamwise component of electric field; (d) net charge density.

with decreasing the dielectric thickness, as shown in Figs. 5.14(c-d). Hence, both E_x and n_{net} are responsible for the increase of F_x when decreasing the dielectric thickness.

The time traces of the domain-integrated heat source under different dielectric thicknesses are shown in Fig. 5.15. A significant peak is observed at about $t = 3$ ns under $d = 0.25$ mm, due to the current peak. The total maximal potential heating energies during 20 ns under $d = 0.25$, 0.5 and 0.74 mm are 1.0061, 0.3412 and 0.1525 mJ/cm, respectively. Similarly to EHD body force, in order to improve the maximal potential heat source W, we need to decrease the dielectric thickness. However, electrical breakdown and erosion of the dielectric material are easier to

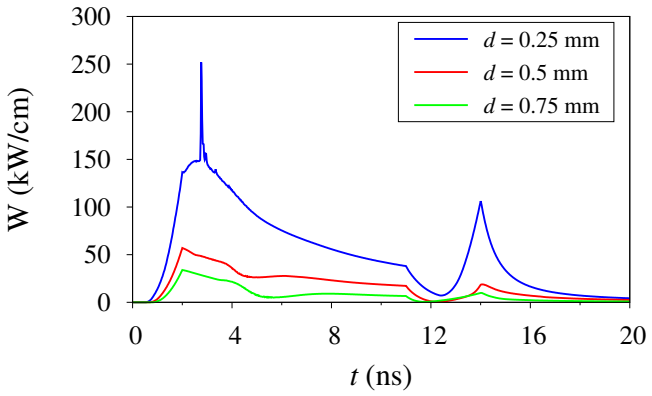

Figure 5.15: Time trace of maximum potential heat source under different dielectric thicknesses for positive polarity.

occur under thinner dielectric thickness. Hence, it is required to balance the improvement of the EHD body force and heat source between the maintenance of the dielectric material in the application of SDBD.

5.3 Parametric study on NSDBD of negative polarity

In this section, the influence of voltage amplitude V_p, dielectric permittivity ε_d, dielectric thickness d, on discharge propagation, generated EHD force and maximal potential heat source of NSDBD under negative electrode polarity are examined.

5.3.1 Influence of applied voltage amplitude

Similarly to positive polarity, three cases with three different voltage amplitudes are computed, and the dielectric permittivity is fixed as $\varepsilon_d = 16$; the dielectric thickness is fixed as $d = 0.5$ mm, as shown in Table 5.4.

The discharge currents under different voltage amplitudes are shown in Fig. 5.16. A significant negative peak is seen at $t = 2$ ns for each voltage amplitude. Besides,

Table 5.4: Test cases for study on influence of applied voltage amplitude for negative polarity.

Case	V_p [kV]	ε_d	d [mm]
NV-1	8	16	0.5
NV-2	12	16	0.5
NV-3	16	16	0.5

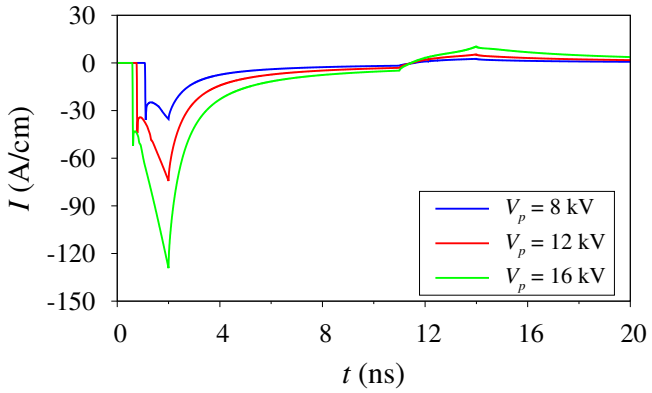

Figure 5.16: Discharge current under different voltage amplitudes for negative polarity.

during the trailing edge of the applied voltage, the currents are positive and positive peaks are observed at about $t = 14$ ns. The positive peak currents are much lower than these negative peaks. With the increase of voltage amplitude, the discharge current increases obviously. The negative peak current at $t = 2$ ns is -35.4, -74.3 and -129.2 A/cm when $V_p = 8$, 12 and 16 kV, while the positive peak current at about $t = 14$ ns is 2.57, 5.35 and 10.4 A/cm.

The time traces of the streamer head position and its propagation velocity under different voltage amplitudes are shown Fig. 5.17. It is clearly shown that the streamer propagates faster with the increase of voltage amplitude. The velocities at $t = 2$ ns are 0.685, 1.1, 1.26×10^8 cm/s when the voltage amplitude $V_p = 8$, 12, 16 kV. Besides, the streamer velocities decrease after about $t = 2$ns. Differently from positive polarity, the length of the encapsulated electrode is enough for the propagation of the negative streamer even when the voltage amplitude $V_p = 16$ kV.

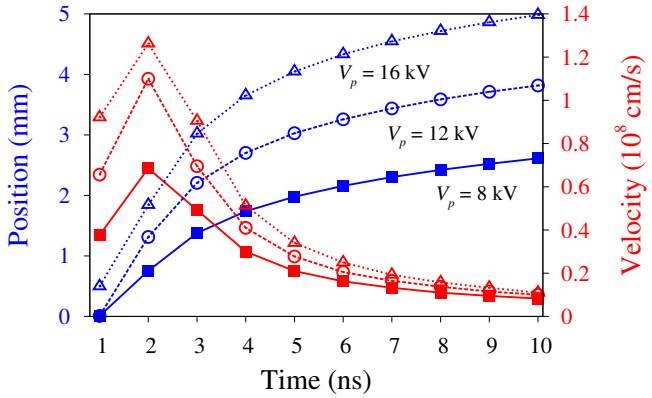

Figure 5.17: Streamer propagation under different voltage amplitudes for negative polarity.

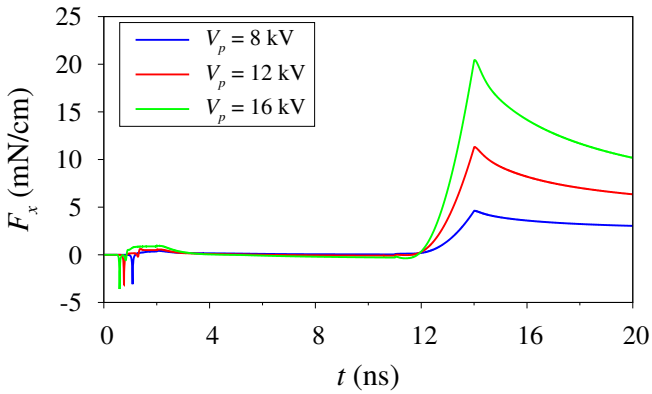

Figure 5.18: Time traces of streamewise domain-integrated EHD body force under different voltage amplitudes for negative polarity.

At $t = 10$ ns, the streamer velocities are about 0.2×10^8 cm/s ,which are much smaller compared with those at $t = 2$ ns. The streamer head positions at $t = 10$ ns under $V_p = 8$, 12, 16 kV are 2.61, 3.82, 4.98 mm, respectively.

The time traces of the streamwise component of domain-integrated EHD body force F_x under different voltage amplitudes V_p are illustrated in Fig. 5.18. Before the trailing edge of the voltage pulse (i.e., $t < 11$ ns), F_x is near-zero due to the absence of near surface sheath layer, as discussed in Chapter 4 and [106]. Positive F_x are observed during the trailing edge of the voltage pulse under the voltage amplitudes computed.

Here, we try to explain the reason for the difference by analyzing the he EHD body force fields under $V_p = 12$ and 16 kV and the difference between them at $t = 14$ ns, as shown in Fig. 5.19(a). Similarly to PEP, the force is concentrated in the sheath region, and the difference in force field is mainly the consequence of plasma sheath, too. The streamwise component of EHD body force F_x in the cross-section $x = 0.5$ mm is depicted in Fig. 5.19(b). It is clearly shown that F_x near the dielectric surface increases with V_p. The streamwise component of electric field E_x and the net charge number density n_{net} in the cross-section of $x = 0.5$ mm are shown in Figs. 5.19(c-d). The distribution of E_x is flat, and the distribution of F_x resembles that of the net charge number density. The electric field E_x increase with the voltage amplitude, as well as the net charge number density n_{net} near the dielectric surface. Hence, both E_x and n_{net} are responsible for the increase of F_x with the increase of voltage amplitude.

The time traces of the domain-integrated heat source under different V_p are illustrated in Fig. 5.20. The maximum values of W appears at $t = 2$ ns, which are 120.2, 402.5 and 962.2 kW/cm when the applied voltage amplitude $V_p = 8$, 12 and 16 kV. The total maximal potential heating energies during 20 ns under $V_p = 8$, 12 and 16 kV are 0.3263, 1.0431 and 2.3993 mJ/cm, respectively.

5.3.2 Influence of dielectric permittivity

The results of three cases with different dielectric permittivities ε_d are compared. Note that the applied voltage amplitude is fixed as $V_p = 12$ kV and the dielectric thickness is fixed as $d = 0.5$ mm, as shown in Table 5.5.

The discharge currents under different dielectric permittivities are shown in Fig. 5.21. The negative peak current at $t = 2$ ns is obviously influenced by the dielectric permittivity, while the positive peak current is almost the same among

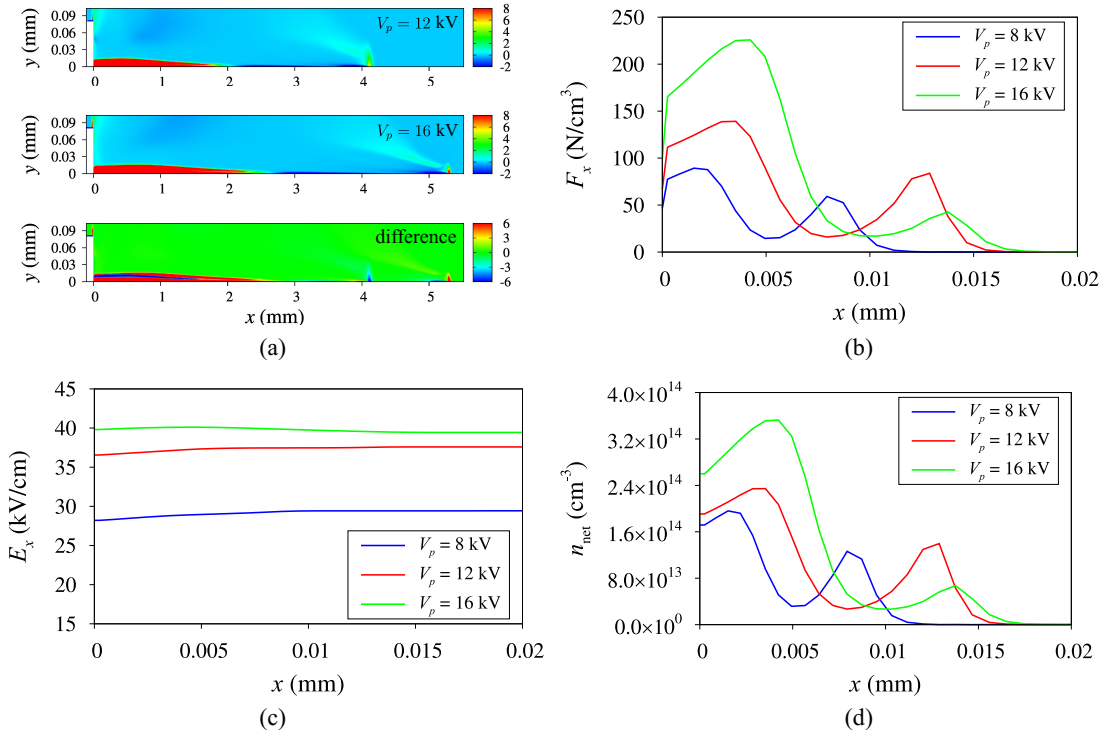

Figure 5.19: Analysis of the difference in EHD body force between different voltage amplitudes for negative polarity: (a) EHD body force field; (b) EHD body force in the cross-section of $x = 0.5$ mm; (c) streamwise component of electric field; (d) net charge number density.

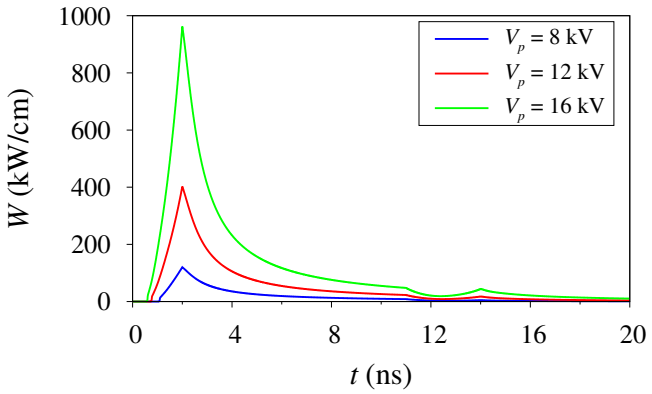

Figure 5.20: Time trace of maximum potential heat source under different voltage amplitudes for negative polarity.

Table 5.5: Test cases for study on effect of dielectric permittivity for negative polarity.

Case	V_p [kV]	ε_d	d [mm]
NE-1	12	4	0.5
NE-2	12	8	0.5
NE-3	12	16	0.5

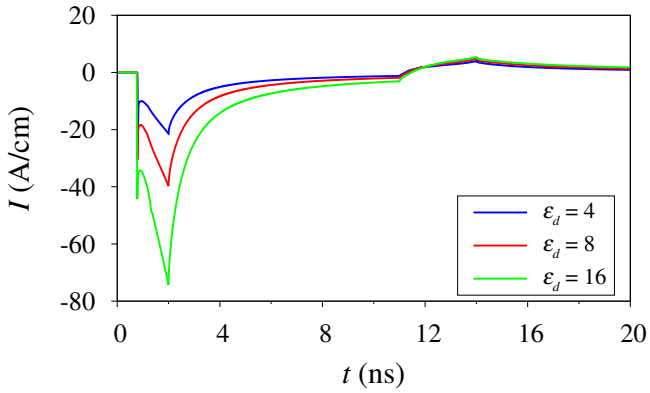

Figure 5.21: Discharge current under different dielectric permittivities for negative polarity.

the dielectric permittivities computed. The discharge currents at $t = 2$ ns are -21.4, -39.7, -74.3 A/cm, while those at $t = 14$ ns are 3.98, 4.78, 5.35 A/cm when the dielectric permittivities $\varepsilon_d = 4$, 8, 16. It is indicated that the discharge current becomes stronger with the increase of dielectric permittivity in the range of $4 < \varepsilon_d < 16$.

The time traces of the streamer head position and its propagation velocity under different dielectric permittivities are shown in Fig. 5.22. The streamer propagates a little faster with the increase of dielectric permittivity. The velocities at $t = 3$ ns are 0.87, 0.775, 0.695×10^8 cm/s when the dielectric permittivity $\varepsilon_d = 4$, 8 and 16. Besides, the streamer propagate longer under lower dielectric permittivity, and the streamer head positions at $t = 10$ ns under $\varepsilon_d = 4$, 8, 16 are 4.74, 4.24, 3.82 mm, respectively.

The time traces of the streamwise component of domain-integrated EHD body

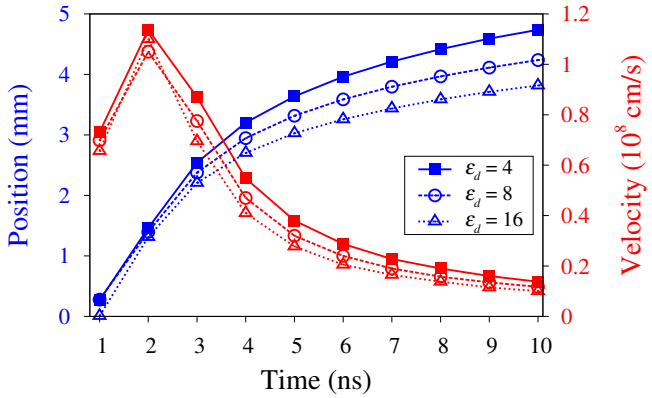

Figure 5.22: Streamer propagation under different dielectric permittivities for negative polarity.

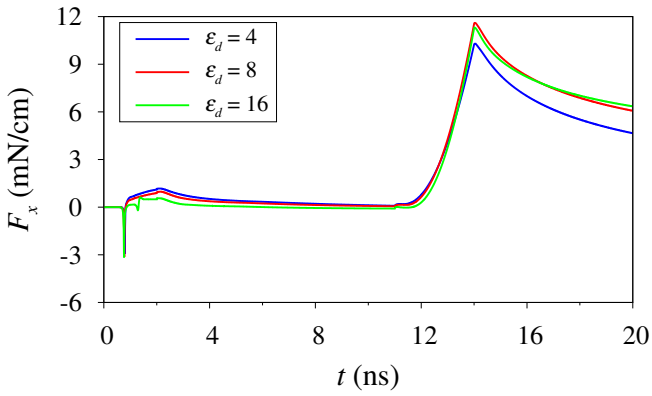

Figure 5.23: Time traces of streamewise domain-integrated EHD body force under different dielectric permittivities for negative polarity.

force under different dielectric permittivities are shown in Fig. 5.23. The EHD body forces are mainly generated during and after the trailing edge of the applied voltage under different dielectric permittivities. The maximum values of F_x at $t = 14$ ns under dielectric permittivity $\varepsilon_d = 4$, 8, 16 are 10.2, 11.5, 11.3 mN/cm. The difference of F_x between case $\varepsilon_d = 4$ and case $\varepsilon_d = 16$ is easy to see, but it is difficult to tell the difference of F_x between case $\varepsilon_d = 8$ and case $\varepsilon_d = 16$. It is indicate that we cannot always increase F_x by increasing dielectric permittivity.

The EHD body force fields under $\varepsilon_d = 4$, 16 and the difference between them at $t = 14$ ns are shown in Fig. 5.24(a). The difference still mainly appears in

Table 5.6: Test cases for study on influence of dielectric thickness for negative polarity.

Case	V_p [kV]	ε_d	d [mm]
ND-1	12	16	0.25
ND-2	12	16	0.5
ND-3	12	16	0.75

the sheath region. Interestingly, from the distribution of F_x in the cross-section of $x = 0.5$ mm, it is shown that, in the area of about $0 < y < 5$ μm and $10 < y < 15$ μm, F_x is larger under $\varepsilon_d = 16$ than that under $\varepsilon_d = 4$. The camelback-like distribution of F_x resembles that of net charge number density, and the position of the second "hump" becomes further away from the dielectric surface with the increase of dielectric permittivity. The streamwise component of electric field E_x increase with the decrease of dielectric permittivity, which is different from PEP. In the region of $0 < y < 5$ μm, the net charge number density n_{net} increase slightly with dielectric permittivity, but the increase of n_{net} in the second "hump" is not observed with the increase of ε_d. Due to the decrease of E_x and increase of n_{net} in the near-surface region, it seems that F_x is not so sensitive to the variance of ε_d.

The time traces of the domain-integrated heat source under different dielectric permittivities are shown in Fig. 5.25. The maximum values of W appear at $t = 2$ ns, which are 116.2, 216.0, 402.5 kW/cm when the dielectric permittivity $\varepsilon_d = 4$, 8 and 16. The total maximal potential heating energies during 20 ns under $\varepsilon_d = 4$, 8, 16 are 0.3718, 0.6126 and 1.0431 mJ/cm, respectively.

5.3.3 Influence of dielectric thickness

The results of three cases with different dielectric thicknesses d are compared. Note that the applied voltage amplitude is fixed as $V_p = 12$ kV and the dielectric permittivity is fixed as $\varepsilon_d = 16$, as shown in Table 5.6.

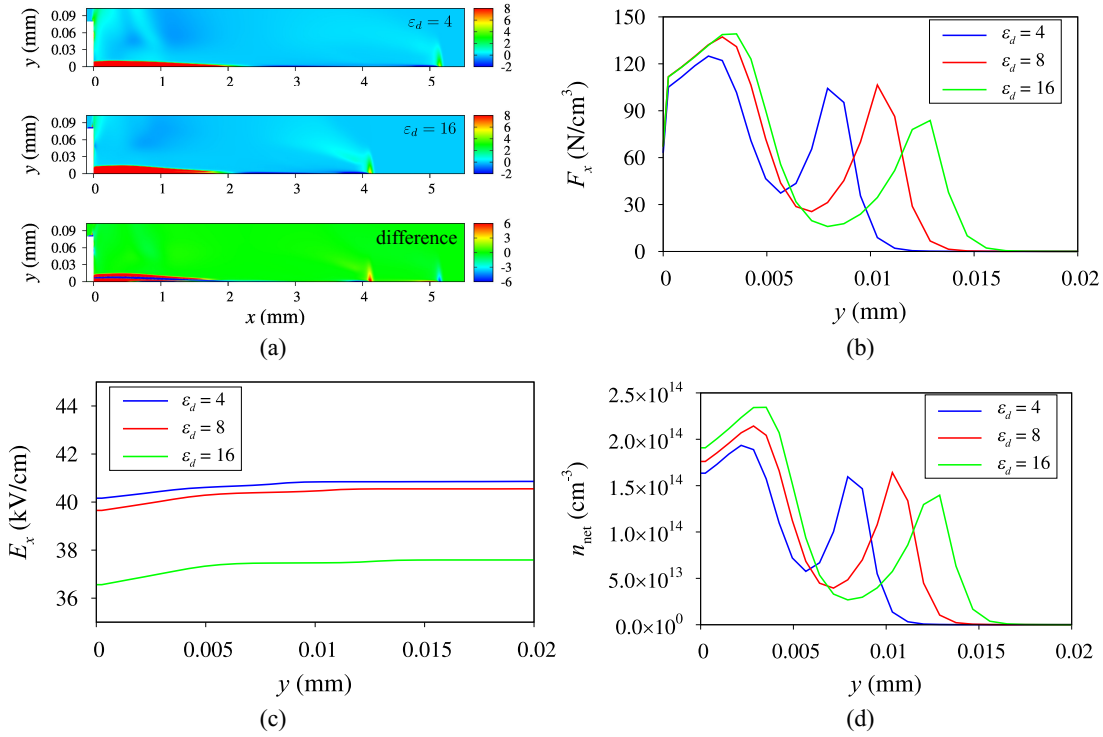

Figure 5.24: Analysis of the difference in EHD body force between different dielectric permittivities for negative polarity: (a) EHD body force field; (b) EHD body force in the cross-section of $x = 0.5$ mm; (c) streamwise component of electric field; (d) net charge number density.

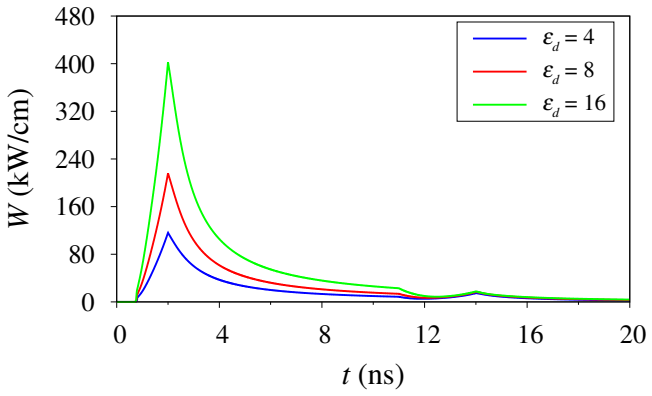

Figure 5.25: Time trace of maximum potential heat source under different dielectric permittivities for negative polarity.

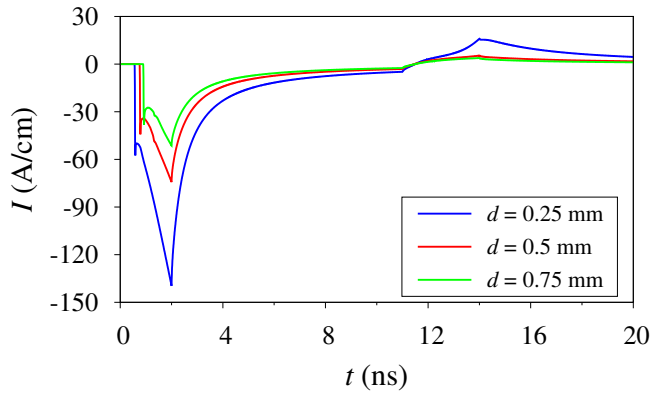

Figure 5.26: Discharge current under different dielectric thicknesses for negative polarity.

The discharge currents under different dielectric thicknesses are shown in Fig. 5.26. The negative current peak at $t = 2$ ns increases apparently with the decrease of dielectric thickness, which are 139.6, 74.3 and 51.4 A/cm when the dielectric thickness $d = 0.25$, 0.5 and 0.75 mm. The positive current peaks at $t = 14$ ns are 15.96, 5.35 and 3.84 A/cm when the dielectric thickness $d = 0.25$, 0.5 and 0.75 mm.

The time traces of the streamer head position and its propagation velocity under different dielectric thicknesses are shown in Fig. 5.22. The developments of the discharge streamer are slightly different under different dielectric thicknesses. During the first 2 ns, the streamer velocity increases with the decrease of dielectric thickness. After that, the change of propagation velocity with dielectric thickness shows opposite tendency. In spite of the slight difference in streamer velocity, the streamer propagation distances under different dielectric thicknesses are essentially the same, which is around 3.8 mm at $t = 10$ ns.

The time traces of the streamwise component of domain-integrated EHD body force under different dielectric thicknesses are shown in Fig. 5.28. The force increase obviously with the decrease of dielectric thickness. The maximum forces during the applied voltage pulse, which appears at about $t = 14$ ns, are 22.6, 11.3, 7.18 mN/cm when the dielectric thickness $d = 0.25$, 0.5, 0.75 mm.

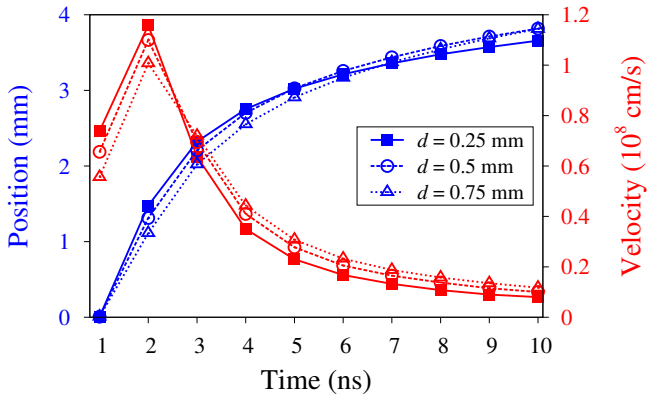

Figure 5.27: Streamer propagation for different dielectric thicknesses for negative polarity.

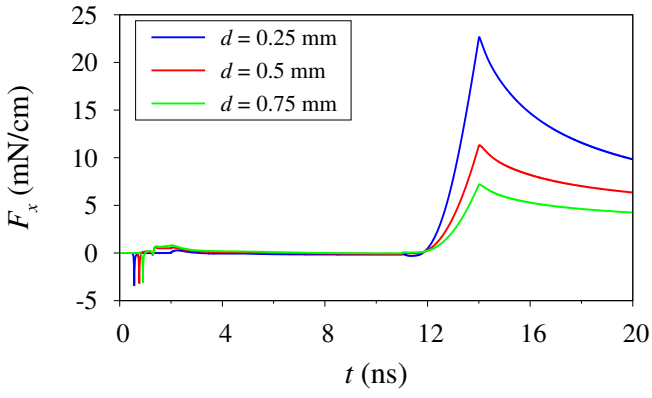

Figure 5.28: Time trace of streamwise domain-integrated EHD body force under different dielectric thicknesses for negative polarity.

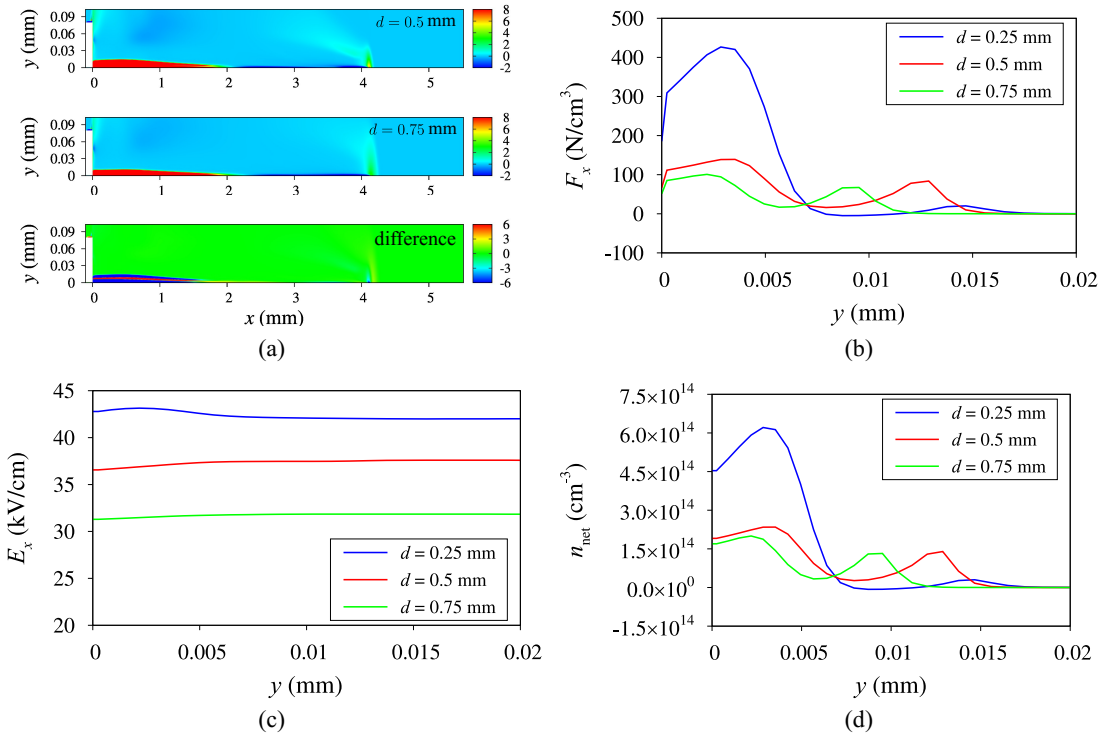

Figure 5.29: Analysis of the difference in EHD body force under different dielectric thicknesses for negative polarity: (a) EHD body force field; (b) EHD body force in the cross section $x = 0.5$ mm; (c) streamwise component of electric field; (d) net charge density.

We try to explain the reason for the difference in F_x by analyzing the EHD body force fields under $d = 0.25$, 0.5, 0.75 mm and the difference between them at $t = 14$ ns, as shown shown in Fig. 5.29(a). The difference still mainly appears in the sheath region. In the area of about $0 < y < 5$ μm, F_x increase apparently with decreasing the dielectric thickness. The camelback-like distribution of F_x and n_{net} tends to lose the second 'hump' away from the dielectric surface with the decrease of dielectric thickness. Besides, The streamwise component of electric field E_x increase with decreasing the dielectric thickness. Due to the increase of E_x and n_{net} in the near-surface region, F_x seems to increase obviously with decreasing the dielectric thickness.

The time traces of the domain-integrated heat source under different dielectric

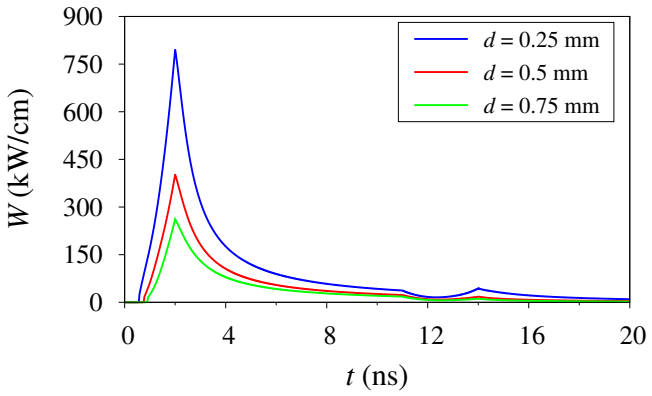

Figure 5.30: Time trace of maximum potential heat source under different dielectric thicknesses for negative polarity.

thicknesses are shown in Fig. 5.30. The peak value of W at $t = 2$ ns increase with the decrease of dielectric thickness, which are 795.9, 402.5, 261.9 kV/cm when the dielectric thickness $d = 0.25$, 0.5 and 0.75 mm. The total maximal potential heating energies during 20 ns under $d = 0.25$, 0.5 and 0.75 mm are 1.9498, 1.0431 and 0.7218 mJ/cm, respectively. However, same problem exist as PEP, i.e., electrical breakdown and erosion of the dielectric material are easier to occur under thinner dielectric thickness. Hence, it is required to balance the improvement of the EHD body force and heat source between the maintenance of the dielectric material in the application of SDBD.

5.4 Comparison with previous researches

I this section, we qualitatively compare our results with the experimental results of Thomas et al. [20]. It is worth noting that the applied voltage is sine wave in the experiment, but the comparison is meaningful because the discharge under sine wave is consist of a series of micro-discharges and the analysis on the single micro-discharge is important to understand the generation of EHD body force. From the experimental result of Thomas et al. [20], it is indicated that for a given voltage

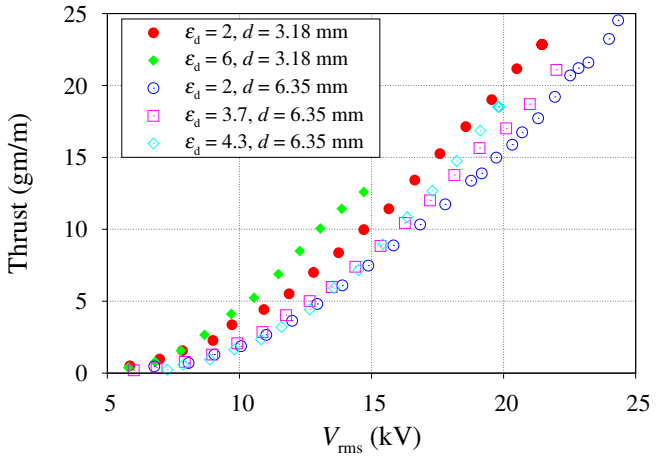

Figure 5.31: Measured thrust versus rms applied voltage of sin wave under various dielectric permittivities and thickness. Figure adapted from [20].

below 'saturation' (i.e. the thrust generated by discharge does not increase with the increase applied voltage), An SDBD-PA with thinner dielectric layer, larger dielectric permittivity produces a larger thrust, as shown in Fig. 5.31. Our simulation results is consistent with the experimental results, i.e., the EHD body force increase with increasing the voltage amplitude, increasing the dielectric permittivity, or decreasing the dielectric thickness.

5.5 Conclusions

Parametric study on the NSDBD is conducted to investigate the influence of several parameters, including voltage amplitude, dielectric permittivity and dielectric thickness, on the discharge process and generated EHD body force and heat source by the SDBD-PA. The numerical results is consistent with the previous experimental results.

When increasing the voltage amplitude, the discharge streamer forms earlier and propagates faster in the initial stage of the discharge process for both PEP and

NEP. Besides, the voltage amplitude does not change the time when the maximum value F_x and W occur under both PEP and NEP. The maximum value of F_x and W increases with V_p. The analysis of the F_x reveal that the increase of F_x is due to the increase of electric field and net charge density in the near-surface sheath layer when increasing the voltage amplitude.

The influence of dielectric permittivity is not as obvious as voltage amplitude. Generally speaking, F_x and W increase slightly with increasing the dielectric permittivity, and the increase of F_x is mainly due to the increase of net charge density in the near-surface layer. The dielectric permittivity has little influence on the discharge propagation of PEP, while the streamer under NEP propagate further with decreasing the dielectric permittivity.

When decreasing the dielectric thickness, it seems that ionization is more easily to take place, and both the positive and negative streamer form early and propagate fast in the initial stage of the discharge process. Both F_x and W increase obviously with decreasing the dielectric thickness. Similarly to voltage amplitude and dielectric permittivity, the increase of F_x is mainly due to the increase of net charge density in near-surface sheath layer. However, one cannot always decrease the dielectric thickness to improve the generated EHD body force and heat source by SDBD-PA, for electric breakdown and erosion of the dielectric material are easier to occur under thinner dielectric thickness.

Chapter 6

Conclusions

Two-dimensional fluid-model of an SDBD-PA is conducted in the present study. The grid resolutions in previous fluid-model of SDBD-PAs differ from 1–100 μm, so grid-convergence study is conducted to check the influence of grid resolution on the computational results. Based on the grid-convergence study, a systematic numerical investigation of the nanosecond-pulsed SDBD evolution under positive (PEP) and negative electrode polarity (NEP) is performed. In order to improve the flow control capability of SDBD-PA, parametric study is conducted. In this chapter, the important findings will be summarized.

6.1 Concluding remarks

1. Grid-convergence study When a positive nanosecond voltage pulse is applied to the upper electrode, a streamer forms in the vicinity of upper electrode and propagates along the dielectric with a maximum propagation velocity of 2×10^8 cm/s. A plasma sheath layer with low electron density exists between the streamer and the dielectric surface. It is found that the simulation result is not sensitive to the streamwise (x) grid spacing, whereas the wall-normal (y) grid spacing is critical to correctly reproduced the structure and dynamics of streamer. When

the thickness of the first layer above the dielectric varies from 2.5 μm to 1.25 μm, the computed streamer propagation velocity abruptly increased. The transports of electrons near the dielectric surface during the nanosecond voltage pulse are found to be quite different between the cases with the finer resolution and the coarser resolution. It is found the coarse grid will lead to the underestimated drift-diffusion flux, resulting in rapid increase of electron density once the electric field reach the ionization threshold.

2. Discharge process under PEP and NEP Two discharge strokes are observed under both PEP and NEP. The first discharge stroke occurs at the leading edge of the applied voltage pulse, while the second discharge stroke occurs at the trailing edge. During the first discharge stroke, discharge streamer forms in the vicinity of the upper electrode. The electron-ion density in the streamer is high, which is of the order of 10^{14}–10^{15} cm^{-3} for PEP and 10^{15}–10^{16} cm^{-3} for NEP. For PEP, around 20 μm-thick plasma sheath layer, characterized by low electron density and high electric field, forms between the streamer and dielectric surface. For NEP, the streamer is attached to the dielectric surface and plasma sheath layer is not observed. For the present $V_p = \pm 12$ kV nanosecond pulse, the maximum propagation velocity of the discharge streamer is 2×10^8 cm/s for PEP and 1×10^8 cm/s for NEP. During the second discharge stroke, for PEP, the plasma sheath layer decays and the electron density near the dielectric surface increases along with the decrease of the electric field in the sheath layer. For NEP, a plasma sheath layer forms near the dielectric surface with the detachment of the streamer from the dielectric surface, which is similar to the sheath layer of PEP during the first discharge stroke. Due to the high electric field and net charge density in the sheath layer, a strong downstream body force is generated when the plasma sheath layer exists.

3. Parametric study When increasing the voltage amplitude, the discharge streamer forms earlier and propagates faster in the initial stage of the discharge process for both PEP and NEP. It is found that the increase of F_x is due to the increase of electric field and net charge density in the near-surface sheath layer when increasing the voltage amplitude. The influence of dielectric permittivity is not as obvious as voltage amplitude. Generally speaking, F_x and W increase slightly with increasing the dielectric permittivity, and the increase of F_x is mainly due to the increase of net charge density in the near-surface layer. The dielectric permittivity has little influence on the discharge propagation of PEP, while the streamer under NEP propagate further with decreasing the dielectric permittivity. When decreasing the dielectric thickness, it seems that ionization is more easily to take place, and both the positive and negative streamer form early and propagate fast in the initial stage of the discharge process. Both F_x and W increase obviously with decreasing the dielectric thickness. Similarly to voltage amplitude and dielectric permittivity, the increase of F_x is mainly due to the increase of net charge density in near-surface sheath layer. The parametric study suggest that a plasma actuator with high dielectric permittivity, thin dielectric thickness, high breakdown voltage is favourable to improve the its flow-control capability.

6.2 Recommendation for future research

The accurate simulation of an SDBD-PA is still a tough problem. As for the numerical model, the accurate boundary condition of the electron at the dielectric surface is still not clear. In this thesis, we conduct preliminary study on the influence of electron boundary condition at the dielectric surface, but a more comprehensive investigation is still meaningful for the future research.

Strictly speaking, the electric field should reduce to zero at infinity. However, in the past and present numerical fluid models, simple Neumann boundary condition for electric potential is assumed at the outer boundary of the computational domain. The influence of such approximation on the computational results still needs further investigations.

In the present study, we just consider the discharge during one nanosecond pulse. In the application of SDBD-PA, no mater under NSDBD or ACDBD, a series of micro-discharges are generated [78], and the development of a micro-discharge is affected by the previous micro-discharges. Investigations on such influence is important for the application of SDBD-PAs.

As for the flow response on the plasma actuation, it is difficult to couple the flow simulation with the plasma simulation due to the segregation of time scales between airflow and plasma. One possible way is to add the body force and heat source obtained from the present results as the source term to the governing equations for a fluid flow, i.e., the Navier-Stokes equation and the energy equation. In this way, we can obtain the flow response on the plasma actuation and investigate the capability of plasma flow control.

Bibliography

[1] V. I. Gibalov and G. J. Pietsch, "The development of dielectric barrier discharges in gas gaps and on surfaces", *Journal of Physics D: Applied Physics* **33**, 2618–2636 (2000).

[2] T. C. Corke, C. L. Enloe, and S. P. Wilkinson, "Dielectric barrier discharge plasma actuators for flow control", *Annual Review of Fluid Mechanics* **42**, 505–529 (2010).

[3] E. Moreau, "Airflow control by non-thermal plasma actuators", *Journal of Physics D: Applied Physics* **40**, 605–636 (2007).

[4] D. V. Roupassov, A. A. Nikipelov, M. M. Nudnova, and A. Y. Starikovskii, "Flow separation control by plasma actuator with nanosecond pulsed-periodic discharge", *AIAA Journal* **47**, 168–185 (2009).

[5] N. Benard and E. Moreau, "Electrical and mechanical characteristics of surface AC dielectric barrier discharge plasma actuators applied to airflow control", *Experiments in Fluids* **55**, 1846 (2014).

[6] S. Roy, P. Zhao, A. DasGupta, and J. Soni, "Dielectric barrier discharge actuator for vehicle drag reduction at highway speeds", *AIP Advances* **6**, 025322 (2016).

[7] L. Dong, G. Gao, K. Peng, W. Wei, C. Li, and G. Wu, "Effects of surface dielectric barrier discharge on aerodynamic characteristic of train", *AIP Advances* **7**, 075112 (2017).

[8] H. Aono, S. Kawai, T. Nonomura, M. Sato, K. Fujii, and K. Okada, "Plasma-actuator burst-mode frequency effects on leading-edge flow-separation control at Reynolds number 2.6×10^5", *AIAA Journal* **55**, 3789–3806 (2017).

[9] I. N. Kosarev, V. I. Khorunzhenko, E. I. Mintoussov, P. N. Sagulenko, N. A. Popov, and S. M. Starikovskaia, "A nanosecond surface dielectric barrier discharge at elevated pressures: time-resolved electric field and efficiency of initiation of combustion", *Plasma Sources Science and Technology* **21**, 045012 (2012).

[10] S. Starikovskaia, "Plasma-assisted ignition and combustion: nanosecond discharges and development of kinetic mechanisms", *Journal of Physics D: Applied Physics* **47**, 353001 (2014).

[11] E. M. Anokhin, D. N. Kuzmenko, S. V. Kindysheva, V. R. Soloviev, and N. L. Aleksandrov, "Ignition of hydrocarbon : air mixtures by a nanosecond surface dielectric barrier discharge", *Plasma Sources Science and Technology* **24**, 045014 (2015).

[12] T. C. Corke, M. L. Post, and D. M. Orlov, "SDBD plasma enhanced aerodynamics: concepts, optimization and applications", *Progress in Aerospace Sciences* **43**, 193–217 (2007).

[13] T. C. Corke, M. L. Post, and D. M. Orlov, "Single dielectric barrier discharge plasma enhanced aerodynamics: physics, modeling and applications", *Experiments in Fluids* **46**, 1–26 (2009).

[14] J. J. Wang, K. S. Choi, L. H. Feng, T. N. Jukes, and R. D. Whalley, "Recent developments in DBD plasma flow control", *Progress in Aerospace Sciences* **62**, 52–78 (2013).

[15] A. Starikovskiy and N. Aleksandrov, "Plasma-assisted ignition and combustion", *Progress in Energy and Combustion Science* **39**, 61–110 (2013).

[16] W. Siemens, "Ueber die elektrostatische induction und die verzögerung des stroms in flaschendrähten", *Annalen der Physik und Chemie* **178**, 66–122 (1857).

[17] U. Kogelschatz, "Dielectric-barrier discharges: their History, discharge physics, and industrial applications", *Plasma Chemistry and Plasma Processing* **23**, 1–46 (2003).

[18] C. Punset, J. P. Boeuf, and L. C. Pitchford, "Two-dimensional simulation of an alternating current matrix plasma display cell: cross-talk and other geometric effects", *Journal of Applied Physics* **83**, 1884–1897 (1998).

[19] Y. Suzen and G. Huang, "Simulations of flow separation control using plasma actuators", in: *44th AIAA Aerospace Sciences Meeting and Exhibit*, AIAA-2006-877.

[20] F. O. Thomas, T. C. Corke, M. Iqbal, A. Kozlov, and D. Schatzman, "Optimization of dielectric barrier discharge plasma actuators for active aerodynamic flow control", *AIAA Journal* **47**, 2169–2178 (2009).

[21] J. Little, M. Nishihara, I. Adamovich, and M. Samimy, "High-lift airfoil trailing edge separation control using a single dielectric barrier discharge plasma actuator", *Experiments in Fluids* **48**, 521–537 (2010).

[22] G. Correale, I. B. Popov, A. E. Rakitin, A. Y. Starikovskii, S. J. Hulshoff, and L. L. M. Veldhuis, "Flow separation control on airfoil with pulsed nanosecond discharge actuator", in: *49th AIAA Aerospace Sciences Meeting including the New Horizons Forum and Aerospace Exposition*, AIAA-2011-1079.

[23] Y. Wu, Y. Li, H. Liang, and J. Li, "Nanosecond pulsed discharge plasma actuation: characteristics and flow control performance", in: *45th AIAA Plasmadynamics and Lasers Conference*, AIAA-2014-2118.

[24] K. Kato, C. Breitsamter, and S. Obi, "Flow separation control over a G̈o 387 airfoil by nanosecond pulse-periodic discharge", *Experiments in Fluids* **55**, 3–14 (2014).

[25] J. G. Zheng, Y. D. Cui, Z. J. Zhao, J. Li, and B. C. Khoo, "Investigation of airfoil leading edge separation control with nanosecond plasma actuator", *Physical Review Fluids* **1**, 073501 (2016).

[26] L. Wang, C. Wong, Z. Lu, Z. Wu, and Y. Zhou, "Novel sawtooth dielectric barrier discharge plasma actuator for flow separation control", *AIAA Journal* **55**, 1405–1416 (2017).

[27] Y. Anzai, K. Fukagata, P. Meliga, E. Boujo, and F. Gallaire, "Numerical simulation and sensitivity analysis of a low-Reynolds-number flow around a square cylinder controlled using plasma actuators", *Physical Review Fluids* **2**, 043901 (2017).

[28] S. Sekimoto, T. Nonomura, and K. Fujii, "Burst-mode frequency effects of dielectric barrier discharge plasma actuator for separation control", *AIAA Journal* **55**, 1385–1392 (2017).

[29] A. Starikovskiy, A. Rakitin, G. Correale, A. Nikipelov, T. Urushihara, and T. Shiraishi, "Ignition of hydrocarbon-air mixtures with non-equilibrium plasma at elevated pressures", in: *50th AIAA Aerospace Sciences Meeting including the New Horizons Forum and Aerospace Exposition*, AIAA-2012-828.

[30] M. A. Boumehdi, S. A. Stepanyan, P. Desgroux, G. Vanhove, and S. M. Starikovskaia, "Ignition of methane- and n -butane-containing mixtures at high pressures by pulsed nanosecond discharge", *Combustion and Flame* **162**, 1336–1349 (2015).

[31] I. A. Kossyi, A. Y. Kostinsky, A. A. Matveyev, and V. P. Silakov, "Kinetic scheme of the non-equilibrium discharge in nitrogen-oxygen mixtures", *Plasma Sources Science and Technology* **1**, 207–220 (1992).

[32] J. R. Roth and X. Dai, "Optimization of the aerodynamic plasma actuator as an electrohydrodynamic (EHD) electrical device", in: *44th AIAA Aerospace Sciences Meeting and Exhibit*, AIAA-2006-1203.

[33] T. Abe, Y. Takizawa, S. Sato, and N. Kimura, "A parametric experimental study for momentum transfer by plasma actuator", in: *45th AIAA Aerospace Sciences Meeting and Exhibit*, January.

[34] A. Y. Starikovskii, A. A. Nikipelov, M. M. Nudnova, and D. V. Roupassov, "SDBD plasma actuator with nanosecond pulse-periodic discharge", *Plasma Sources Science and Technology* **18**, 34015 (2009).

[35] A. Starikovskii, M. Nudnova, S. Kindusheva, and N. Aleksahdrov, "Rate of plasma thermalization of pulsed nanosecond surface dielectric barrier discharge", in: *48th AIAA Aerospace Sciences Meeting Including the New Horizons Forum and Aerospace Exposition*, AIAA-2010-465.

[36] J. G. Zheng, Z. J. Zhao, J. Li, Y. D. Cui, and B. C. Khoo, "Numerical simulation of nanosecond pulsed dielectric barrier discharge actuator in a quiescent flow", *Physics of Fluids* **26**, 036102 (2014).

[37] G. Correale, T. Michelis, D. Ragni, M. Kotsonis, and F. Scarano, "Nanosecond-pulsed plasma actuation in quiescent air and laminar boundary layer", *Journal of Physics D: Applied Physics* **47**, 105201 (2014).

[38] S. O. Macheret, M. N. Shneider, and R. B. Miles, "Modeling of air plasma generation by repetitive high-voltage nanosecond pulses", *IEEE Transactions on Plasma Science* **30**, 1301–1314 (2002).

[39] J. P. Boeuf and L. C. Pitchford, "Electrohydrodynamic force and aerodynamic flow acceleration in surface dielectric barrier discharge", *Journal of Applied Physics* **97**, 103307 (2005).

[40] G. E. Georghiou, A. P. Papadakis, R. Morrow, and A. C. Metaxas, "Numerical modelling of atmospheric pressure gas discharges leading to plasma production", *Journal of Physics D: Applied Physics* **38**, 303–328 (2005).

[41] A. V. Likhanskii, M. N. Shneider, S. O. MacHeret, and R. B. Miles, "Modeling of dielectric barrier discharge plasma actuators driven by repetitive nanosecond pulses", *Physics of Plasmas* **14**, 073501 (2007).

[42] T. Unfer and J. P. Boeuf, "Modeling and comparison of sinusoidal and nanosecond pulsed surface dielectric barrier discharges for flow control", *Plasma Physics and Controlled Fusion* **52**, 124019 (2010).

[43] S. Yamamoto and K. Fukagata, "Numerical simulation of a plasma actuator based on ion transport", *Journal of Applied Physics* **113**, 243302 (2013).

[44] J. Poggie, I. Adamovich, N. Bisek, and M. Nishihara, "Numerical simulation of nanosecond-pulse electrical discharges", *Plasma Sources Science and Technology* **22**, 15001 (2013).

[45] Y. Zhu, Y. Wu, W. Cui, Y. Li, and M. Jia, "Modelling of plasma aerodynamic actuation driven by nanosecond SDBD discharge", *Journal of Physics D: Applied Physics* **46**, 355205 (2013).

[46] M. Abdollahzadeh, J. C. Páscoa, and P. J. Oliveira, "Two-dimensional numerical modeling of interaction of micro-shock wave generated by nanosecond plasma actuators and transonic flow", *Journal of Computational and Applied Mathematics* **270**, 401–416 (2014).

[47] N. Y. Babaeva, D. V. Tereshonok, and G. V. Naidis, "Fluid and hybrid modeling of nanosecond surface discharges: effect of polarity and secondary electrons emission", *Plasma Sources Science and Technology* **25**, 044008 (2016).

[48] K. Kourtzanidis and L. L. Raja, "Three-electrode sliding nanosecond dielectric barrier discharge actuator: modeling and physics", *AIAA Journal* **55**, 1393–1404 (2017).

[49] Y. Zhu, S. Shcherbanev, B. Baron, and S. Starikovskaia, "Nanosecond surface dielectric barrier discharge in atmospheric pressure air: I. measurements and 2D modeling of morphology, propagation and hydrodynamic perturbations", *Plasma Sources Science and Technology* **26**, 125004 (2017).

[50] M. Kotsonis, S. Ghaemi, L. Veldhuis, and F. Scarano, "Measurement of the body force field of plasma actuators", *Journal of Physics D: Applied Physics* **44**, 045204 (2011).

[51] T. Albrecht, T. Weier, G. Gerbeth, H. Metzkes, and J. Stiller, "A method to estimate the planar, instantaneous body force distribution from velocity field measurements", *Physics of Fluids* **23**, 10–14 (2011).

[52] N. Benard, A. Debien, and E. Moreau, "Time-dependent volume force produced by a non-thermal plasma actuator from experimental velocity field", *Journal of Physics D: Applied Physics* **46**, 245201 (2013).

[53] W. Shyy, B. Jayaraman, and A. Andersson, "Modeling of glow discharge-induced fluid dynamics", *Journal of Applied Physics* **92**, 6434–6443 (2002).

[54] B. Jayaraman and W. Shyy, "Flow control and thermal management using dielectric glow discharge concepts", in: *33rd AIAA Fluid Dynamics Conference and Exhibit*, AIAA-2003-3712.

[55] M. R. Visbal, D. V. Gaitonde, and S. Roy, "Control of transitional and turbulent flows using plasma-based actuators", in: *36th AIAA Fluid Dynamics Conference*, AIAA-2006-3230.

[56] M. Visbal and D. Gaitonde, "Control of vortical flows using simulated plasma actuators", in: *44th AIAA Aerospace Sciences Meeting and Exhibit*, AIAA-2006-505.

[57] T. Igarashi, H. Naito, and K. Fukagata, "Direct numerical simulation of flow around a circular cylinder controlled using plasma actuators", *Mathematical Problems in Engineering* **2014**, 1–13 (2014).

[58] Y. Suzen, G. Huang, J. Jacob, and D. Ashpis, "Numerical simulations of plasma based flow control applications", in: *35th AIAA Fluid Dynamics Conference and Exhibit*, AIAA-2005-4633.

[59] M. Sato, T. Nonomura, K. Okada, K. Asada, H. Aono, A. Yakeno, Y. Abe, and K. Fujii, "Mechanisms for laminar separated-flow control using dielectric-barrier-discharge plasma actuator at low Reynolds number", *Physics of Fluids* **27**, 117101 (2015).

[60] H. Fukumoto, H. Aono, M. Tanaka, H. Matsuda, T. Osako, T. Nonomura, A. Oyama, and K. Fujii, "Control of dynamically stalled flowfield around a pitching airfoil by DBD plasma actuator", in: *8th AIAA Flow Control Conference*, AIAA-2016-4239.

[61] T. Ogawa, S. Shimomura, K. Asada, S. Sekimoto, T. Tatsukawa, K. Fujii, and H. Nishida, "Study on the sensing parameters toward better feed-back control of stall separation with DBD plasma actuator", in: *35th AIAA Applied Aerodynamics Conference*, AIAA-2017-3565.

[62] D. Orlov and T. Corke, "Numerical simulation of aerodynamic plasma actuator effects", in: *43rd AIAA Aerospace Sciences Meeting and Exhibit*, AIAA-2005-1083.

[63] D. Orlov, T. Corke, and M. Patel, "Electric circuit model for aerodynamic plasma actuator", in: *44th AIAA Aerospace Sciences Meeting and Exhibit*, AIAA-2006-1206.

[64] D. Orlov, T. Apker, C. He, H. Othman, and T. Corke, "Modeling and experiment of leading edge separation control using SDBD plasma actuators", in: *45th AIAA Aerospace Sciences Meeting and Exhibit*, AIAA-2007-877.

[65] N. A. Popov, "Fast gas heating in a nitrogen–oxygen discharge plasma: I. kinetic mechanism", *Journal of Physics D: Applied Physics* **44**, 285201 (2011).

[66] G. A. Bird, "Monte Carlo simulation of gas flows", *Annual Review of Fluid Mechanics* **10**, 11–31 (1978).

[67] K. Sugimoto and N. Ohnishi, "Toward hybrid simulation of flow generation in DBD plasma actuator", *AIP Conference Proceedings* **1501**, 1408 (2012).

[68] G. J. M. Hagelaar and L. C. Pitchford, "Solving the Boltzmann equation to obtain electron transport coefficients and rate coefficients for fluid models", *Plasma Sources Science and Technology* **14**, 722–733 (2005).

[69] BOLSIG+ CPAT, `http://www.codiciel.fr/plateforme/plasma/bolsig/bolsig.php`.

[70] BOLOS, `https://github.com/aluque/bolos`.

[71] W. L. Morgan and B. M. Penetrante, "ELENDIF: A time-dependent Boltzmann solver for partially ionized plasmas", *Computer Physics Communications* **58**, 127–152 (1990).

[72] A. J. Davies, C. S. Davies, and C. J. Evans, "Computer simulation of rapidly developing gaseous discharges", *Proceedings of the Institution of Electrical Engineers* **118**, 816–823 (1971).

[73] J. P. Boeuf, "A two-dimensional model of dc glow discharges", *Journal of Applied Physics* **63**, 1342–1349 (1988).

[74] J. P. Boeuf, Y. Lagmich, T. Unfer, T. Callegari, and L. C. Pitchford, "Electrohydrodynamic force in dielectric barrier discharge plasma actuators", *Journal of Physics D: Applied Physics* **40**, 652–662 (2007).

[75] J. P. Boeuf, Y. Lagmich, and L. C. Pitchford, "Contribution of positive and negative ions to the electrohydrodynamic force in a dielectric barrier discharge plasma actuator operating in air", *Journal of Applied Physics* **106**, 023115 (2009).

[76] V. Soloviev, V. Krivtsov, A. Konchakov, and N. Malmuth, "Surface barrier discharge simulation in air for constant applied voltage", in: *46th AIAA Aerospace Sciences Meeting and Exhibit*, AIAA-2008-1378.

[77] V. R. Soloviev and V. M. Krivtsov, "Surface barrier discharge modelling for aerodynamic applications", *Journal of Physics D: Applied Physics* **42**, 125208 (2009).

[78] V. R. Soloviev and V. M. Krivtsov, "Mechanism of streamer stopping in a surface dielectric barrier discharge", *Plasma Physics Reports* **40**, 65–77 (2014).

[79] V. R. Soloviev, V. M. Krivtsov, S. A. Shcherbanev, and S. M. Starikovskaia, "Evolution of nanosecond surface dielectric barrier discharge for negative polarity of a voltage pulse", *Plasma Sources Science and Technology* **26**, 014001 (2016).

[80] A. V. Likhanskii, M. N. Shneider, S. O. Macheret, and R. B. Miles, "Modeling of dielectric barrier discharge plasma actuator in air", *Journal of Applied Physics* **103**, 053305 (2008).

[81] A. V. Likhanskii, "Particle-in-cell modeling of the pulsed DBD plasma actuator", in: *40th Fluid Dynamics Conference and Exhibit*, AIAA-2010-5101.

[82] Y. Lagmich, T. Callegari, L. C. Pitchford, and J. P. Boeuf, "Model description of surface dielectric barrier discharges for flow control", *Journal of Physics D: Applied Physics* **41**, 095205 (2008).

[83] H. Nishida and T. Abe, "Numerical analysis of plasma evolution on dielectric barrier discharge plasma actuator", *Journal of Applied Physics* **110**, 013302 (2011).

[84] T. Unfer and J. P. Boeuf, "Modelling of a nanosecond surface discharge actuator", *Journal of Physics D: Applied Physics* **42**, 194017 (2009).

[85] W. Hua and K. Fukagata, "Influence of grid resolution in fluid-model simulation of nanosecond dielectric barrier discharge plasma actuator", *AIP Advances* **8**, 045209 (2018).

[86] K. Nakai, A. Nakano, and H. Nishida, "Validation study of three-fluid plasma modeling of dielectric barrier discharge for plasma actuator", in: *2018 AIAA Aerospace Sciences Meeting*, AIAA-2018-0937.

[87] V. Nikonov, R. Bartnikas, and M. R. Wertheimer, "Surface charge and photoionization effects in short air gaps undergoing discharges at atmospheric pressure", *Journal of Physics D: Applied Physics* **34**, 2979–2986 (2001).

[88] W. S. Kang, J. M. Park, Y. Kim, and S. H. Hong, "Numerical study on influences of barrier arrangements on dielectric barrier discharge characteristics", *IEEE Transactions on Plasma Science* **31**, 504–510 (2003).

[89] S. B. Leonov, I. V. Adamovich, and V. R. Soloviev, "Dynamics of near-surface electric discharges and mechanisms of their interaction with the airflow", *Plasma Sources Science and Technology* **25**, 063001 (2016).

[90] V. Petrishchev, S. Leonov, and I. V. Adamovich, "Studies of nanosecond pulse surface ionization wave discharges over solid and liquid dielectric surfaces", *Plasma Sources Science and Technology* **23**, 065022 (2014).

[91] D. F. Opaits, M. N. Shneider, R. B. Miles, A. V. Likhanskii, and S. O. MacHeret, "Surface charge in dielectric barrier discharge plasma actuators", *Physics of Plasmas* **15**, 073505 (2008).

[92] Y. B. Golubovskii, V. A. Maiorov, J. Behnke, and J. F. Behnke, "Influence of interaction between charged particles and dielectric surface over a homogeneous barrier discharge in nitrogen", *Journal of Physics D: Applied Physics* **35**, 751–761 (2002).

[93] J. Deng, H. Mu, G. Zhang, S. Matsuoka, A. Kumada, and K. Hidaka, "Residual charge distribution of surface leader discharge under positive impulse voltage", *IEEE Transactions on Plasma Science* **41**, 999–1004 (2013).

[94] D. L. Scharfetter and H. K. Gummel, "Large-signal analysis of a silicon read diode oscillator", *IEEE Transactions on Electron Devices* **ED-16**, 65–77 (1969).

[95] P. L. G. Ventzek, R. J. Hoekstra, and M. Kushner, "Two-dimensional modeling of high plasma density inductively coupled sources for materials processing", *Journal of Vacuum Science and Technology B* **12**, 461–477 (1994).

[96] P. A. Vitello, B. M. Penetrante, and J. N. Bardsley, "Simulation of negative-streamer dynamics in nitrogen", *Physical Review E* **49**, 5574–5598 (1994).

[97] G. Dufour and F. Rogier, "Based plasma actuators for flow control : the numerical modeling of dielectric barrier discharge based plasma actuators for flow control : the COPAIER / CEDRE example", *Onera Aerospacelab Journal* **AL-10**, 5 (2015).

[98] T. Unfer, J. P. Boeuf, F. Rogier, and F. Thivet, "An asynchronous scheme with local time stepping for multi-scale transport problems: application to gas discharges", *Journal of Computational Physics* **227**, 898–918 (2007).

[99] S. A. Stepanyan, V. R. Soloviev, and S. M. Starikovskaia, "An electric field in nanosecond surface dielectric barrier discharge at different polarities of the high voltage pulse: spectroscopy measurements and numerical modeling", *Journal of Physics D: Applied Physics* **47**, 485201 (2014).

[100] A. A. Kulikovsky, "A more accurate Scharfetter-Gummel algorithm of electron transport for semiconductor and gas discharge simulation", *Journal of Computational Physics* **119**, 149–155 (1995).

[101] S. Leonov, D. Opaits, R. Miles, and V. Soloviev, "Time-resolved measurements of plasma-induced momentum in air and nitrogen under dielectric barrier discharge actuation", *Physics of Plasmas* **17**, 113505 (2010).

[102] V. R. Soloviev, A. M. Konchakov, V. M. Krivtsov, and N. L. Aleksandrov, "Numerical simulation of a surface barrier discharge in air", *Plasma Physics Reports* **34**, 594–608 (2008).

[103] G. J. M. Hagelaar, F. J. De Hoog, and G. M. W. Kroesen, "Boundary conditions in fluid models of gas discharges", *Physical Review E* **62**, 1452–1454 (2000).

[104] E. I. Mintoussov, S. J. Pendleton, F. G. Gerbault, N. A. Popov, and S. M. Starikovskaia, "Fast gas heating in nitrogen–oxygen discharge plasma: II. energy exchange in the afterglow of a volume nanosecond discharge at moderate pressures", *Journal of Physics D: Applied Physics* **44**, 285202 (2011).

[105] D. L. Rusterholtz, D. A. Lacoste, G. D. Stancu, D. Z. Pai, and C. O. Laux, "Ultrafast heating and oxygen dissociation in atmospheric pressure air by nanosecond repetitively pulsed discharges", *Journal of Physics D: Applied Physics* **46**, 464010 (2013).

[106] W. Hua and K. Fukagata, "Near-surface electron transport and its influence on the discharge structure of nanosecond-pulsed dielectric-barrier-discharge under different electrode polarities", *Physics of Plasmas* **26**, 013514 (2019).